Investigations on Micro Loop Heat Pipe: Design, Fabrication and Mathematical Modeling using Thin-film Evaporation Theory

A THESIS

SUBMITTED IN PARTIAL FULFILLMENT OF THE REQUIREMENTS FOR THE DEGREE OF

DOCTOR OF PHILOSOPHY

BY

Shahnawaz Ahmed

Roll no. 136103007

Department of Mechanical Engineering

Indian Institute of Technology Guwahati

2020

Dedicated to my Parents and my mentor

DECLARATION

I declare the following:

- The work reported in the present thesis is an original research work, carried out by me, under the supervision of Prof. Manmohan Pandey.
- This thesis represents mine and my mentor's ideas in my own words and wherever I have used other's ideas, I have adequately cited their source.
- I have followed all the tenets of 'Scientific method' during my research and have reported the results without any bias and have not fabricated/misrepresented/falsified any facts/idea/source.

I verify that the above information is correct to the best of my knowledge.

Shahnawaz Ahmed
(136103007)

Date: December 22, 2020

Certificate

Department of Mechanical Engineering
Indian Institute of Technology Guwahati

The thesis titled "Investigations on Micro Loop Heat Pipe: Design, Fabrication and Mathematical Modeling using Thin-film Evaporation Theory" submitted by Shahnawaz Ahmed (Roll no. 136103007), for the award of the degree of Doctor of Philosophy is an original work. Its results have not been submitted in part, or in full, in any other Institute or University for the award of any degree or diploma.

Date: December 22, 2020

Prof. Manmohan Pandey

Department of Mechanical Engineering
Indian Institute of Technology Guwahati
781039 (Assam, INDIA)

ACKNOWLEDGEMENTS

I have a lot of people to thank for and even if I remember every one, writing all of their names here would create another thesis. Hence, I am keeping this section short and please forgive me if you don't find your names in it.

First and foremost, I would like to thank my mentor Prof. Manmohan Pandey, who has moulded me in his image and during the last seven years, has instilled in me a strong work ethic. I am who I am today because of him and I am proud of myself. My doctoral committee members: Prof. Ujjwal K. Saha, Prof. Amaresh Dalal and Prof. Dipankar Bandyopadhyay, who have always been very cooperative and took time out from their schedules to review my work. Prof. Amit Agrawal from IIT Bombay and Prof. Sameer Khandekar from IIT Kanpur who allowed me to work in their respective labs. The experience that I gained in there helped me complete my research work.

I would also like to thank Dr K Nageswari and her colleagues from INUP, IIT Bombay who are always working hard every day, so that students like me could finish their respective projects on time, Ashwini Gajarushi-Pandit madam, who helped me with fabrication of my test samples, Dr Vijay Duryodhan who was like a junior mentor and last, I am grateful for the help of Mr C S Goswami, Mr Sanjeev Chauhan and Mr Ravindra Kainthura from Phase Change Thermal Systems Laboratory, IIT Kanpur, in developing the experimental setup for the micro loop heat pipe device.

Finally, I would like to end this section with the mention of my friends and family who have always been with me since day one, and the latest addition to my life, my wife, Begum Emte Ajom. You all will always be in my heart.

Shahnawaz Ahmed
IIT Guwahati
December 22, 2020

ABSTRACT

Since its inception, micro loop heat pipe has played a significant role in maintaining a constant thermal environment, in applications where space is the primary constraint. Hence, it is a promising solution for passive thermal management in small wearable electronic devices like smartphones, smartwatches, ultra-thin laptop. Its most notable characteristics are gravity-independent operation and low maintenance cost due to the absence of any moving parts.

In this study, a new design of micro loop heat pipe is presented. Its dimensions are optimized to maximize the heat transport capacity. It is fabricated on a silicon wafer using a relatively simple microfabrication technique. It is then filled with methanol and performance tested. Next, a new mathematical model is developed to investigate the performance of its evaporator. This model is based on evaporating thin film in an extended meniscus inside a microchannel. Its novelty is that it combines two ideas: the use of the velocity slip boundary condition at the wall and modelling of both retarded and non-retarded components of disjoining pressure. This leads to better simulation of heat transfer phenomenon in the evaporator.

The work presented in this study is divided into two parts. In the first part, development of the micro loop heat pipe is described and in the second part, the new thin film evaporation model is explained. The results are summarized as follows:

Development of micro loop heat pipe:

- Design and optimization: The micro loop heat pipe is designed in such a way that it eliminates the need of a charge port (for filling the device with working fluid) and thermal barrier (for preventing the heat leak between vapour and liquid channels) without compromising its performance. Thus, the design is simple compared to that available in the literature. For optimization, its heat transport capacity is maximized for the width of evaporator channels and transport channels, its depth and overall length. It was found that the heat-carrying capacity is highly sensitive to the width of the evaporator channels and attains maxima for a specific value.
- Fabrication and charging: The device is fabricated on a 2-inch silicon wafer using MEMS-based techniques. Compared to other fabrication procedures used for MEMS based two-phase capillary devices, the present methodology is incomplex as it involves simple techniques and a lesser number of steps.

  For example, for better performance, the transport channels of micro loop heat pipe device should be rectangular with a high aspect ratio. Now, most of the fabrication technique in literature involves the use of Deep Reactive Ion Etching (DRIE) to form such channels. Since this technique is highly directional (anisotropic) and controllable,

perfect rectangular channels can be generated. However, since the process involves the use of plasma, it leads to complexity in the overall process flow and increases the cost. In the present study, this process is replaced with chemical etching. Etchant used is TMAH (tetramethylammonium hydroxide). TMAH is known to be highly anisotropic etchant. Also, the selection of wafer is made in such a manner that it has a high probability of etching rectangular microchannels (wafer with $\langle 1\,1\,0 \rangle$ orientation). In this way, the fabrication methodology is simplified.

After fabrication, the device is filled with working fluid. This involves purging of non-condensable gas from the device using a vacuum pump, then filling it from a fluid reservoir and then sealing. To seal the device, a micro metering valve is used.

- Performance tests: The device is connected with thermocouples, a strip heater and a heat sink. Methanol is used as the working fluid. The results of its performance testing are encouraging with a temperature reduction of 28.6°C at 3.78 W heat load.

Thin-film evaporation model:

- Mathematical model: In literature, there are many models based on thin-film evaporation, available to simulate the heat transfer in the evaporator. In the present work, these models are analyzed for their capability to model the physics of the problem. Both their strengths and shortcomings are highlighted. Hence, a novel method for estimation of the film thickness at the onset of evaporation is presented. It is tested for a wide range of superheats and is found to give physically realistic results. A new thin-film evaporation model is also presented, consisting of the velocity slip boundary condition at the wall and a disjoining pressure consisting of both retarded and non-retarded terms.
- Parametric study: The new model is validated with experimental data from literature and is found to give a good match. Next, parametric study is carried out. Effect of superheat on film thickness, heat flux, disjoining pressure, capillary pressure and mean liquid velocity is studied. It is found that the heat flux decreases monotonically throughout the thin-film region.
- A new figure of merit: During numerical simulation using the new model, a new parameter was discovered which can be used to calculate the maximum possible heat transfer coefficient of a cooling device undergoing thin-film evaporation. This parameter is independent of superheat and depends only on the properties of the working fluid. Its expression is simple (consists of three terms only: liquid thermal conductivity, saturated vapour pressure and dispersion constant). Hence, it requires minimal computational resource. This parameter is calculated for different working fluids, and it is plotted against a wide range of saturation temperature. Its trend is then compared with that of different figures of merit available in the literature and is found that it matches with them.

  Hence, this parameter is proposed as a new figure of merit for devices utilizing thin-film evaporation.

NOMENCLATURE

$\bar{A}$	Hamaker constant (J)
$\bar{u}$	Average velocity (m/s)
$\dot{m}$	Mass flow rate per unit depth(kg/ms)
$\dot{m}''$	Evaporation mass flux (kg/m^{2}s)
$\mathbb{R}$	Curvature (m^{-1})
$\overline{M}$	Molecular mass
$\overline{R}$	Universal Gas Constant (J/mol-K)
K_∞	Hagenbach's factor
m'	Mass flow rate (kg/s)
A	Dispersion constant (J)
b	Empirical factor (=5.32)
C_P	Heat capacity at constant Pressure (J/kg)
D	Diameter (m)
d	Depth (m)
e	characteristic wavelength (=100 nm)
f	Friction factor
fug	Fugacity
G	Gibb's free energy
h	Heat transfer coefficient, (W/m^{2}K)
I	Current (A)
J	Flux of molecules in one direction
k	Thermal conductivity(W/mK)

L	Length (m)
m	Ratio of particle diameter with effective pore radius
N	number of particle diameters along the wick thickness
n	Number of channels
P	Pressure (Pa)
Perm	Permeability (m^2)
Q	Power (W)
r	Radius (m)
R	Specific Gas Constant (J/kg-K)
Re	Reynolds Number
Res	Thermal resistance (°C/W)
s	Number density of vapour molecules
T	Temperature (°C)
t	Thickness (m)
V	Voltage (V)
w	Width (m)

Greek Symbols

α	Aspect ratio
γ	Area contraction ratio
ι	Carmen-Kozeny factor
λ	Latent heat of vaporisation (J/kg)
μ	Coefficient of viscosity (Pa s)
ϕ	Porosity
ρ	Density (kg/m^3)
σ	Surface Tension (N/m)
τ	Shear stress (N/m^2)
θ	Contact angle

Subscripts

a	ambient
c	Capillary
cond	Condenser
cont	Contraction
d	Disjoining
diff	Difference
eff	Effective
evap	evaoprator
exp	Experiment
h	Hydraulic
hl	Heat leak
in	Inlet
l	Liquid
lam	Laminar
lat	Latent
ll	Liquid line
m	Mole
out	Outlet
sa	source–ambient
sp	Single-phase
sub	Sub–cooling
tot	Total
tp	Two-phase
tur	Turbulent
v	Vapour
vc	Vapour chamber

Abbreviations

μlhp	Micro loop heat pipe

BOE	Buffered oxide etch
CC	Compensation chamber
CPS	Coherent Porous Silicon
DRIE	Deep reactive ion etching
DSA	Double sided aligner
ELR	Evaporator with lateral replenishment
EOR	Evaporator with opposite replenishment
FoM	Figure of merit
FoS	Factor of safety
g-field	Gravity field
IL	Interline
LBM	Lattice-Boltzmann method
lhp	Loop heat pipe
LTF	Liquid Transport Factor
MEMS	Microelectromechanical System
mlhp	Miniature loop heat pipe
NCG	Non-condensable gas
NTF	Nucleation Tolerance Factor
PDMS	Polydimethylsiloxane
PPR	Positive photoresist
PTFE	Polytetrafluoroethylene
SEM	Scanning electron microscope
TMAH	Tetramethylammonium hydroxide

TABLE OF CONTENTS

LIST OF FIGURES

LIST OF TABLES

Part I

Background

CHAPTER 1

INTRODUCTION

1.1 Motivation

With the advancement of technology, there has been a surge in the demand of small wearable day to day electronic equipment like smartphones, smartwatches and thin ultrabooks. One of the challenges faced in designing these compact, high computing processor and GPU laden devices are fabrication and thermal management. Thermal management is especially important as it limits the computing power and if not appropriately addressed, renders the strenuous fabrication methodologies meaningless.

Some of the conventional technologies available to combat these challenges are microchannel heat sinks, spray cooling, jet impingement, heat pipes, phase change cooling and thermo-electric cooling. Their characteristics and special features are summarised below:

1. Thermo-electric cooling: It generally applies the Peltier effect to achieve cooling. Its module consists of an alternating junction of p-type and n-type semiconductor materials, connected in such a way that they are thermally parallel and electrically in series. When current flows in one side, it leads to movement of electrons and holes from one side to other. This, in turn, brings about heat absorption from one side (source) and heat rejection to the other (sink). They have numerous advantages which include: no vibration or moving parts and hence minimal maintenance cost, no chemical reaction and long operating life[1]–[3]. Hence, this technology also finds use in battery, laser diode, medical devices and refrigeration. However, it suffers from disadvantages like low efficiency, high power requirement and suitable materials which limit its use.

2. Jet impingement: This involves the discharge of fluid with high velocity on the target surface to remove heat. Aside from electronic cooling, it is also applied in fabric drying, furnace heating, turbine blade cooling[4]. It has a high heat flux removal rate of the order of 2000 W/cm^2. Its main drawbacks are: requirement of high powered pump which also adds to the weight and volume footprint and shielding the electronic circuit from the working fluid.

3. Spray cooling: It is similar to jet impingement technique. Here the liquid is sprayed over the target surface. Heat is removed by single-phase or thin-film evaporation. Smakulski and Pietrowicz[5] listed some of its advantages, mainly: fast cooling rate, temperature uniformity, simple technique. However, a protective coating is required for the circuit board to prevent short-circuiting.

4. Phase change cooling: Here, the cooling is achieved by virtue of high latent heat. Hence, it is usually used in high heat flux applications like food industry[6], solar[7] and building cooling system[8]. Its advantages are economical, reusable and most importantly no requirement of additional equipment. However, it also has several problems, mainly: corrosiveness, supercooling, flammability disposal, and low thermal conductivity.

5. Microchannel heat sink: It is one of the most popular methods to remove high heat flux of the order of 1000 W/cm^2[9]. Here, the heat is removed by the flow of liquid through the microchannels. A pump is required for the flow. Single-phase convection or two-phase boiling is the primary source of heat transfer. It has also found widespread use in other areas like micro-turbine, micro-pump and similar MEMS-based application.

Their comparison have shown that technologies based on latent heat exchange (two-phase systems) hold a distinct advantage over the others[10]. Hence, in this study, the complete development of a micro loop heat pipe is shown.

1.2 Operating principle

The loop heat pipe (figure 1.1) consists of the evaporator, separate transport channel for liquid and vapour, condenser and a compensation chamber. Its operating principle is simple. Heat is applied in the evaporator where the liquid turns into vapour and through the vapour channel reaches condenser. In the condenser, the vapour condenses releasing the heat. The resultant liquid then travels to the evaporator through the liquid channel and compensation chamber where the cycle is again repeated. In the evaporator, there is sintered metallic or non-metallic powder called wick which provides

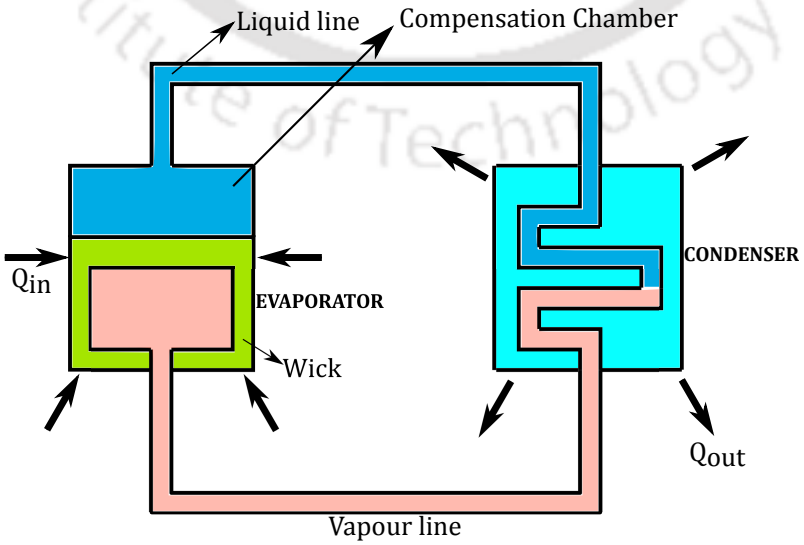

Figure 1.1: Generalised schematic of a loop heat pipe

capillary support to the liquid as well as aid in the removal of vapour (in MEMS-based micro loop heat pipes, capillary support is provided by numerous microchannels). It has the following advantages:

- No moving parts inside. Hence, no need for any active power source.
- Separate transport lines for vapour and liquid phase. As a result, there is no counterflow frictional loss which enhances the device performance.
- Presence of capillary structures structure in the evaporator only. This makes the device capable of working in any orientation in the gravitation field.
- A compensation chamber attached to the evaporator to regulate the liquid distribution in the device.

Thus, the micro loop heat pipe is a passive device suitable for both space as well as terrestrial applications. Hence, it is essential to study its design optimization, fabrication techniques, characterization and mathematical model, so, that it reaches its full potential.

To simulate heat transfer in the evaporator, thin-film evaporation model is used. In the microchannels of the evaporator, the liquid and vapour are in equilibrium as shown in figure 1.2(b). As can be seen from figure 1.2, the thin-film evaporation is encountered in various phenomena involving two-phase heat transfer, examples being nucleation, slug-plug flow, heated microchannels, and droplet evaporation. Based on the force acting on it, the extended meniscus can be divided into three regions:

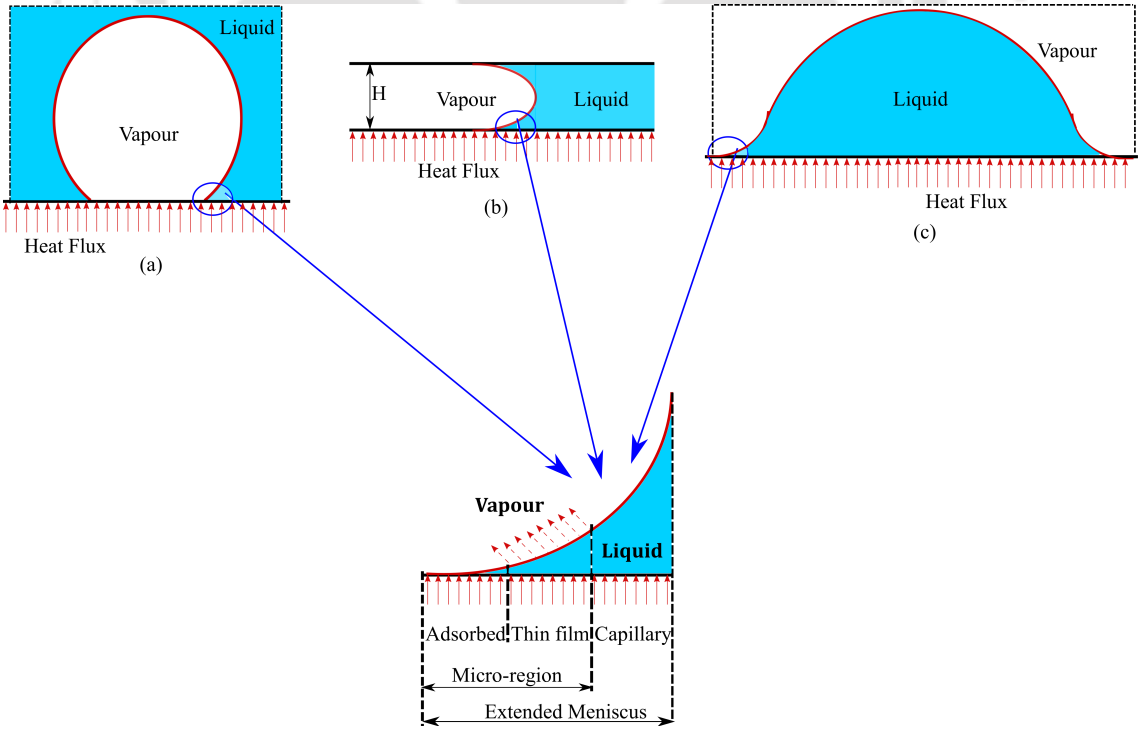

Figure 1.2: Extended Meniscus in (a) nucleation, (b) heated microchannels and (c) evaporation

- **The adsorbed region:** Here, the thickness of the film is minimal, due to which, the disjoining force (force arising due to interaction between the molecules of the working fluid and the substrate) dominates. The pressure balance for this region is the following:

$$P_v = P_l + P_d \tag{1.1}$$

- **The thin-film region:** In this region, both disjoining and capillary force is significant. Most of the heat transfer takes place in this region because of the low thermal resistance of the liquid film. The balance of pressures for this region is given by:

$$P_v = P_l + P_d + P_c \tag{1.2}$$

- **The intrinsic meniscus region:** This region is characterized by high capillary pressure due to the dominant surface force. Its pressure balance equation is:

$$P_v = P_l + P_c \tag{1.3}$$

Here, P_v, P_l, P_c and P_d are vapour, liquid, capillary and disjoining pressure respectively.

Recent molecular simulation has shown that the adsorbed layer plays a vital role in the evaporation[11], [12]. Existence of extremely high disjoining pressure (due to low film thickness) in this region leads to 'reduced/negative' liquid pressure, which in turn, makes the liquid flow from the meniscus to the thin-film region, thus aiding the evaporation process.

1.3 Brief history

This section is dedicated to the important landmarks in the development of the micro loop heat pipe technology and thin-film evaporation model, as shown in figures 1.3 and 1.4, respectively.

1.3.1 Micro loop heat pipe

The history of heat pipe dates back some two centuries ago, with the groundbreaking work on thermosyphons (known as 'Perkins Tube') by four generations of ingenious engineers with the family name Perkins[13]. It was patented in 1830 by Jakob Perkins. Because of its high operating temperature and fuel economy, it was widely used as a baking oven[14].

The concept of heat pipe was first put forward by Gaugler[15]. His design was mainly applied in refrigeration units. Nevertheless, the term 'HEAT PIPE' would not be used until 1963 by Grover in his patent[16]. Next important milestone is the development of loop heat pipe in 1972 with the aim of regulating the thermal needs of various systems of a spacecraft[17]. It had a length of 1.2m and capacity 1kW with water as working fluid. A decade later, in 1999, a miniature loop heat pipe was demonstrated[18].

In 1984, Cotter fabricated the first micro heat pipe[19] as a possible solution to the electronics overheating problem. It was of triangular cross-section having equal dimensions of 0.2 mm. Since then, with the advancement in technology, many researchers have produced and characterized micro versions of different types of heat pipes for electronic cooling purpose[20], [21].

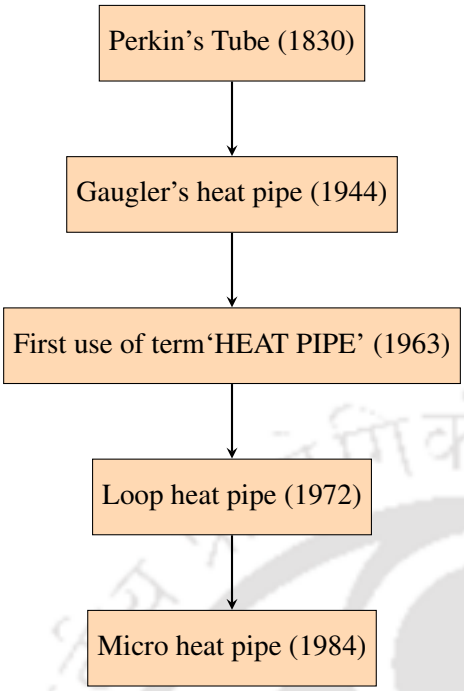

Figure 1.3: History of development of micro loop heat pipe

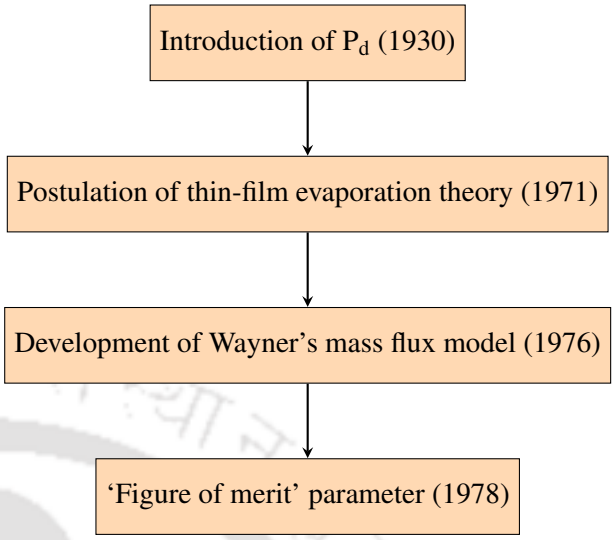

Figure 1.4: History of development of thin-film evaporation model

1.3.2 Thin-film evaporation

Dergajuin and coworkers pioneered the study of ultra thin-films. They defined a new force parameter to account for the force arising due to the interaction between the molecules of the working fluid and the substrate. Commonly known as the *disjoining pressure* and defined as "The difference between the pressure in a region of a phase adjacent to a surface confining it, and the pressure in the bulk of this phase". Wayner and Coccio[22] were one of the first to study the heat transfer phenomenon in a heated meniscus. They studied the heat transfer characteristics of an evaporating meniscus on a flat plate (stainless steel/aluminium) immersed in a pool of liquid (water/methanol). Their results showed that high heat flux occurs in the interline region of the meniscus, having value much higher than a simple conduction model. They came out with three different theories to explain this anomaly, first was the existence of turbulent interface, second was high convection due to surface tension gradients and third (most accepted) was the existence of a thin-film region adjacent to the intrinsic meniscus. Their work opened the door for more studies in this field. The following summarizes some of the earliest work.

Potash Jr. and Wayner Jr.[23] investigated the thin-film formed on a superheated glass using carbon tetrachloride as the working fluid. Using their mathematical model, they studied the extended meniscus profile. They discovered that the evaporating thin-film region is governed by both capillary and disjoining force. Wayner et al.[24] modified the Schrage Model[25] for evaporation mass flux into a simpler model which became commonly known as the Wayner's Model. Holm and Goplen[26] concluded that 80 percent of the heat transfer takes place in the region between the thin-film and capillary region (known as thin-film transition region).

Attempts were also made to theoretically compare the heat transfer capability in these regions using a dimensionless number[27], [28]. This lead to the development of a figure of merit parameter (equation (8.1)–derivation given in the appendix).

1.4 Overview of the dissertation

Figure 1.5 shows the break-up of research carried out in this study. As can be seen from this figure, it is divided into two parts. The 'device' part describes the overall development of micro loop heat pipe. It consists of a detailed description of how the present design was finalized and optimized, how a simple fabrication methodology was developed and how the device was filled with working fluid. Finally, the device performance was investigated using experimental results.

The second part deals with the numerical modelling of the evaporator. A new thin-film evaporation model was developed for this purpose. Its governing equations, boundary conditions and solution methodology are described in details, and parametric simulation is done to better understand the physics of heat transfer in the evaporator of μlhp devices.

The present dissertation has been divided into four parts:

- **Part I:** This section provides an overview of the work done. It describes the motivation behind this work, a brief history of its development along with a detailed literature review.
- **Part II:** In this section, experimental study of the μlhp is presented as well as its detailed fabrication procedure and charging methodology (filling of μlhp device with working fluid).
- **Part III:** This section deals with the detailed formulation of thin-film evaporation model.
- **Part IV:** This section summarizes all the results of the present study.

An appendix is provided at the end of the thesis where the derivation of important parameters is shown and some early results, during this research.

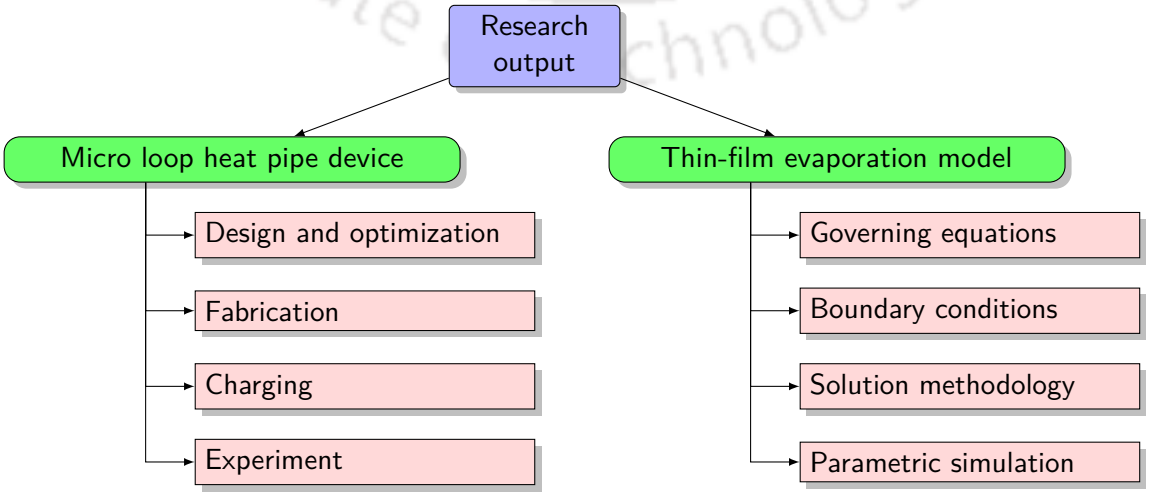

Figure 1.5: Overview of the research work

CHAPTER 2

LITERATURE SURVEY

In this chapter, a detailed literature survey of the present study is discussed. It is divided into two separate sections– loop heat pipe family and thin-film evaporation. Lastly, the gaps in the literature and objectives are presented.

2.1 Loop heat pipe

Based on their sizes, the loop heat pipe can be grouped into three distinct categories: conventional, miniature and micro loop heat pipes. Over the course of years, researchers have tried to give a clear definition of the terms 'miniature' and 'micro'. Ramaswamy et al.[29] presented a brief review on this for miniature loop heat pipes. They found that researchers have designated an lhp as 'miniature' for evaporator diameter up to 12 mm and diameter of transport channels not greater than 3.5 mm.

For micro heat pipes, Cotter[19] defined them as heat pipes so small that the curvature of its liquid-vapour interface is comparable to the reciprocal of hydraulic channel of its channels. Generally, micro heat pipes should satisfy the following criteria:

$$\frac{r_c}{r_h} \geq 1$$

$$\frac{(\rho_l - \rho_g)\, g\, {r_h}^2}{\sigma} \leq 1$$

The second equation represents the Bond/Eötvös number criterion.

In this section, a detailed review of these three types of lhp is given, along with a short description of the emerging practices followed while designing the evaporator and on working fluid selection.

2.1.1 Evaporator design

As shown in figure 1.1, the loop heat pipe system consists of an evaporator, condenser, compensation chamber and transport channels. Hence, its efficiency directly depends on the individual efficiency of these components. Based on the results obtained during optimization study (chapter 3), it is clear that the heat transport capacity parameter of lhp is highly sensitive to the wick

pore diameter. Hence, for the loop heat pipe to work properly, it is imperative to design efficient evaporators which would be both hydraulically as well as thermally linked to the wick. In this section, different designs of lhp evaporators are discussed.

Based on the menisci shape, the evaporators are of two types (figure 2.1):

- Inverted meniscus evaporator: Developed in 1975 by E W Saaski[30], in this design, heat enters from the vapour side of the meniscus[31], as shown in figure 2.1(a). It was developed in answer to the need of wicking concepts having high heat transfer coefficient as well as providing adequate pumping capability at high heat load and adverse tilt. The 'evaporator with opposite replenishment (EOR)' is based on this design scheme (figure 2.2(a)).

- Non-inverted meniscus evaporator: One disadvantage of the inverted meniscus design is that it has high thermal resistance and requires high temperature difference between the liquid and vapour side of the wick to operate[31]. To overcome this problem, non-inverted meniscus design is used. Here, heat enters from the liquid side of the meniscus (figure 2.1(b)). Since, in this design wick with high thermal conductivity can be used, it allows for the removal of comparatively high heat flux. However, high thermal conductivity also leads to undesirable heat leak from the evaporator to the compensation chamber.
  Example of such an evaporator is the evaporator with lateral replenishment (ELR), shown in figure 2.2(a). Tian et al.[32] further modified this scheme for their mlhp system with the wick (biporous) eccentrically installed in the evaporator. Their system showed good response in low heat load.

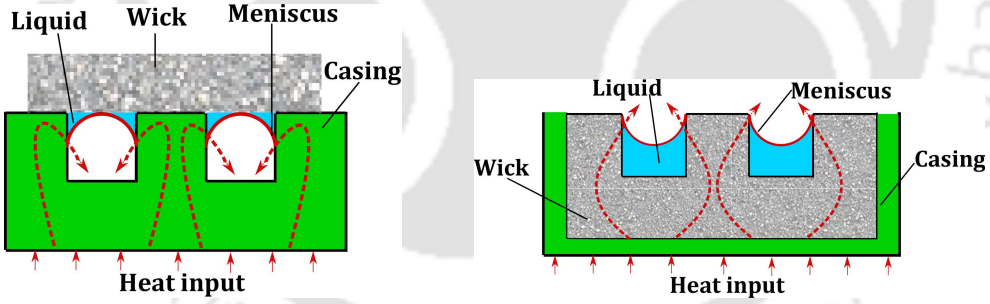

(a) Inverted meniscus (b) Non-inverted meniscus

Figure 2.1: Evaporator design used in LHP

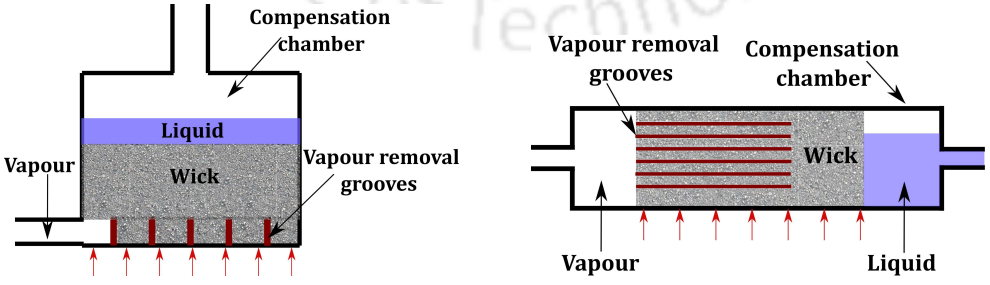

(a) Opposite replenishment scheme (EOR) (b) Lateral replenishment scheme (ELR)

Figure 2.2: Flat evaporator design scheme

Based on shape, lhp evaporators are either cylindrical[33], [34] or flat (rectangular and disc)[35], [36]. Flat evaporators are generally very easy to miniaturize and can easily maintain proper contact

with the heat source. Both EOR and ELR design schemes belong to it. However, they suffer from the following disadvantages[37]–[39]:

1. Increase in the internal pressure of the working fluid which results in a thicker wall (leading to an increase in weight) and limits the range of operating temperature.
2. Increase in compensation chamber temperature and start-up failure at low heat loads.
3. Increase in temperature instabilities due to higher heat leak to the compensation chamber.

The cylindrical evaporator does not suffer from such issues and its fabrication technique is comparatively simple and cheap. Its only disadvantage is the need of special thermal interface to maintain a proper contact with the heat source[40], which may increase its weight. Maydanik et al.[41] compared the performance of both cylindrical and flat evaporators in a loop heat pipe using ammonia as working fluid. Parameters compared were junction temperature, thermal resistance and start-up under different orientations. They observed that both the evaporators perform almost similarly under the same circumstances. However, it is the author's opinion that the thermal characteristics of their cylindrical evaporator was a bit better than their flat evaporator. As explained by Maydanik et al.[37], the thickness of EOR is limited by the dimensions of compensation chamber, which in turn depends on that of vapour line and condenser. Hence, its thickness cannot be reduced beyond 10 mm. ELR, on the other hand, does not suffer from such issues and hence, has thickness ranging from 3 to 8 mm. However, since its compensation chamber is located axially from the evaporator, it leads to an increase in the length of the evaporator.

In simple words, for those LHP-applications, where thickness is the limiting constraint, use of ELR evaporators is recommended, whereas for length constraints, use EOR. Generally, disc-shaped evaporators use EOR configuration and flat-oval shaped use ELR.

2.1.2 Working fluid selection

The working fluid should have the following desirable properties[42]:

- It should be compatible with the constituent material of the heat pipe, especially wick and evaporator wall.
- It should not break down at operating temperature range.
- Its vapour pressure should be at an optimum range.
- It should have high latent heat of vapourisation.
- It should have high thermal conductivity.
- It should have low viscosity in both liquid and vapour state.
- It should have high surface tension.

Using these criteria, a set of working fluids is selected. Once that is done, a correlation compromising of properties of working fluids only, is used to select the most suitable among the working fluids being considered.

The following three parameters are used to screen the working fluids for potential application in heat pipes[43]:

$$\mathrm{FoM_{LTF}} = \frac{\sigma \rho_l \lambda}{\mu_l} \tag{2.1a}$$

$$\mathrm{FoM_{g\text{-}field}} = \frac{\sigma}{\rho_l} \tag{2.1b}$$

$$\mathrm{FoM_{NTF}} = \frac{k_l \sigma}{\lambda \rho_v} \tag{2.1c}$$

Among them, $\mathrm{FoM_{LTF}}$ is the most popular figure of merit or merit number. It qualitatively represents the capillary limit of a heat pipe working in the absence of any body force, and having negligible vapour pressure drop. Hence, it is also known as '0-g figure of merit' or the 'liquid transport factor'. Poplaski et al.[44] modified it to estimate the performance of nanofluid charged heat pipes.

However, body force can affect the relative performance of the working fluid, as it works against the surface tension force[45]. Hence, the parameter $\mathrm{FoM_{g\text{-}field}}$ (equation (2.1b)) is proposed. It is also called capillary pump parameter. It is specially useful in evaluating the LHP performance working in 'anti-gravitational regime' (evaporator above condenser configuration)[46]. To minimize the unfavourable effect of the body-force, working fluid with higher value of this parameter is recommended.

Equation (2.1c) represents the measure of radial heat transfer tolerance. Higher the value of $\mathrm{FoM_{NTF}}$, greater the value of heat flux that the working fluid can withstand without undergoing nucleate boiling. Since, nucleate boiling is a precursor to dry-out, hence, this parameter can also be used to investigate dry-out limit of the device.

Figure 2.3 shows the variation of these parameters under different saturation/vapour temperatures, ranging from 0 to 100°C. The working fluids selected are ammonia, acetone, methanol, octane, pentane and water, which is the most common fluids used in heat pipes.
It can be observed from the figure that water is the most suitable working fluid owing to its highest value for all $\mathrm{FoM_{LTF}}$, $\mathrm{FoM_{g\text{-}field}}$, and $\mathrm{FoM_{NTF}}$ parameters. This can also be verified from the experimental results of Veeramachaneni et al.[47] and Hsu et al.[48]. They compared the performance of water and methanol using their respective heat pipe device and got better performance using water.

Over the years, several figures of merit/criteria were proposed. These parameters can be grouped, based on the different phenomena they represent in a heat pipe, as described in chapter 8.

2.1.3 Conventional loop heat pipe (lhp)

Here most of the researches are focused on two aspects: Performance studies and innovative design aimed at increasing the performance of the device.

1. Performance studies: For performance tests, parameters studied are maximum heat transfer capacity, heat transport distance, maximum evaporator temperature, thermal resistance and minimum heat load required for a successful start-up. Maydanik et al.[49] designed and fabricated a high capacity loop heat pipe able to transport 1700 W (12 W/cm^2) over a distance of 12 m while maintaining a source temperature of 89°C. Working fluid used was ammonia. Table 2.1 shows some of the recent performance studies on loop heat pipe. Other parameters

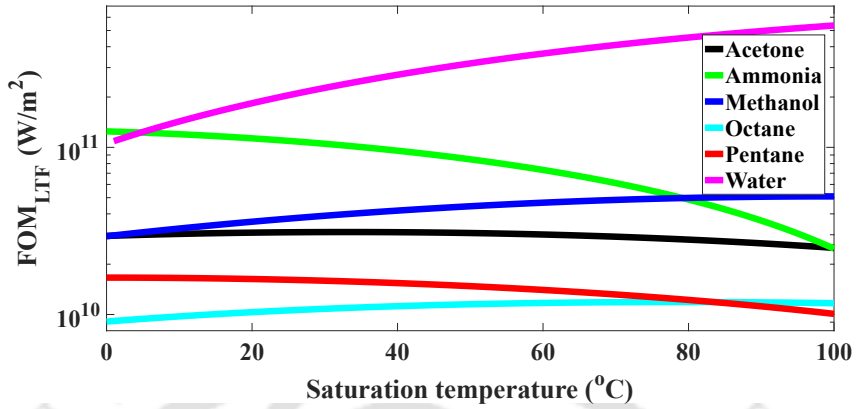

(a)

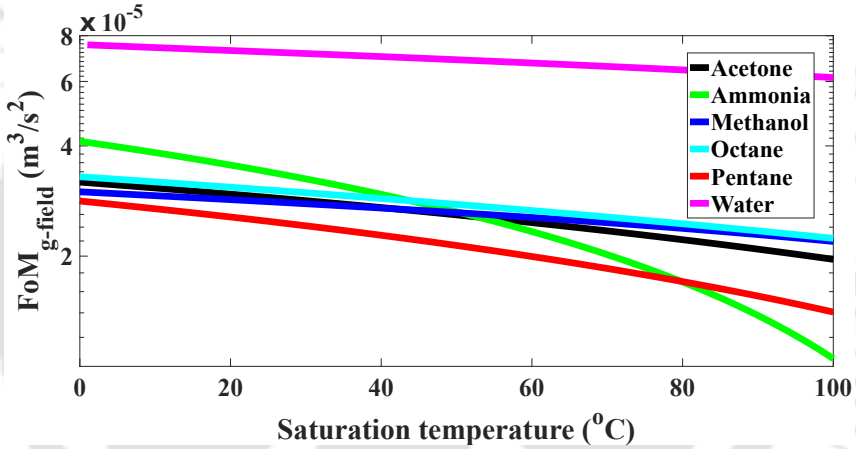

(b)

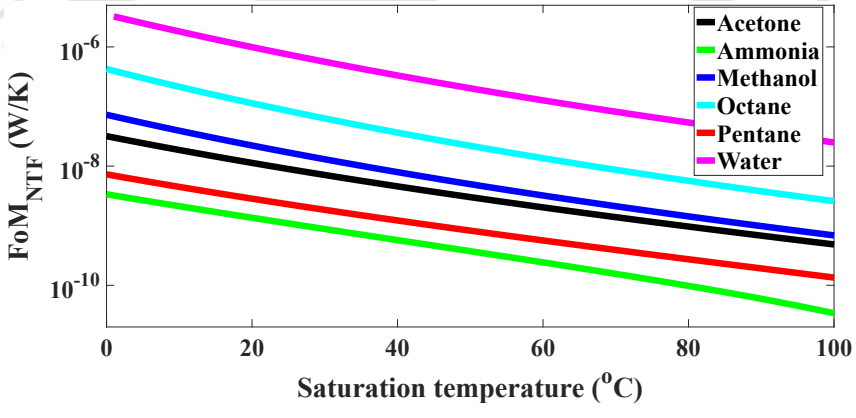

(c)

Figure 2.3: Variation of (a) Liquid transport factor, (b) g-field factor and (c) Nucleation tolerance factor for heat pipes

Table 2.1: Summary of recent performance studies on loop heat pipe

Research	Specifications	Performance test/results
[46]	Working fluid: Ammonia Wick: Nickel and stainless steel (biporous) Evaporator: 91.5 mm (flat) Liquid line: ID = $\phi 2/1.5 \times 485$ mm Vapour line: ID = $\phi 3/2.5 \times 330$ mm	Heat transport capacity = 500 W Maximum temperature = 70°C Thermal resistance = 0.147°C/W
[55]	Working fluid: Water Wick: PTFE Evaporator: $240 \times 260 \times 33$ mm (flat) Liquid line: ID = $\phi 6.35/4.35 \times 1060$ mm Vapour line: ID = $\phi 6.35/4.35 \times 4.35$ mm	Heat transport capacity = 650 W Maximum temperature = 180°C Thermal resistance = 0.071K/W
[56]	Working fluid: Acetone Wick: Nickel Evaporator: $\phi 11 \times 85$ mm (semi-cylindrical) Liquid line: $\phi 3/2 \times 1090$ mm Vapour line: $\phi 3/2 \times 1150$ mm	Heat transport capacity = 60 W
[57]	Working fluid: R134a Wick: Stainless steel Evaporator: $\phi 13/11 \times 90$ mm (cylindrical) Liquid line: $\phi 6/5 \times 720$ mm Vapour line: $\phi 6/5 \times 520$ mm	Heat transport capacity = >100 W Maximum temperature = 70°C Thermal resistance = 0.78°C/W Start-up load = 2W
[58]	Working fluid: n-pentane Wick: Copper Liquid line: $\phi 49.7 \times 250$ mm Vapour line: $\phi 66.7 \times 500$ mm	Heat transport capacity = 200 W Maximum temperature = 50.7°C
[59]	Working fluid: Water Wick: Charcoal Evaporator: $36 \times 26 \times 16$ mm (flat) Vapour line: $\phi 6$ mm	Heat transport capacity = 250 W Maximum temperature = 95°C Thermal resistance = 0.17°C/W
[60]	Working fluid: Nitrogen Wick: Nickel Evaporator: $16.57 \times 75 \times 1.015$ mm (cylindrical) Transport lines: $1.755 \times 680 \times 0.71$ mm	Heat transport capacity = 12.17 W Maximum temperature = -170.38°C Thermal resistance = 0.25K/W

studied are effect of inclination, temperature oscillation and effect of varying heat load[50]–[54]. Comparison tests of different wicks and working fluids in the loop heat pipes are also studied.

The most critical among the performance test is the start-up test. Nishikawara et al.[50] studied the effect of phase distribution in the evaporator during start-up. They experimented with eight phase-patterns and compared their findings with those of Ku[61]. They noted some differences in their data which may be due to different wick materials. In their study, they also stressed the need for more detailed experiments with different wick and working fluid. Wang and Wei [51] described in details the start-up characteristic of their device which is subdivided into seven different processes: the initial liquid supply from the evaporator to boiling pool; the appearance of an increasingly intense boiling process in the compensation chamber; the dynamic equilibrium of evaporation and liquid supply inside the compensation chamber; the appearance of breathing phenomena; its termination; the periodic turn out of circulation start and circulation stop; the acquirement of steady-state operation. The second most important study is the temperature oscillation. Studies have shown that it arises due to rise/collapse of bubbles, orientation and low heat load [62]–[64].

2. Innovative design: Over the years, various researchers have used different methods to improve the performance of their heat pipe systems. Khalidi et al.[65] presented a review on it. Topics covered were heat transfer enhancement using nanofluids, fins, self-rewetting fluids and other miscellaneous techniques like use of magnetic field.

   In this section, design modification and other creative ideas, for performance augmentation of loop heat pipe systems are given.

   - Start-up improvement: Jung and Boo[66] installed a bypass line to purge excessive vapours from the evaporator. This resulted in prevention of temperature overshoot during start-up and as a result the start-up time was reduced.
   - Minimizing heat leak: In a bid to prevent heat leak from the evaporator to the compensation chamber, researchers have used many innovative ideas. Following are some examples:

     (a) Khalili et al.[67] placed a steel ball inside the evaporator (non-inverted meniscus design). Using magnets, the steel ball can be moved to different positions in the evaporator and temperature reading was taken against varying heat load. They observed that the operating temperature of the loop heat pipe device was different based on the position of the steel ball and attained minimum value when it was placed in contact with the wick separating the evaporator and the compensation chamber (called reservoir in this study). This enabled them to actively control the operating temperature of the loop heat pipe. They also observed that the heat leak is the lowest when the steel ball is in that position.

     (b) Yang et al.[68] and Zhu et al.[69] fabricated a loop heat pipe having wick completely separate from the evaporator shell. The liquid from the wick is transported to a heated chamber (called steam chamber) where the resultant vapour goes into

the transport channel. Performance test yielded a short start-up time for the device. However, the thermal resistance was relatively high. In another study[70], this configuration (called Config3) was compared with two other designs of evaporator: one design consists of vapour channels embedded on the heated surface and the other was having vapour channels on the wick. It was observed that Config3 had better thermal characteristics compared to the other designs.

(c) Lu and Wei[71] added a separate pool boiling heat transfer chamber along side the evaporator. The idea was to reduce the load on the evaporator under high heat flux which would minimize the heat leak. In later studies, separate fabricated separate micro and nano structures were added into the boiling pool container to increase the performance of the device[72]. Experimental studies confirmed the same and an overall enhancement of 110% in the heat transfer coefficient was observed.

- Use of external pump: Loop heat pipes are passive, self-regulatory devices, having a wide range of operating conditions. Sometimes, researchers modify its design and add an external mechanism to improve its performance. Examples are:

  (a) Kiseev and Sazhin[73] implemented a steam ejector in their loop heat pipe to increase the heat transport distance. They claimed that their design could work favourably under high acceleration but encountered start-up problems at high temperature (50°C).

  (b) Setyawan et al.[74] connected a diaphragm pump to the loop. The function of this pump was to pump working fluid into the evaporator under high heat flux, thereby reducing the chance of a dry-out under such conditions and also decreasing the evaporator temperature.

  (c) Zhang et al.[75] used a light-weight centrifugal micropump to reduce temperature oscillations and increase the heat transfer distance. Experimental investigation confirmed that their device reached steady-state within 5 minutes even at low heat load.

- A combined Loop-pulsating heat pipe system was designed by Pastukhov and Maydanik[76] to decrease the thermal resistance of the device and increase the heat removal area. Ammonia and R141b were used in the loop heat pipe and pulsating heat pipe system, respectively.

- Anti-freeze system: Since, water expands on cooling below 0°C, it will damage the capillary wick and also subject the LHP structures to high deformative force. That is why, water is not used for low temperature applications in loop heat pipe. However, Petit et al.[77] proposed a solution. They put forward three LHP designs where they integrated anti-freeze system using adsorption. The first configuration consists of thermally and hydraulically linking the evaporator with the adsorbent through a series of valves, which could be operated manually when the need arises. The second configuration consists of connecting the adsorbent tank with the LHP system, without the use of valves through the vapour line. This system can be used when space is the limiting constraint. The third configuration is directly integrating the evaporator with

the adsorbent tank. This enables the system to work autonomously, but requires more space for the evaporator. In all the configurations, silica gel is selected as the adsorbent.

- Dual compensation chamber: Loop heat pipes with dual compensation chambers are used under conditions subject to high acceleration force or adverse terrestrial attitude[78]–[82]. Recently, Du et al.[83] fabricated a loop heat pipe without any compensation chamber. This enabled them to use a smaller evaporator. They also fitted a portion of liquid line with copper wick. Experimental investigation showed that the their device had improved start-up characteristics and could start at very low heat load (10W). This was attributed to the presence of wick in the liquid line which ensured that the fluid entering the evaporator is always sub-cooled.

Thus, it is clear that loop heat pipes have achieved wide-spread application in various technologies. Some of the examples are: cryogenics[84]–[86], microgravity[87]–[89], solar applications[90], [91] and other miscellaneous applications (aircraft anti-icing system[63] and waste heat recovery[92]).

2.1.4 Miniature loop heat pipe (mlhp)

The mlhp was developed primarily to solve the 'electronic over-heating' problem[93]–[95]. Their main applications include mobile phones and slim laptops[96]. Researchers have also explored the feasibility of mlhp in other applications namely avionics cooling[97], LED cooling[98] and cryogenics[99]–[101]. The review in this section is categorized into the following fields based on the aim and focus of the research:

- **Parametric investigation:** In this section, studies on the effect of different parameters, and comparative analysis of different components, on the performance of the mlhp are summarized.
  Singh et al.[102] investigated the effect of wick properties. Parameters varied were wick material (nickel and copper), flow parameters and structures. They concluded that copper wick gives superior performance at low to moderate heat load. This is because of its high thermal conductivity compared to nickel. However, high thermal conductivity leads to higher heat leak at high thermal load. This was also confirmed in a separate study using a theoretical model[103]. They also concluded that high porosity and high permeability increases the performance of the wick by minimizing the heat leak and the pressure loss respectively. Maydanik and Vershinin[104] compared the performance of nickel and titanium wicks in their system by using different cooling methods in the condenser.
  Effect of different working fluids was also studied. Nishikawara and Nagano[105] compared the performance between ethanol, acetone, and R134a. They confirmed that the performance of working fluids is in accordance with their respective figure of merit (equation (2.1)). They also studied the effect of clearance between evaporator casing and wick, working fluid inventory and sink temperature. Anand et al.[106] used acetone, methanol, n-pentane and ethanol as working fluids for their mlhp system with special emphasis on spacecraft applications. They also observed that n-pentane gives the best performance owing to its highest figure of merit (equation (8.4)) of the four and the methanol has the highest capillary

limit.

Tharayil et al.[107] varied the working fluid filling ratio to study its effect on the performance of their mlhp having a copper-water configuration. They concluded that out of different values used, charging ratio of 30% gives the best performance.

- **Temperature transients:** Gai et al.[108] observed that temperature oscillation increases with increase in charging ratio and decrease in tilt angle. Vershinin and Maydanik [109] found out that temperature oscillation occurs due to shortage of working fluid and high intensity cooling in the condenser. They also observed that oscillation occur at 'Evaporator above condenser' and 'Compensation chamber above evaporator' configuration. Chen et al.[110] also did a detailed study of temperature oscillation and component layout. They observed high-temperature oscillation for horizontal orientation, 'evaporator above condenser' and 'Compensation chamber above evaporator' configuration and minimum temperature oscillation in the evaporator. Additionally, start-up difficulty was encountered in 'Condenser above evaporator' and 'Evaporator above condenser' configuration. Ramasamy et al.[29] carried out a complete characterization (start-up, orientation and temperature oscillations test) of their mlhp. They observed temperature oscillations in three configurations in their system: 'horizontal', 'compensation chamber above evaporator' and 'evaporator above compensation chamber' at moderate heat load and low sink temperature (5 and 20 °C). Singh et al.[111] explained that at moderate heat load, two conflicting processes leads to temperature oscillations. One process is that at moderate heat load, the condenser is no longer able to fully function (because of high mass flow rate). This results in vapour entering the liquid line and eventually reaching the compensation chamber/evaporator, thereby, increasing the evaporator temperature. This leads to the second conflicting process where high evaporator temperature leads to high heat leak from the evaporator to compensation chamber. This lowers the phase change phenomenon and in turn lowers the mass flow rate, and as a result leads to low evaporator temperature. Both these process give rise to temperature oscillations.

- **Effect of non-condensable gas (NCG):** Presence of NCG always has a deteriorating effect on the performance of heat pipes by increasing the operating temperature and loop pressure. Singh et al.[112] observed more performance degradation at lower heat load and an increase in start-up time in their mlhp system due to NCG. They also observed that their system could tolerate the NCG up to a limit without any performance detoriation because of the compensation chamber, where most of the NCG get stored.

  Anand[113] used an intentionally defective gasket to simulate a leaked mlhp system. This enabled him to study the effect of different mass of NCG at a wide range of heat loads. He used an absolute pressure transducer and a special capacitive gauge in the mlhp to determine the mass of NCG inside the system.

- **Effect of nanoparticle:** Many researchers have used nanofluids (nanoparticles suspended in working fluid) and metal coatings on the evaporator surface with the aim to increase the performance of their devices. It has been proved that presence of nanoparticles in minute concentration leds to a huge increase in the performance of the heat pipe system. Examples are:

1. Graphene-water[114], [115]: optimum volume concentration of 0.006% leads to 21.6% reduction in thermal resistance, 34.6% reduction in entropy generation, and 37.5% enhancement in the second law efficiency.
2. Copper nanoparticles coating: Krishnan et al. [116] deposited different coatings of 35, 70, and 130 nm diameter with 25 μm height using electrodeposition technique. They observed a 2.7 times increase in the heat transfer coefficient and 33% reduction in thermal resistance.
   Tharayil et al.[117] deposited coating of different thickness ranging from 100 to 500 nm using physical vapour deposition. They observed 86% increase in the heat transfer coefficient and 22.6% reduction in thermal resistance.

In another study, Tharayil et al.[118] used a combination of graphene-water nanofluid and copper coatings to get 45.2% reduction in thermal resistance, and 113.4% enhancement in the heat transfer coefficient.

2.1.5 Micro loop heat pipe (μlhp)

The most prominent characteristic that sets them apart from conventional and miniature loop heat pipes is the absence of wick. Here the function of wick (capillary support) is carried out by minute grooves which are machined into the device. Although invented way back in 1984 by Cotter [19], research is still lagging behind as compared to their counterparts mainly due to fabrication difficulties. Table 2.2 shows the summary of experimental studies carried out.

For improving the performance of μlhp, researchers have developed different methods to increase the efficiency of its different components. Examples are:

1. CPS wick[119]–[121]: It developed with the aim of providing flat planar evaporator for the μlhp, thereby providing better thermal contact and compact size.
2. Liquid grooves in the compensation chamber[122]: μLHP with flat evaporators have an inherent disadvantage of high pressure drop in the wick. Hence, Fukushima and Nagano[122] fabricated a μlhp with a unique evaporator-compensation chamber structure where grooves were provided in the compensation chamber to facilitate transportation of liquid into the evaporator. This reduces the pressure loss in the wick.
3. μlhp with no wick: Wang et al.[123] developed a new type of μlhp, having no wick in the evaporator. The capillary support was provided by the liquid channels. They also fabricated nanopillars into the condenser, which enhanced the condensation.
4. Charging technique: Dhillon and Pissano[124] demonstrated a unique method to charge their μlhp device, called dual port thermal flux method. It consists of two steps. In the first step, degassing is done by passing vapour through the device at high speed. Next, the device is allowed to cool, which in turn condenses the vapour into liquid. Finally, the device is permanently sealed.

Ghajar et al.[127] developed a mathematical model to predict its performance. Using the model, a parametric study of the geometry of μlhp was performed. A special 2D CFD model (given by

Table 2.2: Summary of performance studies on micro loop heat pipe

Research	Specifications	Performance test/results
[125]	Working fluid: Water Wick: Copper Evaporator: $20 \times 17 \times 0.6$ mm Liquid line: $120 \times 6 \times 0.6$ mm Vapour line: $75 \times 7.6 \times 1$ mm	Heat transport capacity = 20 W Maximum temperature = 110 °C Thermal resistance = 0.11 °C/W
[123]	Working fluid: Water Evaporator: 1 mm^2 Liquid line: $20 \times 0.5 \times 0.0003$ mm Vapour line: ID = $20 \times 1 \times 0.003$ mm	Heat transport capacity = 3.4×10^{-6} W Maximum temperature = 110 °C
[122]	Working fluid: Ethanol Wick: PTFE Evaporator: $20 \times 10 \times 3$ mm Transport line: $\phi 1.56 \times 200$ mm	Heat transport capacity = 11 W Maximum temperature = 80.5 °C Thermal resistance = 1.21 °C/W
[126]	Working fluid: Water Wick: Copper Evaporator: $20 \times 17 \times 0.6$ mm Liquid line: $120 \times 4 \times 0.4$ mm Vapour line: $75 \times 5.6 \times 1$ mm	Heat transport capacity = 15 W Maximum temperature = 50.5°C Thermal resistance = 0.32°C/W
[48]	Working fluid: Methanol and water Wick: Microchannels etched in silicon wafer Depth of the device: 263 µm Evaporator: 8.5×10 mm Liquid line: 35 mm Vapour line: 40 mm	Heat transport capacity = 12.92 W Thermal resistance = 0.106 °C/W

equation (2.2)) was incorporated into the code to simulate the heat leak from the evaporator to the compensation chamber. An insulated boundary condition for all the outside boundary was used.

$$\nabla \cdot (\mathrm{k}(y)\nabla \mathrm{T}) = 0 \tag{2.2}$$

Although this model could capture the trend of experimental data, there was still some inconsistency between them. As explained by the authors, this was because the ambient heat transfer was ignored. The model was later modified and an ADI (alternating direction implicit) scheme was used to solve equation (2.2). This new model was used to perform optimization study and predict the evaporator temperature as a function of heat input, ambient temperature and geometry[128]. In later studies, they incorporated thin-film evaporation model in their code[129]. This model could predict the heat transfer coefficient in the capillary grooves of the evaporator and calculate the dry-out distance.

2.2 Thin-film evaporation model

Figure 1.2 shows thin-film evaporation encountered in various real-life applications like nucleation, slug-plug flow, droplet evaporation and heated microchannels[130]. It is especially used to study the liquid-vapour interface in the evaporators of two-phase capillary devices like the wicked heat pipe, vapour chamber, capillary pumped loop and loop heat pipe[131]–[134]. As explained by Mandel et al.[135], when the conduction thermal resistance through the liquid film is less than nucleate boiling thermal resistance, direct evaporation from the liquid into vapour takes place. Recent studies[136]–[140] have shown that such direct evaporation has the capacity of removing very high heat flux (order of 100 W/m^2. Hence, the study of thin-film evaporation presents a very attractive solution for electronics heating problem and the need for a numerical model predicting important variables like the film thickness profile, temperature distribution and heat transfer coefficient.

Since the scale of an evaporating meniscus ranges from a few nanometers to millimetre, a natural question arises whether the Continuum theory holds in this case. Freund[141] compared the results obtained from atomistic simulation of a liquid drop on a cold spot surrounded by hot spots and the results from simulation using Continuum mechanics for the same drop. They found that the Continuum model is accurate in predicting the mass flux and interface shape of an evaporating meniscus. In general practice, atomistic simulation is used up to the adsorbed region and Continuum theory is used from thin-film onward.

In this study, the literature study is broadly divided into three groups: the first one presents the different ways by which researchers have increased the accuracy of their thin-film evaporation model, the second one explains the different solution methodologies and the third one explains the different experimental study.

2.2.1 Study of different parameters

The thin-film evaporation model is an amalgamation of different models. It consists of film thickness parameter, liquid pressure parameter, mass flow rate, interface temperature, capillary and disjoining pressure. Different researchers have tried to improve its modelling technique by focusing on one or more of those constituent models. They are summarized as follows:

1. **Vapour pressure gradient and slip boundary condition:** Most of the researchers assume uniform vapour pressure and hence neglect the vapour pressure gradient. To simplify the simulation, they also assume no-slip boundary condition at the wall. Park et al. [142] however, considered both vapour pressure gradient and slip boundary condition in their studies and came to the conclusion that vapour pressure gradient does have an effect on the shape and thickness of thin-film and hence, should not be neglected. Subsequently, more researchers have considered vapour pressure gradient [143] and slip boundary condition [144]–[148] in their thin-film evaporation studies.

2. **Mass flow rate:** It is calculated from different mass flux model. Some of the most popular models are Schrage model [25], Wayner model [24] and Linear model. Out of these three, the Linear Model is the simplest and easiest to implement. As stated in section 1.3, Wayner Model is the simplified form of Schrage model (derivation shown in the appendix). Wayner Model can be further modified to give the Moosman and Homsy Model [149]. Wang et al. [150] compared the thin-film profile generated from Schrage and Wayner Model and observed that the profile matches at low superheat and start diverging when the superheat becomes high. Thus, from their study, it can be concluded that Wayner Model can be used for low superheat (up to 5K) and beyond that Schrage Model should be used. Kou et al. [151] confirmed that the Linear Model overestimates the thin-film profile.

3. **Disjoining pressure:** Since thin-films are sensitive to disjoining pressure, some researchers have used different models on disjoining pressure to accurately simulate the heat transfer in thin-films. The most popular disjoining pressure model is given by:

$$P_d = \frac{A}{\delta^3}$$

This model takes into account the non-retarded dispersion component only.
Setchi et al.[152] considered two additional terms along with this component for their disjoining pressure model. They are structural force (arising from the interactions of liquid molecules between two approaching interfaces), short-range repulsion force. They concluded that the structural component is dominant when the film thickness is between two and twenty-five times the molecular diameter of the working fluid and the dispersion component is dominant when it is greater than twenty-five times the molecular diameter. Effect of structural force in the disjoining pressure model was also considered by Du and Zhao [153] and Azarkish et al. [154]. Hu et al.[136] used a modified disjoining pressure model to study the effect of nanoscale surface roughness on thin film evaporation. Using their model, they found that there exists an optimal range of pitch where the cumulative heat transfer range is maximum. Biswal et al. [155] considered slope and curvature dependence of the disjoining pressure and Hanchak et al. [156] considered both retarded and non-retarded terms.

4. **Momentum equation:** The lubrication approximation is widely used in the simulation of thin-films where one dimension is very small compared to the other. It is derived by expanding the Navier-Stokes equation taking $\alpha << 1$ and neglecting the fluid inertia. Morris et al.[157] analyzed the classical dam-break problem for thin-films by comparing the results

from lubrication approximation and 2-D Navier-Stokes equation. They concluded that the Lubrication approximation gives satisfactory results for low Reynolds and Froude number. For evaporation in thin-films case, velocity is zero at the absorbed region, then it increases and reaches its maximum value in thin-film region and then decreases again as capillary region approaches (figure 7.8), its average Reynolds number is low. Hence, the lubrication approximation holds in this case. Ma et al.[158] and Yan et al.[159] confirmed that the momentum conservation and energy conservation terms might affect the results, but they can be neglected near the adsorbed region. They only change the meniscus length at which the maximum value of heat flux and velocity occurs. Fu et al.[160] added the effects of bulk flow and interfacial thermal resistance in their model.

5. **Thermocapillary stress:** As explained by Wee et al.[148] surface tension gradient is generated due to the temperature gradient in the meniscus. This leads to thermocapillary stress which reduces the film length. Mirzamoghadam and Catton[161], Hallinan et al.[162] and Lim et al.[163] also considered the thermocapillary stress in their analysis. In another study, Lim et al.[164] investigated the heat transfer characteristics of self -rewettable fluids using this theory. They used dilute aqueous solution of heptanol as working fluid, having negative surface tension gradient.

2.2.2 Solution strategy

Next, different strategies to solve the governing equations are discussed. Du and Zhao[153] and Jasvanth et al.[165] listed the three different strategies available in the literature:

1. In this approach, the calculation is initiated in the capillary region where the disjoining pressure is negligible and capillary pressure dominates as was done by Akkus and Dursunkaya [166] and Bellur et al.[167] and then march towards the thin-film region. This method has two advantages. One is the elimination of the need to modify or tune the boundary conditions. The other is the elimination of calculation of non-evaporating film thickness at the contact line. However, as Du and Zhao [153] pointed out, the exact point where the calculation should be initiated is not clearly defined and curvature of the profile changes rapidly at this position.

2. Here, the intrinsic meniscus is treated an isothermal meniscus and appropriate boundary conditions are applied. However, the profile so generated doesn't touch the heater wall at high superheat[153].

3. In this approach, the calculation is initiated from that point where the film thickness is equal to that of its retarded region and then march towards the capillary region. Since this point is clearly defined both experimentally and numerically, this approach is widely used for thin-film evaporation analysis (it is also used in the present study). However, as will be discussed in section 6.2, this approach has its own set of drawbacks.

Some researchers have also used the Lattice-Boltzmann Method (LBM) to simulate this phenomenon. Zhang et al.[168] developed a 3-D LB model incorporating the equation of state of

a real gas. Using this model, they studied the heat transfer in a thin-film between two micropillars. Parameters varied were heat flux and contact angle and the interface was tracked. Other researchers[169], [170] have used LBM to study the hydrophobicity/hydrophilicity of the wall and to increase the efficiency of the heat transfer in thin-films.

2.2.3 Experimental study

As discussed in section 1.3, Wayner and Coccio[22] had postulated the existence of an evaporating liquid meniscus in their experimental study. Since then, there has been significant progress in the experimental investigation of this phenomenon. Generally, the following parameters are measured:

1. Film thickness: Researchers have used different methods to measure the film thickness of a heated meniscus. Some of the notable methods used are: ellipsometry[171], interferometry[156], [172]–[175], reflective-mode confocal microscopy [176], laser confocal displacement sensor [177], Shack–Hartmann wavefront sensor [175] and laser sheet sounding [178].

2. Interface temperature: Because of the high evaporation rate of this phenomenon, a local cooling spot exists where there is a clear dip in temperature. Hömann et al.[179] and Sodtke et al.[180] attempted to characterize this temperature drop. They used thermochromic liquid crystals to measure the temperature distribution underneath the evaporating meniscus. However, Hömann et al.[179] method had high uncertainty and hence recommended using Savitzky–Golay filters for higher accuracy.

3. Heat flux: Matin et al.[137] explained that the measured film thickness and temperature for a heated meniscus have a high degree of uncertainty and is limited to 1 to 10 µm thickness range. Hence, it is better to measure the wall heat flux (even though it comes with its own set of challenges).
   Xu and Carey[181] experimentally investigated the heat transfer characteristic of film evaporation on a 'V' shaped copper microgroove, having dimension 64×190 µm. They had mounted the test section in a cylindrical SS tank. Two electrical heaters were then clamped on either side of the test section and thermocouples were connected at different position underneath it. Working fluid used was acetone and methanol. A condenser was connected at the top of the tank to control the saturation condition. Heat flux and heat transfer coefficient were calculated from the temperature reading. However, the uncertainty in their calculated parameters was very high and did not validate their model. Jasvanth et al.[182] experimental setup consists of a capillary slot using two glass plates ($100 \times 100 \times 5$ mm) separated by 100 µm distance, constant temperature reservoir, weighing scale, cathetometer and pentane as working fluid. The unique aspect of their set up was it can be used to simultaneously measure wicking height and evaporation rate, which can be used to calculate apparent contact angle. However, their experimental data did not match with their numerical data (They matched in a later study[165]). Nazari et al.[138] achieved a heat flux of 11 ± 2 kW/cm^2 using thin-film evaporation in nanochannels (6×25 µm) with isopropyl alcohol (IPA). Such small geometry allowed them to use negative pressure to reach high heat flux. Matin et al.[137]

designed a sensor array to characterize heat flux and temperature for a heated meniscus in a microchannel (300 × 75 µm) using FC-72 as working fluid. The sensor array consists of 50 resistance temperature detectors (RTD) (50 nm titanium layer (adhesive) and 100 nm platinum layer).

2.3 Gaps in the literature

- **Micro loop heat pipe:** Figure 2.4 shows an estimate of the proportion of research work available for different types of loop heat pipe. As expected, more than 50 % share belongs to the conventional ones and less than 5 % to μlhp. This is because of the lack of proper fabrication techniques for μlhp. As pointed out by Phan and Nagano[183], the present fabrication procedures (both MEMS and mechanical manufacturing process) have drawbacks, *i.e.* process complexity, expensive equipments and difficulty in controlling. Another challenge is charging. Because of the extremely low amount of working fluid involved (10 to 100 µl) and small device size, it becomes very difficult to purge non-condensable gas and control the flow of working fluid during charging.
  Figure 2.5 shows the number of experimental investigation of different types of MEMS-based micro heat pipes available in the literature (data taken from Qu et al.[184]). As can be seen from the figure, here also, the μlhp share is lowest.

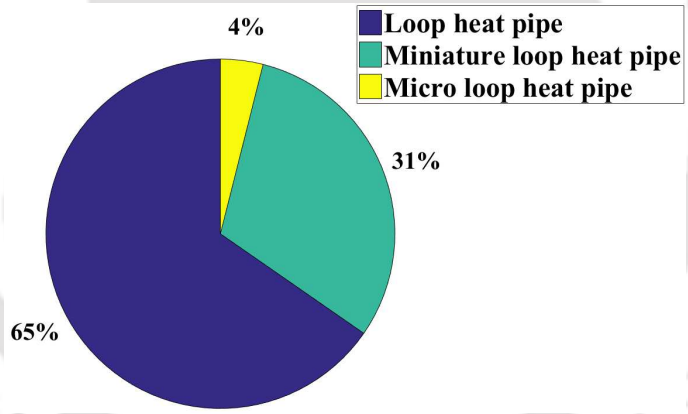

Figure 2.4: Research available for loop heat pipe based on size (Numbers are approximate)

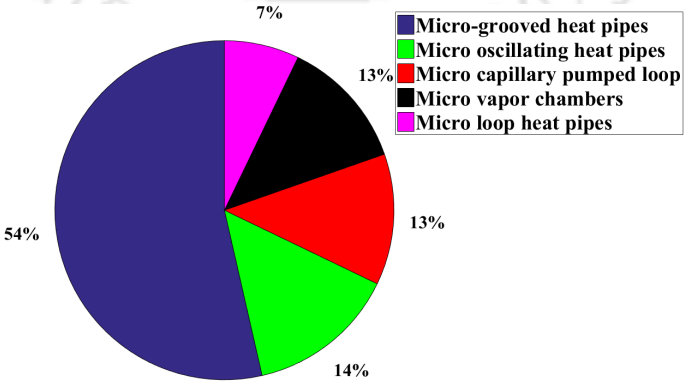

Figure 2.5: Experimental research available for different types of MEMS based micro heat pipe (data taken from Qu et al.[184])

- **Thin film evaporation model:** For thin-film evaporation model, there are several studies available in the literature, both numerical as well as experimental. However, there are still many issues in the thin-film evaporation model, which are yet to be addressed. One of the issues is that of non-conformation of numerical result with experimental data despite showing similar trends. Although a very good match was obtained by Hanchak et al.[156] and Jasvanth et al.[165], it is very few in number and has limitations. For example, the experimental data of Hanchak et al.[156] is for extremely low superheat only. Also, the methods available in the literature to calculate the initial film thickness at the end of adsorbed region (equations (6.11) and (6.12)) gives satisfactory results over a very narrow range of superheat (as will be explained in section 6.2). Thus, there is a need for a robust methodology for the estimation of initial conditions which will not only follow the physics of thin-film evaporation but will also be valid over a wide range of superheat.

2.4 Objectives

Based on the gaps in the literature, the following objectives are designed for the present study:

1. Design a new micro loop heat pipe.
2. Fabricate the micro loop heat pipe on a silicon wafer.
3. Experimentally determine its heat transport capacity, temperature reduction, thermal resistance and heat leak.
4. Formulate a mathematical model to simulate the heat transfer phenomenon of the evaporator.
5. Perform parametric simulation using the model.

Part II

Development of μlhp device

CHAPTER 3

DEVICE OPTIMISATION

In this chapter, optimization study of the device is shown. The main aim is to maximize the heat transport capacity within the limit of two-inch length of the silicon wafer. This study is based on the works of Dhillon[185] and Dhillon et al.[186]. They used a pre-optimization tool called Monotonicity analysis to simplify the problem and solved using a constrained numerical optimization algorithm. In the present study, the equations are linearized and then solved. The optimization equations are developed from the energy and pressure balance of the device, as shown in the subsequent sections.

3.1 Energy balance

Overall energy balance of the micro-evaporator yields following equations:

$$Q_{tot} = Q_{lat} + Q_v + Q_l \tag{3.1}$$

Here:

$$Q_{lat} = m' h_{fg} \tag{3.2}$$

3.2 Pressure balance

Performing the pressure balance of the device at steady state yields the following equation:

$$\Delta P_c = \Delta P_v + \Delta P_l + \Delta P_w \tag{3.3}$$

Here, the RHS of equation (3.3) represents the pressure rise of the working fluid due to capillary in evaporator channels while in LHS, the total pressure drop in different components of the device is shown.

1. **Pressure rise:** It is derived from the Young-Laplace equation.

$$\Delta P_c = \frac{\sigma \cos\theta}{D_h} \tag{3.4}$$

2. **Pressure drop:** Here, frictional pressure drop, two-phase pressure drop, pressure drop due to expansion and contraction is considered.

   (a) Pressure drop in transport channels: Here, the pressure drop is mainly due to friction. [187]:

   $$\Delta P_f = \frac{2(fRe)\mu u L}{D_h^2} + \frac{K_\infty \rho u^2}{2} \tag{3.5}$$

   (b) Pressure drop in the channels between the evaporator and compensation chamber: Here, it is mainly due to friction (given by equation (3.5)) and contraction, which is given by:

   $$\Delta P_{cont} = \frac{B\dot{m}^2}{2\rho n^2}[(1-\gamma_{cont}^2 C_{cont}^2) - 2C_{cont}(1-C_{cont})] \tag{3.6}$$

   Pressure rise due to expansion is neglected because the area ratio is less than 0.1[188].

   (c) Pressure drop in the evaporator channels: The pressure drop occurs due to single-phase friction (equation (3.5)), contraction (equation (3.6)) and two-phase friction (equation (3.7)), which is given by:

   $$\Delta P_{tp} = \frac{2(fRe)\mu u(L-L_{sp})\phi_l^2}{D_h^2} \tag{3.7}$$

Following are the lists of correlations used[185]–[189]:

$$fRe = 24(1 - 1.3553\alpha + 1.9467\alpha^2 - 1.7012\alpha^3 + 0.9564\alpha^4 - 0.2537\alpha^5)$$
$$K_\infty = 0.0697 + 1.2197\alpha + 3.3089\alpha^2 - 9.592\alpha^3 + 8.9089\alpha^4 - 2.9959\alpha^5$$
$$C_{cont} = 1 - \frac{\gamma_{cont}}{2.08(1-\gamma_{cont}) + 0.5371}$$
$$u = \frac{\dot{m}}{n\rho A}$$
$$\phi_l^2 = 1 + \frac{C\{1-\exp(-319D_h)\}}{X} + \frac{1}{X^2}$$
$$D_h = \frac{2wd}{w+d}$$
$$\alpha = \frac{w}{d}$$

The different pressure drops and pressure rise are calculated and substituted into equation (3.3) and solved for m'. The maximum theoretical heat transfer limit is then calculated using equation (3.2).

3.3 Parametric studies

After solving the equations, different parameters are varied to study their effect on the maximum heat transfer limit of the device (design shown in figure 3.1). Following are the design constraints:

I. Overall device length is capped at 5cm, since it is to be fabrication on a two-inch wafer.

II. The contact area of the condenser is kept greater than that of the evaporator (explained in section 3.4.1).

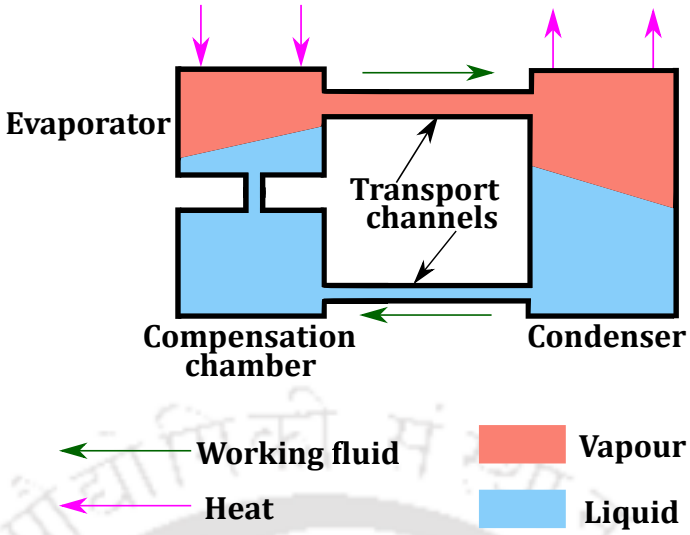

Figure 3.1: Basic idea of the MEMS-based micro loop heat pipe design

III. Width of the vapour channels is kept greater than that of liquid channels (explained in section 3.4.1).

Figure 3.2 shows the effect of the wick pore diameter (in this case width of the evaporator channels) on the heat transfer limit. It is varied from as low as 1 μm to 0.3 mm, keeping the width of the evaporator constant. From the graph, it is clear that there is an optimum value (6.4 μm width for 20 mm length of the device) for which the heat transfer rate is very high. For very low evaporator channel width, the wick pressure drop (total pressure drop at the micro-evaporator) becomes very high, which reduces the mass flow rate and hence the heat transfer limit. At very high value, the capillary pressure rise becomes low reducing the maximum heat transfer limit. The graph also clearly shows that the maximum heat transfer limit decreases with an increase in device length. Nevertheless, it does not affect the optimum evaporator channel width. That is because device length only affects the liquid and vapour transport lines pressure drop and at optimum width, only wick pressure drop dominates.

Figures 3.3 and 3.4 show the effect of vapour channel width and depth of the device on the heat transfer limit for different evaporator channel width, respectively. Keeping the space constant, the vapour channel width is increased which leads to less number of channels. This leads to an initial increase in heat transfer limit. However, after attaining a specific value, it becomes steady because of the space constraint. No such constraint is encountered while increasing the depth of the device, which is why the heat transfer limit continues to increase with an increase in depth.

In figure 3.5, the effect of the evaporator channel width on different pressure components is shown. Both the capillary pressure rise and wick pressure drop is high near the optimum width and decreases with its increase. However, the rate of decrease of wick pressure drop is high as compared to capillary pressure rise. From the graph, it is clear that at small evaporator channel width, the wick pressure drop is the primary balancing component of capillary pressure rise. At high evaporator channel width, the vapour pressure drop is the main balancing component.

The parametric study gives insight into the trends of the performance of μlhp concerning design parameters. It will be useful for design optimization as well as fabrication.

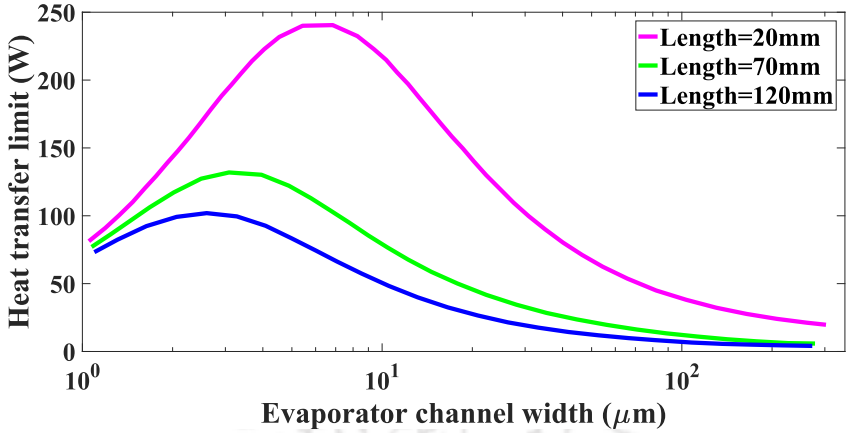

Figure 3.2: Effect of width of evaporator channels on maximum theoretical heat transfer limit

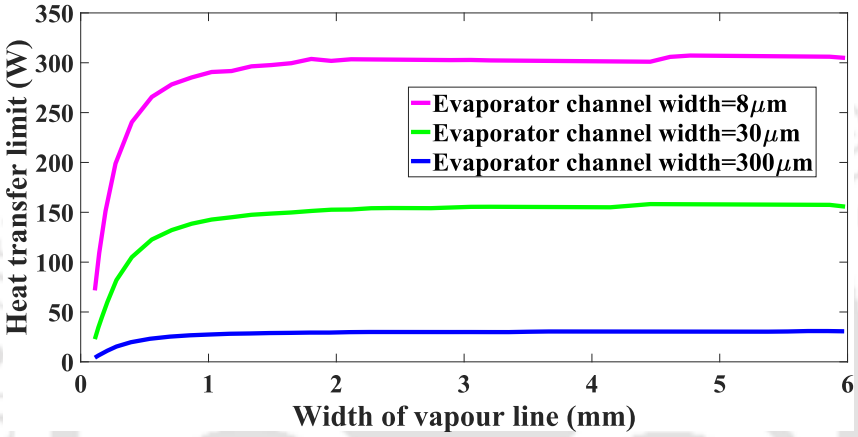

Figure 3.3: Effect of width of vapour channels on maximum theoretical heat transfer limit

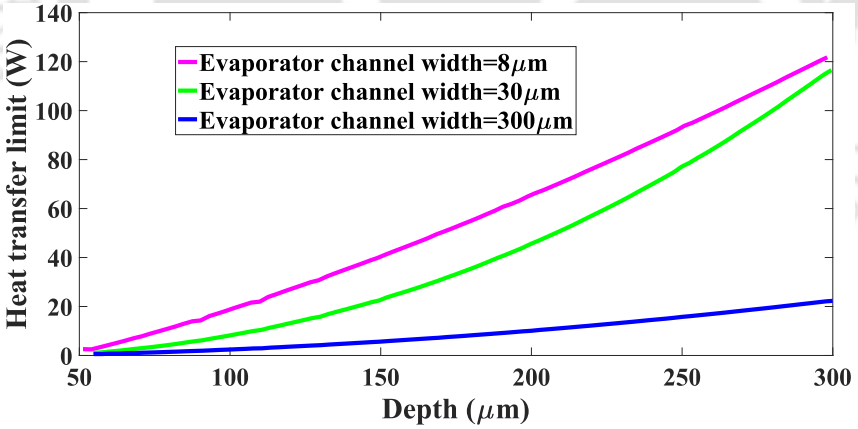

Figure 3.4: Effect of depth of the transport channels on maximum theoretical heat transfer limit

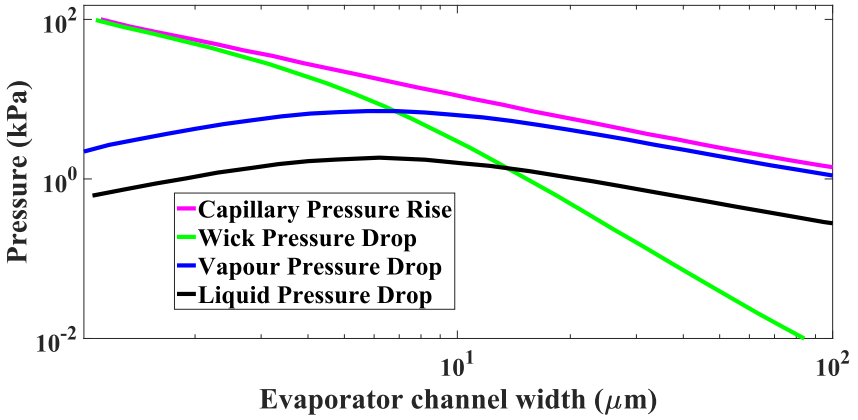

Figure 3.5: Variation of different pressure terms in the device

3.4 Design

3.4.1 Past designs

Before describing the present design, the various μlhp designs presented in the literature are shown. The following points summarise it:

- The evaporator was fabricated on a silicon wafer and provided with CPS wick[119]–[121]. It was then connected with a copper condenser tube through stainless steel transport lines.
- The device of Hsu et al.[48] had two evaporators, each having its compensation chamber. Their channel cross-section was triangular.
- Dhillon[185] fabricated three different kinds of μLHP complete with charge ports and a thermal barrier between vapour and liquid channels on a four-inch silicon wafer. To facilitate condensation, the size of the condenser was kept larger than that of the evaporator. Also, the width of the vapour channels was kept more than that of the liquid channels to minimize frictional pressure drop.
- Wang et al.[123] fabricated a unique μlhp device. Its evaporator was an empty cavity devoid of any channels to provide capillary support. Instead, capillary support was provided by the liquid channels. In the condenser, nanopillars were fabricated to assist condensation.

However, these designs had some drawbacks. They either were too complicated (having multiple evaporators or accessories like charging port or thermal barrier), or were not fabricated on a single unit (only the evaporators were fabricated on the wafer and external components were used for transport channels and condenser). The length of most of these devices were in the range of 5 to 12 cm (for MEMS-based devices only).

3.4.2 Present design

A new design is presented with optimized dimensions, and taking inspiration from the past designs with the aim to overcome most of their shortcomings.

Figure 3.6 shows the present design. As can be seen from the figure, the device is comparatively simple, does not have any charge ports or thermal barrier. Its cross-section is 35×17 mm. It has an evaporator (5×5 mm), condenser (7×7 mm) and a compensation chamber (5×5 mm). Multiple transport channels are provided to reduce the mass flow rate in a single microchannel. The evaporator consists of numerous channels of width 10 µm. Working fluid is charged directly over the compensation chamber. Shorter channels connecting the evaporator and compensation chamber compared to the liquid channels (connecting between the compensation chamber and condenser) ensure that the working fluid directly enters the evaporator. Enough distance is also maintained between the vapour and liquid channels so that heat does not leach from the vapour into the liquid channel, thus, eliminating the need for a thermal barrier. Table 3.1 shows the dimensions of the proposed μlhp device fabricated on a two-inch silicon wafer.

We claim, to the best of our knowledge that our design ranks second in terms of length. The credit of fabricating the smallest μLHP goes to Wang et al.[123], having an overall length of 2 cm. But their fabrication technique was comparatively complicated, as shown in table 4.1.

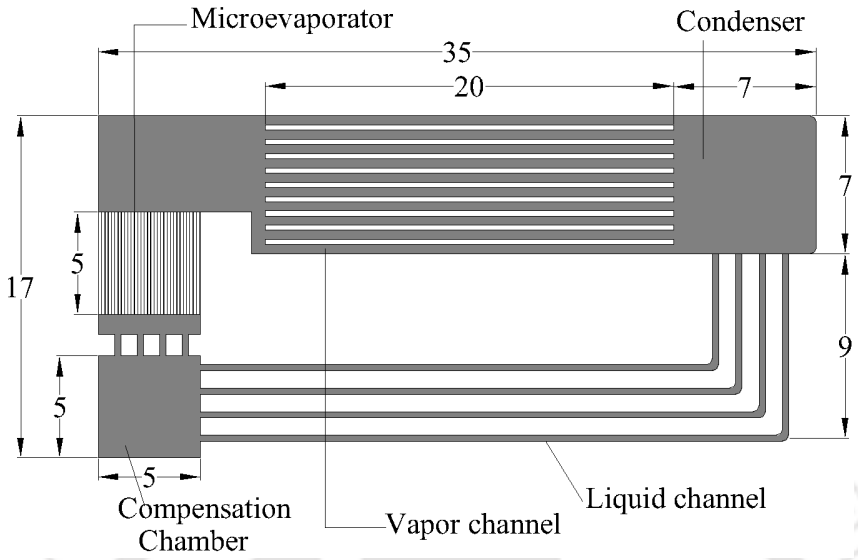

Figure 3.6: Micro loop heat pipe (All dimensions are in *mm*)

Table 3.1: Dimension of different components of μLHP device

COMPONENT	DIMENSION (μm)
Compensation Chamber	Length: 5000 Width: 5000 Depth: 150–160
Condenser	Length: 7000 Width: 7000 Depth: 150–160
Evaporator channels	No. of channels: 125 Length: 5000 Width: 10 Depth: 150–160
Vapour channels	No. of channels: 10 Length: 20000 Width: 600–650 Depth: 150–160
Liquid channels	No. of channels: 4 Length: 28000–37000 Width: 450–500 Depth: 150–160

CHAPTER 4

DEVICE FABRICATION AND CHARGING

ONE of the main problems encountered in the μlhp field is the lack of easy fabrication techniques and charging method [190]. The methodology is complicated and costly because of the numerous intermediate steps involved. This lowers the probability of successful fabrication. This chapter provides a brief summary of the different steps involved in the fabrication and charging and discusses in detail, the methodology used in the present study.

4.1 Fabrication basics

Figure 4.1 shows the main steps involved in the fabrication of μlhp on a silicon wafer. They are: cleaning, deposition/formation of a mask layer, pattern transfer, generation of grooves over the pattern and sealing of the fabricated device.

1. **Cleaning:** After the selection of the wafer, it is crucial to get rid of all contaminants, if any, present on it. These contaminants generally can be grouped into particulates, metallic and organic contaminants. Besides that, sometimes a thin layer of oxide layer will also be present. If not removed before fabrication, these contaminants pose a risk of not only damaging the equipment and other samples, but also increases the chances of failure in fabrication.

   Several recipes or chemical mixtures are available to clean Si wafers. The most popular is the piranha clean and RCA clean.

   - Piranha clean: Its recipe consists of H_2SO_4 and H_2O_2 mixed in 4:1 ratio. The mixture is kept at 80–120°C (the reaction is self-heating). H_2SO_4 reduces any organic matter into carbon and H_2O_2 then oxidizes it to CO or CO_2, which leaves the solution, thereby removing the contaminant. It is also used as a pre-clean to RCA.
   - RCA clean: It consists of three steps.
     (a) RCA1: The first steps removes particulates and organics. The recipe consists of NH_4OH, H_2O_2 and water mixed in the ratio of 1:1:5 or 1:2:7. The temperature is kept at 40–80°C. H_2O_2 oxidises the contaminants and NH_4OH forms soluble complexes. The particles are removed by OH^- ions.

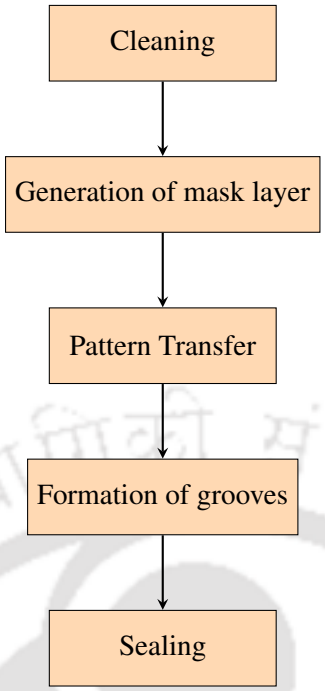

Figure 4.1: Flow diagram showing major processes involved in the fabrication process

(b) RCA2: The second step removes metal. The recipe is the same as RCA1 except NH_4OH is replaced with HCl and mixed in the ratio 1:1:6 or 1:2:8. The mixture is heated at a temperature between 70–80°C. The role of H_2O_2 is the same as in RCA1. HCl forms chloride salt which is soluble with water and hence easily removed.

(c) DHF: The third step removes the chemical oxide, which is formed due to H_2O_2. It is done with a dilute solution of HF (1:50 or 1:100).

Besides this, it is also essential to clean the wafers with a separate solution of acetone, propanol and DI water in that order after every significant step shown in figure 4.1 and then drying with a nitrogen gun.

2. **Generation of mask layer:** After cleaning, it is imperative to protect the pure native Si surface. This is done by generating a protective layer (generally SiO_2) over it. The process generally used for this is the wet oxidation process as its growth rate of the SiO_2 layer is high, compared to other processes like the dry oxidation. Following is the chemical reaction involved:

$$Si + 2H_2O \xrightarrow{900\text{-}1000\,^{\circ}C} SiO_2 + 2H_2$$

3. **Pattern transfer:** This is the step where the device design is imprinted over the wafer. Two methods are generally used: photolithography or electron lithography depending on whether photons or electrons are used.

   - Photolithography: Here, photons are used to transfer the pattern over the wafer. The wavelength used is generally 248 nm (deep-UV). The wafer is at first, coated with

a sensitive material (sensitive only to 248 nm photons) called photoresist. It is then exposed to incident photons through a mask, which is used to control the amount of incident photon and area to be exposed. This mask is either a negative or positive image of the design (depending on the type of photoresist used). This method is used when the dimension of the smallest feature is greater than 0.35 μm.

- Electron lithography: This method is used when the smallest feature is less than 0.35 μm (often of the order of nm). Here the pattern is directly written over the wafer using electrons (wavelength = 0.62Å) without the use of any mask. Since the wavelength of electrons is less than that of photons, this process provides better resolution than photolithography.

4. **Formation of grooves:** This methodology is the subtracting fabrication or etching (both isotropic as well as anisotropic). It involves removing materials from the selected area of the wafer to imprint the design over it permanently. Depending on the type of etchant used, it is of two types:

   - Wet etching: This is used when etchant available is an acid or base. Some of the most common etchants are KOH, TMAH (Tetramethylammonium hydroxide) and HNA. The mechanism involves three steps. First is the transport of the etchant to the wafer surface, next is the chemical reaction between the etchant and the surface (actual etching) and finally removal of the by-products away from the surface, so that the cycle may continue.
   - Dry etching: It involves bombardment of ions to remove the material from the surface. It is used when the etching needs to be highly anisotropic (directional). A typical example is the deep reactive ion etching (DRIE).

   For CMOS compatible anisotropic wet etching, the etchant used is TMAH (figure 4.2(a)).

5. **Sealing:** This is generally the last step in fabrication. PDMS (Polydimethylsiloxane) is used as the most common material used to bond a transparent or non-transparent material over the silicon surface. Its molecular structure is shown in figure 4.2(b).

4.2 Charging basics

After fabrication, the next challenging task is the charging of MEMS-based heat pipes. Its first step is the removal of non–condensable gas (NCG) from the device (since it will degrade the thermal

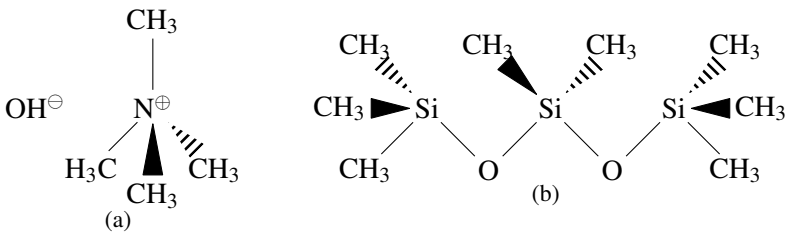

Figure 4.2: Molecular structure of (a)TMAH and (b)PDMS

performance, if allowed to remain in the device). This is done by evacuating the device to very high vacuum of the order of 10^{-4} to 10^{-2} torr. After that, the device is charged with an appropriate amount of working fluid. Since amount of fluid involved is extremely low (of the order 10 to 100 µl) difficulty is encountered in controlling the flow of liquid and then sealing.

Peterson et al.[191] summarised the three different charging methodologies used. The first is similar to that used for conventional heat pipes, *i.e.* charging from an already filled chamber after evacuating the device. The second consists of evacuating the device in a high-pressure chamber. Then, introducing a pre-determined amount of working fluid in the chamber and heating it to supercritical point. At this point, the vapour will redistribute uniformly in the chamber and the device. The device is sealed while inside the chamber. The charged device is then taken out of the chamber. The third is using a charging trough to inject the working fluid inside the device kept in a vacuum chamber after evacuating it. As the pressure approaches the saturation point of that temperature, the vapour wicks into the device. The device is then sealed and ready for application. Cao et al.[192] also demonstrated three different charging procedures: 'High vacuum bypass method', 'Sealed reservoir method' and 'Microsyringe method'. They found only the third method is feasible for charging micro/miniature devices due to factors like back-flow, low accuracy associated with the other two methods. The microsyringe method consists of using a syringe to fill the device using a T-junction valve after evacuation.Li et al.[193] used a peristaltic pump to fill the device after vacuuming and a hot clamp to seal. In a seperate study, a low melting point alloy is used to seal[194]. Wang et al.[195] showed the 'Double air pumping charge method' which consists of completely filling the device with fluid after evacuating and then using the vacuum pump to purge the excess working fluid again from the device and then sealing. Another notable method was that of Ababneh et al.[196]. It consists of evacuating the device to a pressure lower than the saturation pressure of filling temperature. Then the working fluid is passed through multiple distillations to ensure that it is free of any dissolved gas or other impurities. Next, the working fluid is introduced into the device. The fluid flashes and the device is sealed.

Dhillon and Pissano[124] proposed a unique method, especially for charging μLHPs. Instead of using vacuum pumps, they passed vapour through it. The high velocity of the vapour purges the device of any NCGs. Next, the device is allowed to cool, which in turn condenses the vapour into liquid. Finally, the device is permanently sealed.

4.3 Present fabrication and charging methodology

Researchers have adopted different methodologies to fabricate and charge the μlhp according to their respective size and applications. As can be seen from table 4.1, most of them have numerous steps and complicated procedures. Hence, in this study, a simplified fabrication procedure is put forward.

4.3.1 Fabrication

The fabrication methodology is developed from Singh et al.[197]. The basic process consists of cleaning (RCA cleaning), generation of the mask layer (wet oxidation), pattern transfer (photolithography), the formation of rectangular grooves (chemical etching) and sealing with glass

Table 4.1: Details of fabrication methodologies for μLHP

Researchers	Si Orientation	Smallest features (μm)	Fabrication methodology
[120]	$\langle 100 \rangle$	5	Thermal oxidation→Phosphorus diffusion→ LPCVD→Photolithography→KOH etch→ Electron beam evaporation→ Photon assisted electrochemical etch
[48]	$\langle 100 \rangle$	47	Oxidation→Photolithography→ BOE etch→KOH etch→Bonding
[185]	$\langle 100 \rangle$	32	LPCVD→Anneal→Photolithography→ Plasma etch→DRIE→Wet etch→Bonding
[123]	NA	0.15	Electron beam lithography→ Plasma etch→Two step bonding

using PDMS bonding (as shown in figure 4.1). The micro loop heat pipe device is fabricated on a 2-inch silicon wafer having the following properties:

Type : p
Resistivity : 1-5 Ω-cm
Orientation: $\langle 1\,1\,0 \rangle$
Thickness : 250 µm

Before the start of the fabrication process, the wafer is RCA cleaned to remove any organic contamination, oxide layer and ionic contamination. Then a layer of SiO_2 is generated over it. The next step involves the measurement of the oxide layer using an Ellipsometer. The measured layer should be between 700 to 1000 nm. Next, the following procedures are followed:

- **Photolithography**: Following are the steps in this process:
  1. The wafer is heated at 150°C for 15 minutes.
  2. Positive photoresist (PPR) is applied on the wafer and then rotated at 300 rpm for 15 seconds and then 3000 rpm for 30 seconds.
  3. The PPR coated wafer is heated at 100°C for 3 minutes.
  4. The wafer is exposed to UV light for 8 seconds at 13.8 doses using the mask aligner (DSA). (Note: The mask is designed using AutoCAD and then printed, or if the feature is comparatively small then it is directly developed on a glass plate using a Laser Writer).
  5. The wafer is treated with a PPR developer (MF319) for 25 seconds.
  6. The wafer is cleaned using deionized (DI) water.
  7. The wafer is heated at 95°C for 5-10 minutes.

- **Etching**: The setup used is shown in figure 4.3. Following are the steps:

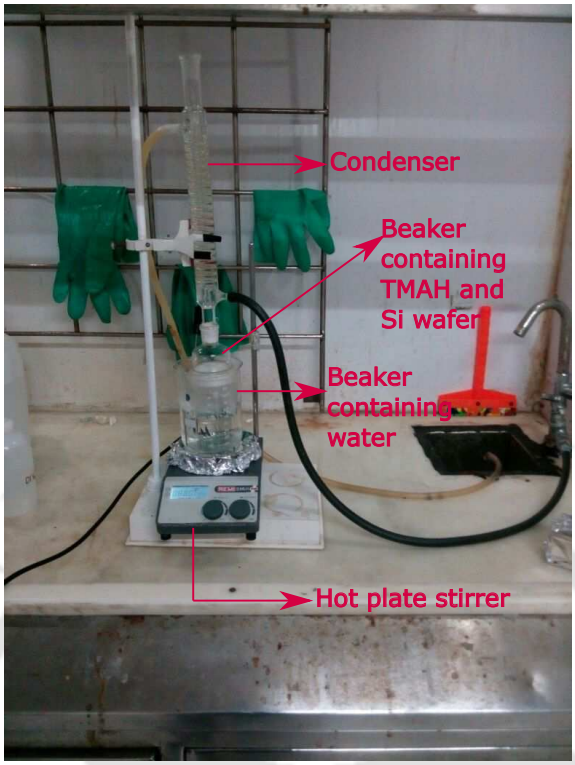

Figure 4.3: Wet etch set-up

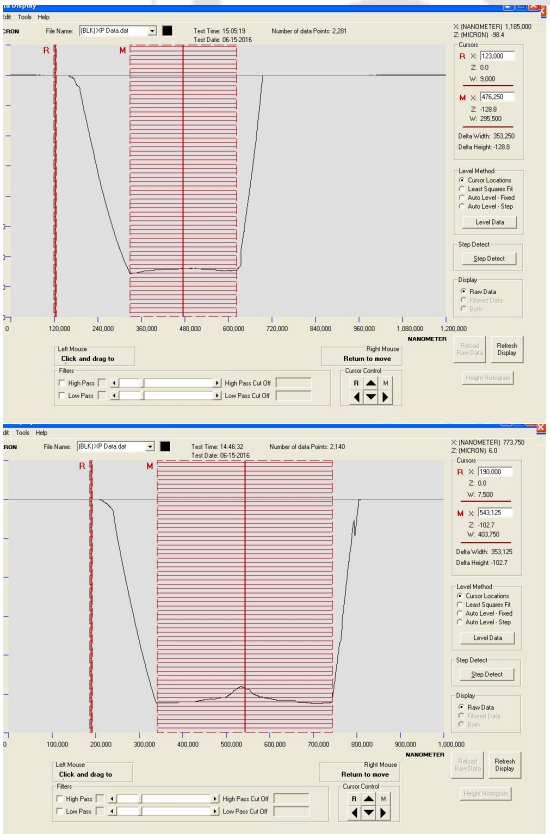

Figure 4.4: Channels shown by Profilometer

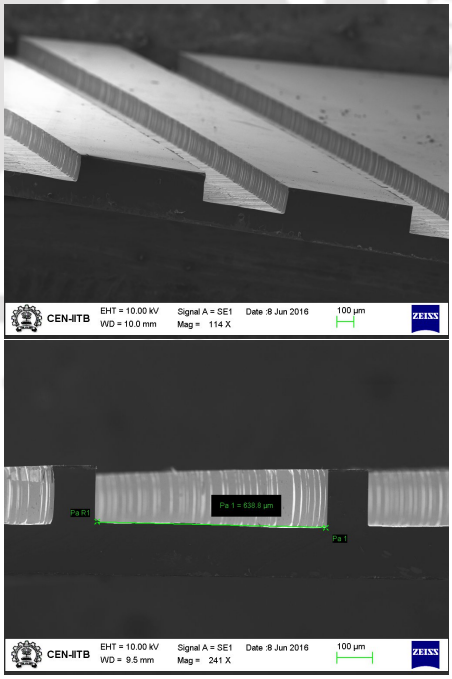

Figure 4.5: Channels shown through Scanning Electron Microscope

1. The exposed side of the wafer is treated with buffered oxide etch (BOE) solution to remove the SiO_2 layer so as to expose the Si layer underneath. (Note: The SiO_2 layer is removed from that area which contained the image of the device from the mask).
2. The PPR is removed from the mask using acetone.
3. The wafer is cleaned using deionized (DI) water.
4. The wafer is etched using a solution of Tetra-methyl-ammonium hydroxide (TMAH) kept at a temperature of 70-80°C for a specific amount of time depending on the depth required.

Based on an etch rate of 1.067 $\mu m/min$, the etched depth got was of the order of 160 μm. This is confirmed either with a Profilometer (figure 4.4) or using a Scanning Electron Microscope (figure 4.5).

- **Bonding**:

1. Polydimethylsiloxane (PDMS) and a curing agent are mixed in 10:1 ratio.
2. The mixture is then subjected to vacuum condition to remove any dissolved gas.
3. The mixture is then applied on the cover plate uniformly and rotated at 3000 rpm for 30 seconds and then 1500 rpm for 15 seconds.
4. The cover plate is then attached to the wafer and sealed.

Although, rotating at uniform speed ensures the mixture spreads uniformly and forms a mono-layer, 10 µm is subtracted from the channel depth to account for unwanted PDMS in them. Since the depth of the channels is 150 µm, it will not affect the flow of fluid through it.

Figure 4.6 shows the detailed process flow of the fabrication technique and figure 4.7 shows the fabricated μlhp device, its size compared with a ₹ 5 coin (having a diameter of 1 inch). However, despite best effort, some deviations were obtained. Furthermore, since, it is a multi-step methodology, errors sustained in one step will always carry over to the next one. Some example of deviation is the width of the liquid channel was intended to be 400 μm. After photolithography, the dimension of the imprinted liquid channel on the wafer was between 410–430 μm (figure 4.8(a)) and after etching it became 450–500 μm (figure 4.8(b)).

4.3.2 Charging methodology

Figure 4.9 shows the block diagram of the charge station. Before charging, thermocouples and micrometer valve are attached to the device. Following steps are involved:

1. **Removal of non-condensable gas:** This is achieved by the use of a vacuum pump (rotary vane pump). First, valves V1 and V2 are opened and V3 is closed. Then vacuum (up to 0.13 Pa) is created in the device by the pump which purges the non-condensable gas and other impurities. After its removal, valves V1 and V2 are closed and the vacuum pump is disconnected. Figure 4.10 shows the set up of the device for this step.

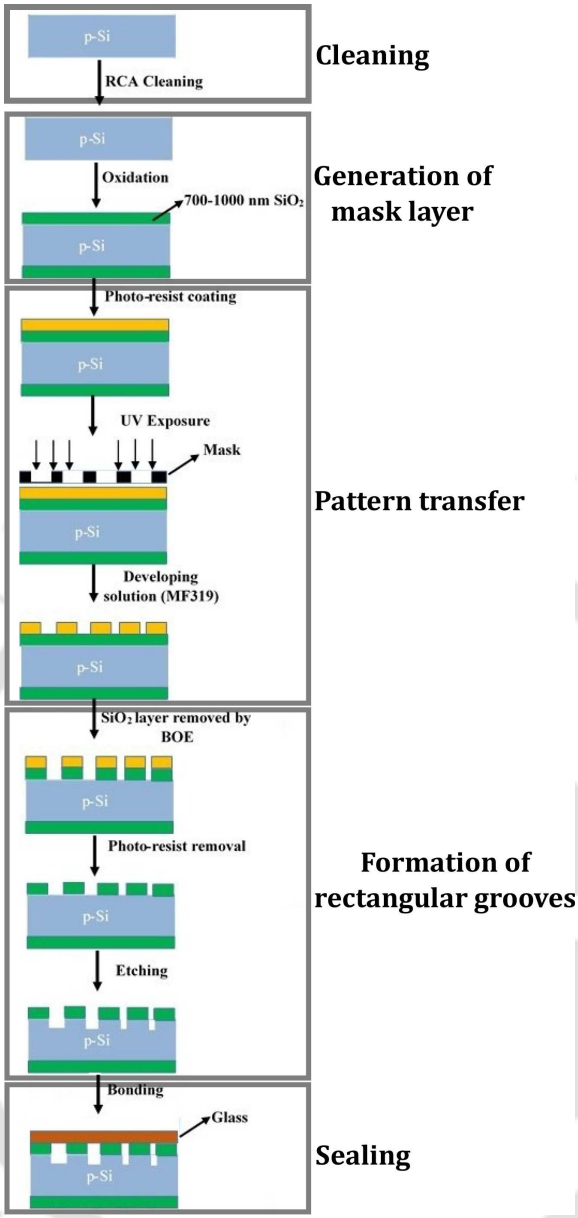

Figure 4.6: Process flow of the Fabrication Technique

2. **Filling the device with working fluid:** Keeping V1 closed, V2 and V3 are opened. Because of the vacuum in the device, it immediately begins to fill with the working fluid. Valves V2 and V3 are closed after the required amount of fluid enters the system, then, the reservoir is disconnected. Figure 4.11 shows the setup of the device for this step.

In all these steps, care must be taken so that air bubbles do not enter the device.

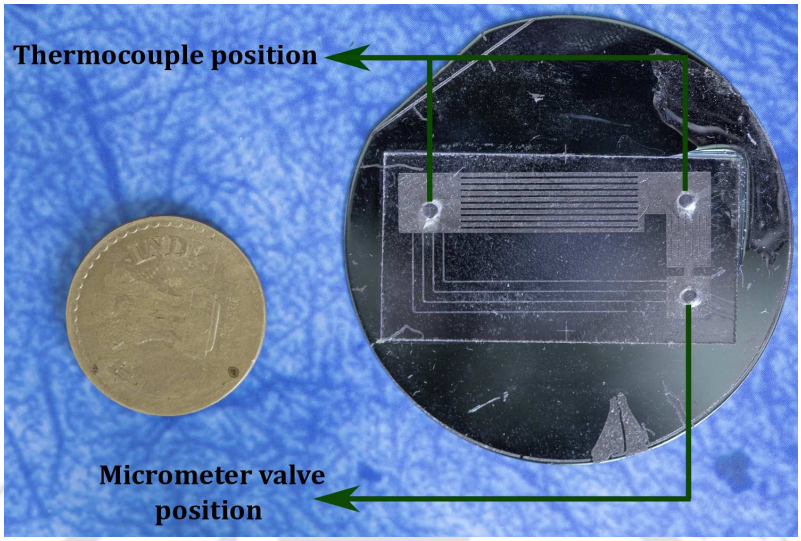

Figure 4.7: Fabricated test device

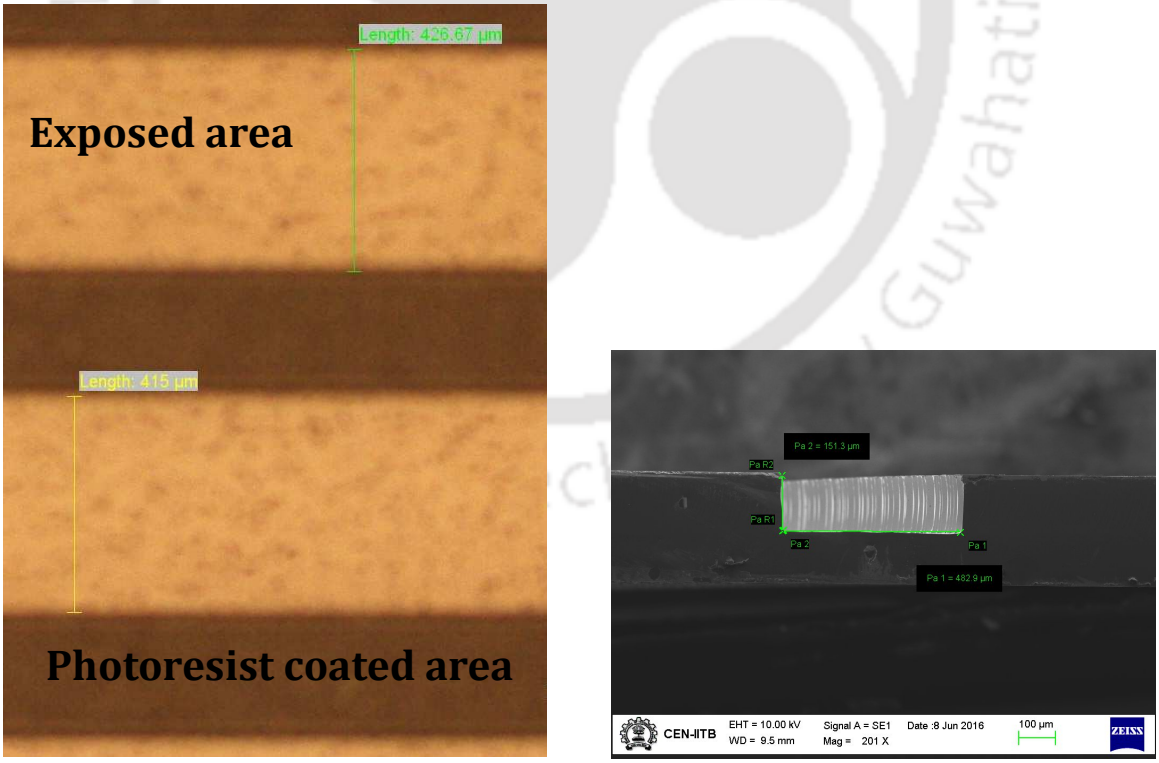

(a) (b)

Figure 4.8: Measured dimension of the liquid channel after (a) Photolithography and (b) Etching

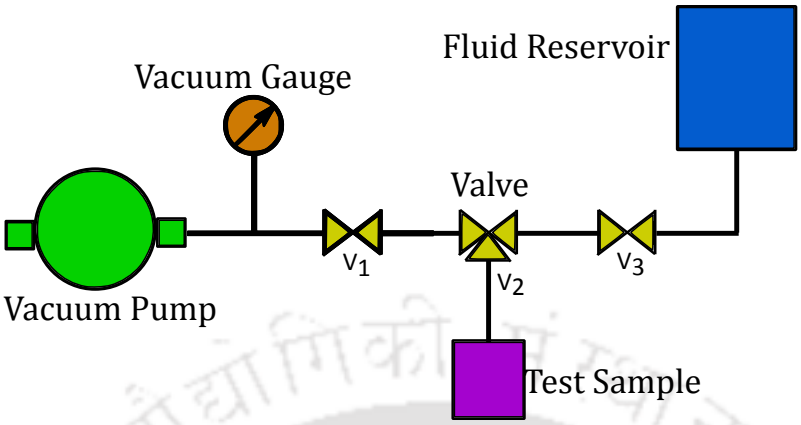

Figure 4.9: Charging Station

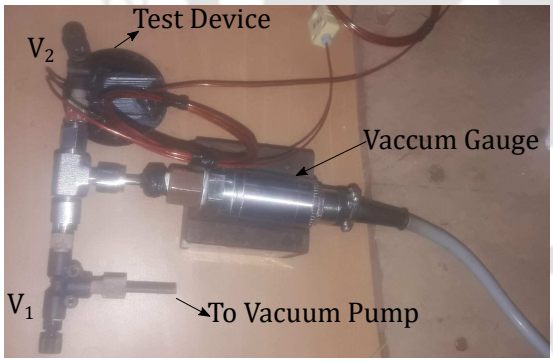

Figure 4.10: Setup of the device for removal of non condensable gas

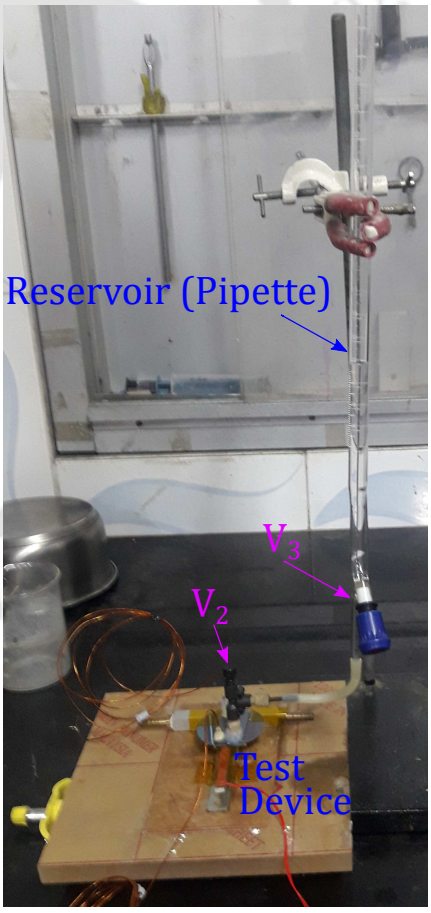

Figure 4.11: Setup of the device for filling with working fluid

CHAPTER 5

PERFORMANCE TESTING

BEFORE charging, a suitable working fluid needs to be selected. For this, a figure of merit parameter is used, as explained in section 2.1.2. In this study, a new figure of merit ($(h_l)_{max}$) is proposed given by equation (8.7). Its derivation and detailed analysis are described in chapter 8. Figure 5.1 shows its value at wide range of saturation temperature (-50 to 200°C) using different working fluids. From the figure it is clear that ammonia is comparatively the best working fluid. However, it has very high vapour pressure and may subject the device to deformative force at high temperature. Hence, the second best working fluid is selected *i.e* methanol.

After charging the device with methanol, it is then connected with a strip heater in the evaporator side and a heat sink in the condenser side as shown in figure 5.2. Methanol was selected as the working fluid because of its low boiling point. Figure 5.3 shows the block diagram of the experimental setup. It consists of a DC power supply, a data acquisition system, gear pump and a constant temperature bath. Using the DC power supply, heat load to the device is controlled and temperature reading is taken through the thermocouples connected at both the evaporator and condenser side. The temperature of the coolant in the heat sink is kept at a constant 15°C. Figure 5.4 shows the actual experimental setup.

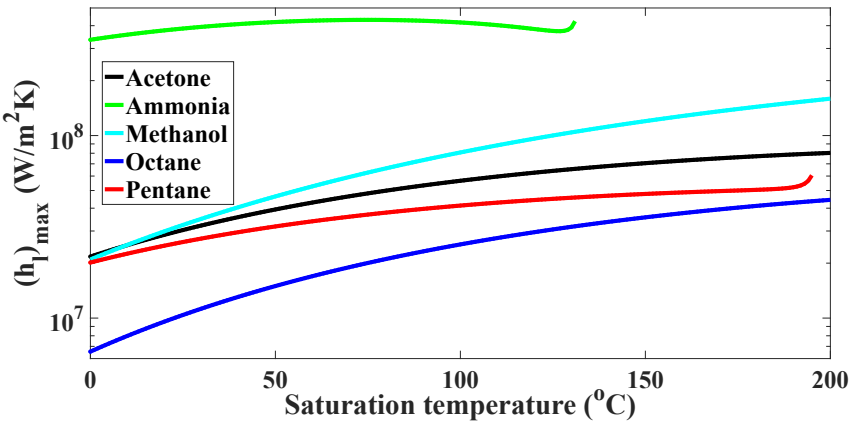

Figure 5.1: Performance comparison of various working fluids

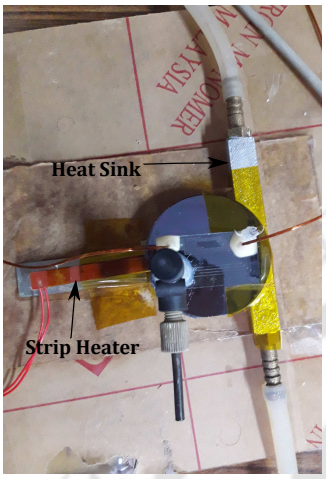

Figure 5.2: Assembled device

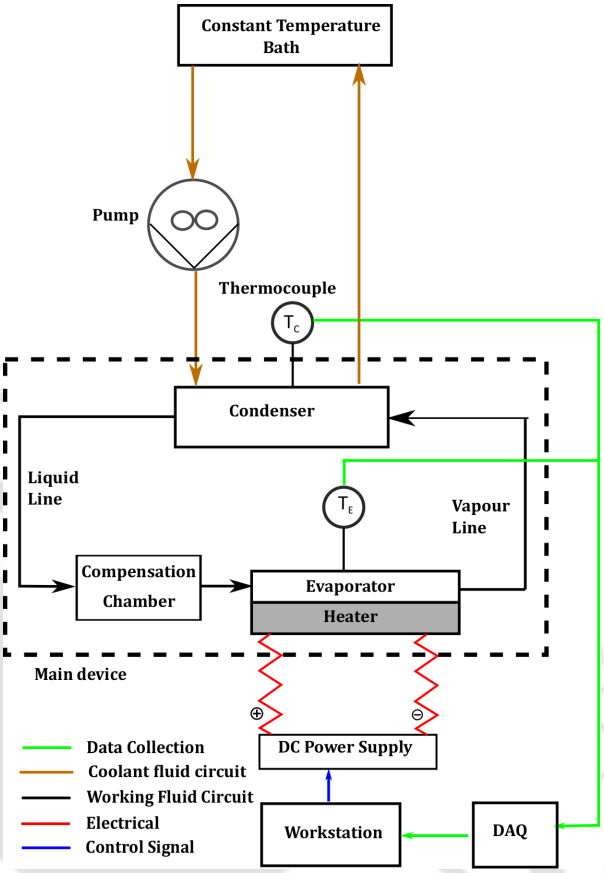

Figure 5.3: Block diagram of the experimental setup

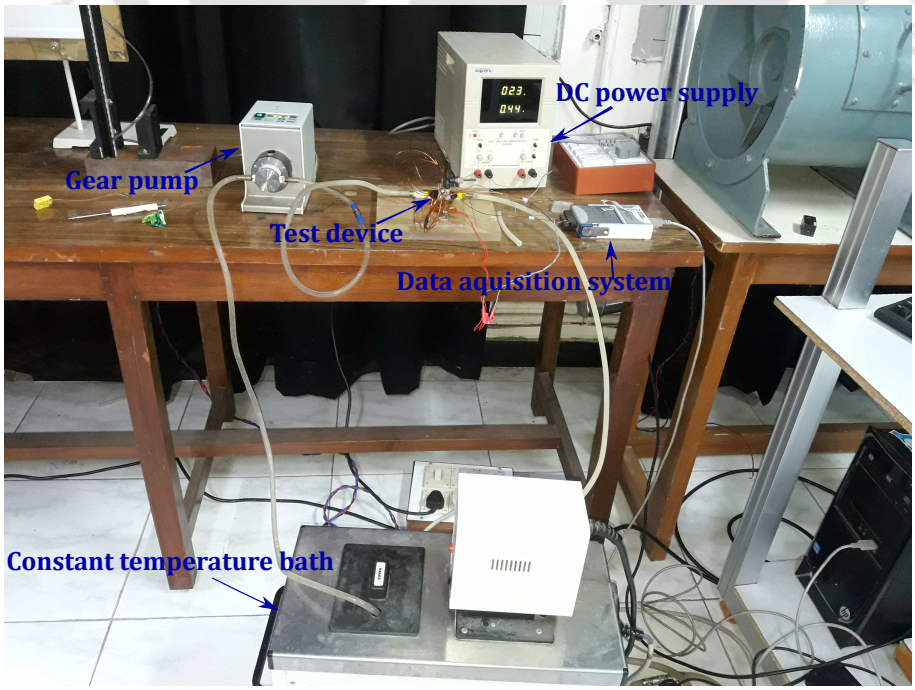

Figure 5.4: Entire experimental setup

Figure 5.5 shows the variation of evaporator and condenser temperatures with time. Heat load is varied slowly, so, that it does not damage the strip heater. The μlhp device starts between 5–10 minutes mark when there is a jump in temperature of condenser. This is because the vapour has entered the condenser from the evaporator. The corresponding heat load is 1.5–4 W.

The performance of the μlhp device is measured by comparing it with an empty silicon wafer, thus basically pitting it against a pure conduction block. Figure 5.6 shows the comparison. At 3.78 W input heat, the maximum surface temperature of the empty device is recorded to be 70°C while that of the filled μlhp device is 41.4°C. Hence, using the μlhp device, temperature reduction of 28.6°C is attained. Figure 5.7 shows the plot of thermal resistance (calculated from equation 5.1) with the heat load. As expected, it decreases monotonically with the heat load. At a heat load of 4.7 W, the thermal resistance is 3.61 °C/W. Using equation (5.2), the effective thermal conductivity of the device is calculated. Figure 5.8 shows its variation. As can be seen from this figure its value approaches 360 W/mK around 5 W heat load. Compared to the values obtained in the literature (around 200 to 230 W/mK[191], [198], [199]), the present design has a much higher thermal conductance.

$$R_{dev} = \frac{T_{evap} - T_{cond}}{Q_{applied}} \tag{5.1}$$

$$k_{eff} = \frac{L_{dev}}{Area_{evap}\, R_{dev}} \tag{5.2}$$

Equation (5.3) shows the thermal resistance uncertainty using Kline and McClintock uncertainty methodology. The uncertainty in temperature measurement is 2% and that for the power source is 1% for both voltage and current. Table 5.1 shows the uncertainty in the calculated thermal resistance. As can be seen from the table, the uncertainty decreases with an increase in the thermal load.

$$\delta R = R\sqrt{\left(\frac{\delta T_{diff}}{T_{diff}}\right)^2 + \left(\frac{\delta V}{V}\right)^2 + \left(\frac{\delta I}{I}\right)^2} \tag{5.3}$$

Where:

$$T_{diff} = T_{evap} - T_{cond}$$

$$\dot{Q} = VI$$

Table 5.1: Uncertainty in calculated thermal resistance

R (°C/W)	δR (°C/W)	% error
5.17	1.25	24.3
4.03	0.652	16.2
4.48	0.578	12.9
4.18	0.488	11.7
3.99	0.436	10.9
4.11	0.361	8.78
3.61	0.312	8.65

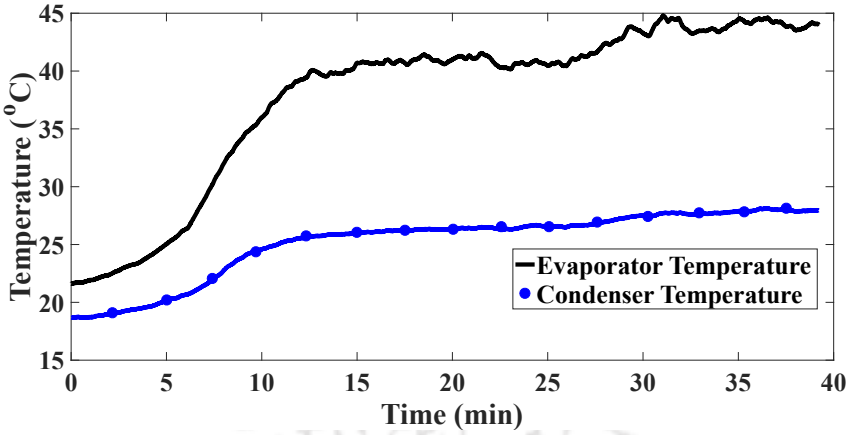

Figure 5.5: Temperature profile of evaporator and condenser side of the device

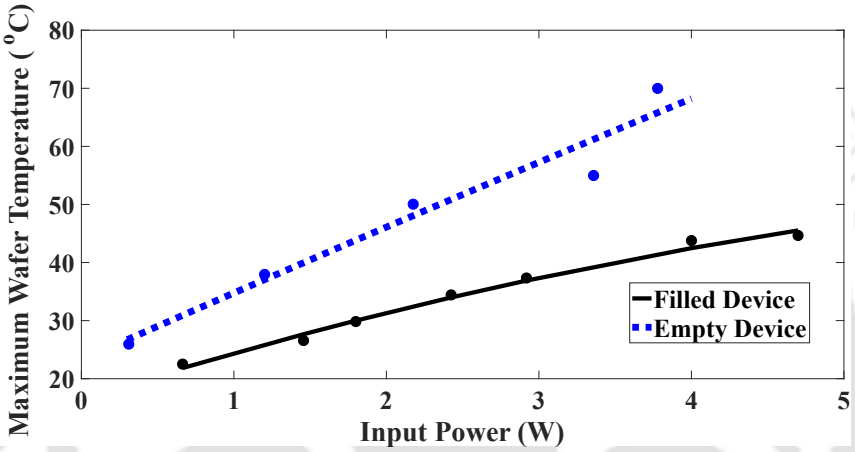

Figure 5.6: Performance of the μlhp device compared with a conduction block

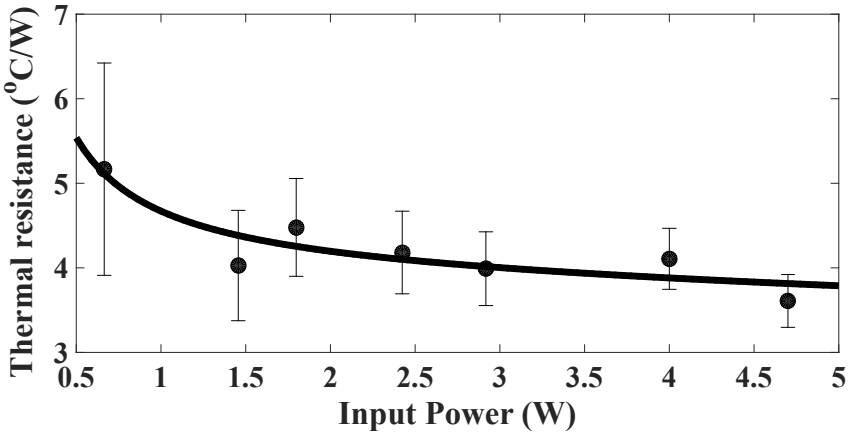

Figure 5.7: Variation of thermal resistance of the μlhp device with heat load

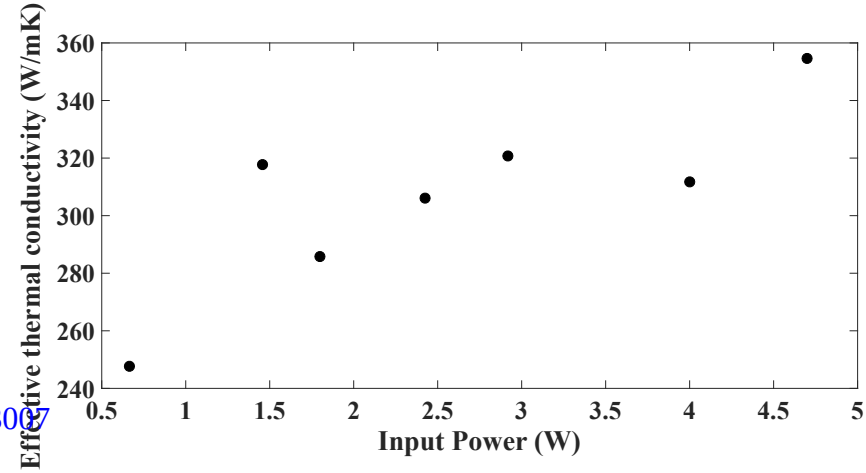

Figure 5.8: Corresponding variation of effective thermal conductivity with heat load

Another parameter is the amount of heat that is being back-conducted from the evaporator towards the compensation chamber/liquid channels. It is commonly referred to as the "Heat leak"(Q_{hl}). As can be seen from equation (5.4), it is the sum of heat removed due to liquid sub-cooling at the condenser ($Q_{cons(sub)}$) and heat loss to the ambient from liquid lines ($Q_{ll\text{-}a}$) and evaporator ($Q_{evap\text{-}a}$)[126].

$$Q_{hl} = Q_{cond(sub)} + Q_{ll-a} + Q_{evap-a} \tag{5.4}$$

Where:

$$Q_{cond(sub)} = m' C_P \left(T_{cond(in)} - T_{cond(out)}\right)$$

$$m' = \frac{Q_l}{\lambda + C_p(T_{evap(out)} - T_{ll(out)})}$$

Its variation with heat load is shown in figure 5.9. Here, the heat loss from the transport lines to the ambient is neglected because of its small cross-section. As explained in Shioga et al.[126], the heat leak is linearly varying with the heat load from 5 to 40 mW. To estimate the heat loss to the ambient, amount of heat transported by the device is calculated. It is computed by taking the difference in heat load between the filled and empty device under the same wafer temperature. Figure 5.10 shows the linear variation of heat transported by the device with the evaporator temperature. This figure clearly show that there is a significant increase in the heat transport through the device.

To better explain the design benefits of the present study, its thermal resistance is compared with other types of MEMS-based micro heat pipes, working on methanol (figure 5.11). Dimensions of the compared devices are shown in table 5.2, along with their corresponding source. As can be seen from figure 5.11, with the exception of Hsu et al.[48] device, all the other devices have higher thermal resistance than our design. This is because in case of Hsu et al.[48], their device is almost twice as large as our device, hence, will hold higher quantity of working fluid. Thus, their device will have lower thermal resistance than our device. However, the figure clearly shows that its thermal resistance start increasing after 2 W and its value become greater than that of our device at higher heat load. This is because of increase in its heat leak. This problem was also faced by Phan and Nagano[183] for their miniature loop heat pipe device. As is clear from figure 5.9 the present design has very low heat leak.

Table 5.2: Characteristics of the MEMS devices from literature

References	Device type	Dimensions (mm)
Hsu et al.[48]	Micro loop heat pipe	Hydraulic diameter (wick): 0.067 Overall length: 60
Lin et al.[200]	Polymer micro heat pipe	Hydraulic diameter: 2 Overall length: 56
Peterson et al.[191]	Grooved micro heat pipe (Rectangular)	Hydraulic diameter: 0.0576 Overall length: 20
Peterson et al.[191]	Grooved micro heat pipe (Triangular)	Hydraulic diameter: 0.06 Overall length: 20

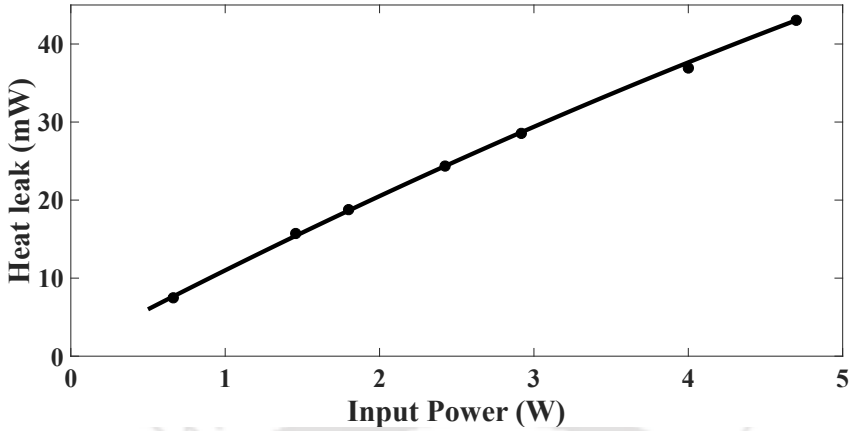

Figure 5.9: Dependence of heat leak with heat load

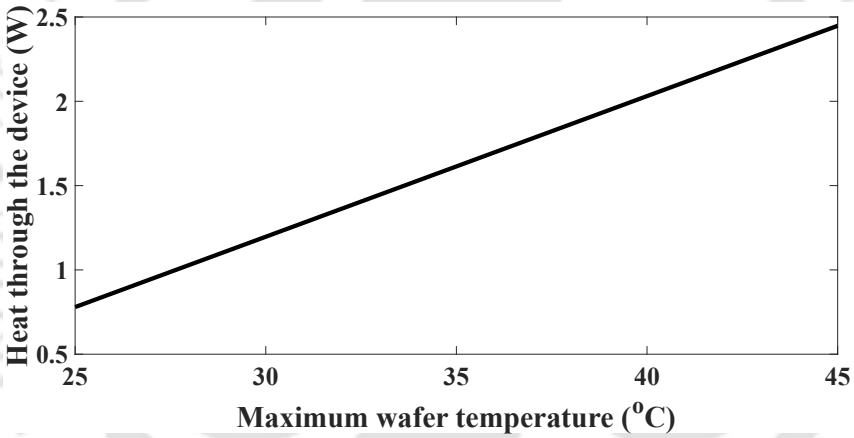

Figure 5.10: Heat loss calibration curve

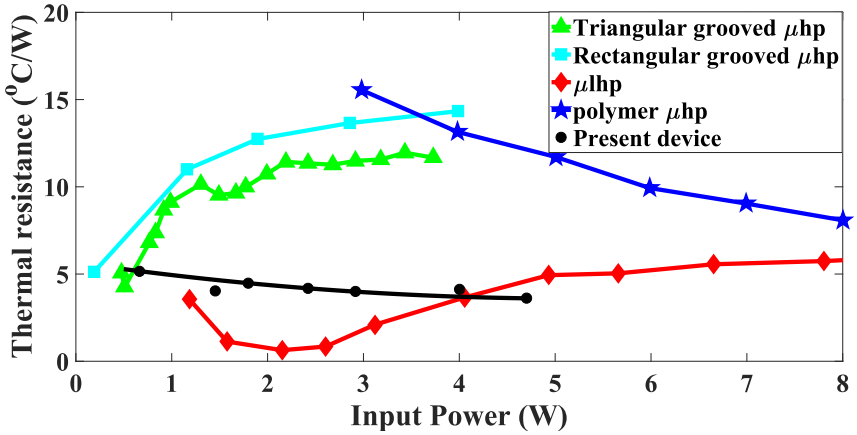

Figure 5.11: Comparison of the present device with different type of MEMS heat pipe from the literature

Part III

Thin film evaporation model

CHAPTER 6

MATHEMATICAL MODEL

In this chapter, a new theoretical model is described to model the liquid-vapour meniscus formed in the microchannels of device evaporator (shown in figure 6.1). As explained in chapter 1, this liquid-vapour interface is divided into three regions called adsorbed, thin-film and capillary region. Figure 6.2 shows the thin-film region in detail. The following assumptions are made in its mathematical modelling:

a The flow is laminar and has attained a steady state.

b Both the liquid and vapour phases are incompressible.

c Properties of the fluid are constant.

d Convective terms in the momentum equation are negligible.

e Evaporation is restricted to thin-film region only.

Since, most of the heat transfer takes place in the thin-film region, it is practical to restrict the problem statement to thin-film region only. Hence, such type of modelling is known as 'Thin-film evaporation theory'.

6.1 Governing Equations

The governing equations of thin-film evaporation are given below [142], [150], [156], [160]. The derivations are given in the appendix.

6.1.1 Thin-film thickness

Following is its governing equation:

$$\frac{d^3\delta}{dx^3} = \frac{3(\frac{d\delta}{dx})(\frac{d^2\delta}{dx^2})^2}{\{1+(\frac{d\delta}{dx})^2\}} - \frac{1}{\sigma}\left(\frac{dP_d}{dx} + \frac{dP_l}{dx}\right)\left\{1+\left(\frac{d\delta}{dx}\right)^2\right\}^{3/2} \tag{6.1}$$

Here, the vapour pressure gradient is neglected as its effect on the thin film profile is negligible (results shown in the appendix).

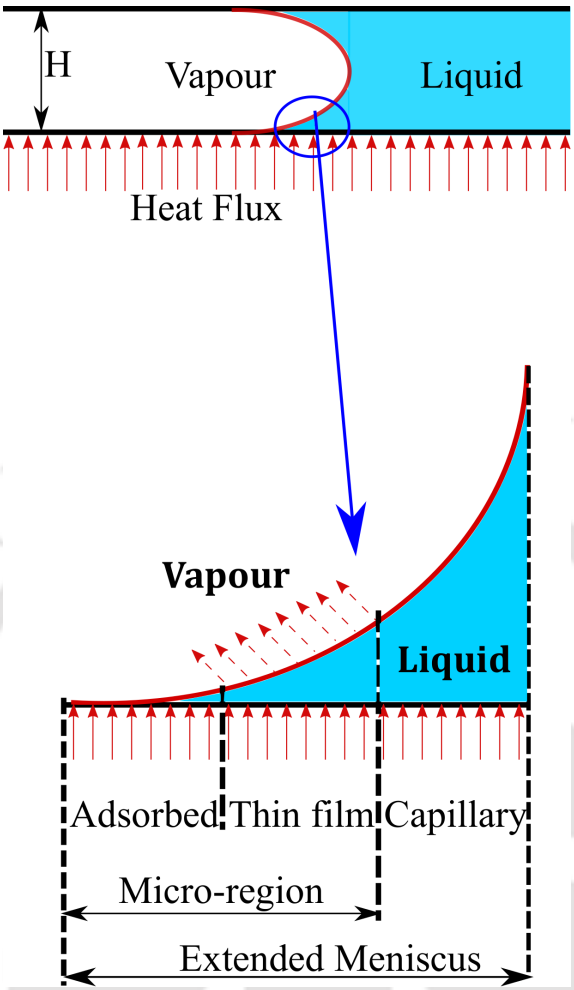

Figure 6.1: Liquid-vapour interface in the device evaporator

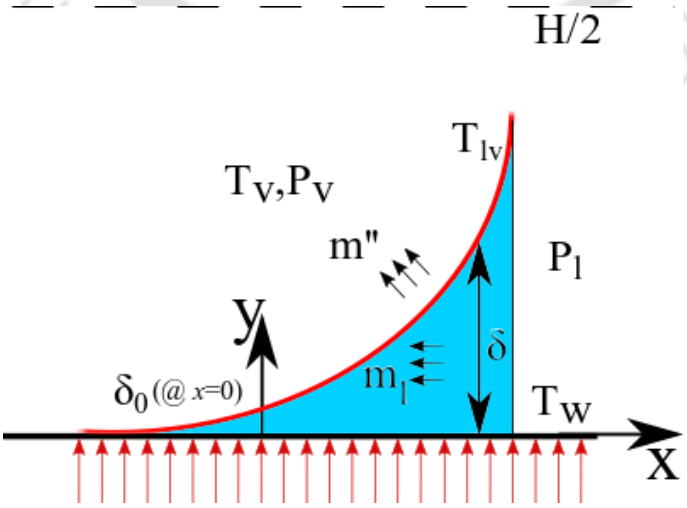

Figure 6.2: Thin-film region

6.1.2 Capillary pressure

$$P_c = \sigma \frac{\frac{d^2\delta}{dx^2}}{\{1+(\frac{d\delta}{dx})^2\}^{3/2}} \tag{6.2}$$

6.1.3 Disjoining pressure

$$P_d = \frac{A}{\delta^3}\frac{(1+3b\delta/2e)}{(1+b\delta/e)^2} \tag{6.3}$$

Equation (6.3) models, both the retarded and non-retarted components of disjoining pressure[156].

6.1.4 Liquid pressure

$$\frac{dP_l}{dx} = -\frac{3\mu_l \dot{m}_l}{\rho_l \delta^2(\delta+3\beta)} \tag{6.4}$$

6.1.5 Liquid mass flow rate

The mass flow rate of liquid is calculated by integrating the following equation:

$$\dot{m}'' = -\frac{d\dot{m}_l}{dx} \tag{6.5}$$

In this study, the Wayner model of mass transfer is used, which is given by:

$$\dot{m}'' = \frac{2\hat{\sigma}}{2-\hat{\sigma}}\left(\frac{\overline{M}}{2\pi\overline{R}}\right)^{1/2}[c_1(T_{lv}-T_v)-c_2(P_v-P_l)] \tag{6.6}$$

Combining equations 6.5 and 6.6 gives the following equation:

$$\frac{d\dot{m}_l}{dx} = -\frac{2\hat{\sigma}}{2-\hat{\sigma}}\left(\frac{\overline{M}}{2\pi\overline{R}}\right)^{1/2}[c_1(T_{lv}-T_v)-c_2(P_v-P_l)] \tag{6.7}$$

Here, c_1 and c_2 are constants given by:

$$c_1 = \left(\frac{P_v\overline{M}\lambda}{\overline{R}T_vT_{lv}^{3/2}}\right), \quad c_2 = \left(\frac{V_lP_v}{\overline{R}T_{lv}^{3/2}}\right)$$

6.1.6 Interface temperature

Two different methodologies are available to calculate T_{lv}:

- **Energy Balance:** Here, the energy balance is considered between the evaporating flux in the interface and the conduction across the thin-film. This leads to the following correlation:

$$\begin{aligned} m''\lambda &= \frac{k_l(T_w-T_{lv})}{\delta} \\ \implies T_{lv} &= T_w - \frac{m''\lambda\delta}{k_l} \end{aligned} \tag{6.8}$$

- **Clausius-Clapeyron Equation:** This methodology consists of linear expansion of the Clausius-Clapeyron equation which gives the following equation [159], [201], [202]:

$$T_{\mathrm{lv}} = T_v \left(1 + \frac{P_v - P_l}{\rho_v \lambda}\right) \tag{6.9}$$

  However, in some studies [151], [161], [203], expansion of the Clausius-Clapeyron equation leads to the following relation:

$$T_{\mathrm{lv}} = T_v \left(1 + \frac{P_v - P_l}{\rho_l \lambda}\right) \tag{6.10}$$

Although both the equations (6.9) and (6.10) have been derived from the same source for the same application (thin-film evaporation on microchannels and stationary plates), both will give different values. Hence to verify, all the three methods will be used to model the interface temperature and its result will be compared with data from the literature, in the subsequent section. Similar comparison was also done by Kou et al.[151] but only between equations (6.8) and (6.10).

6.2 Boundary Conditions

The boundary conditions of thin-film thickness, liquid pressure, evaporating mass flux and interface temperature are discussed below.

6.2.1 Thin-film thickness

Since equation (6.1) is a third-order ordinary differential equation, at least three boundary conditions are required, *i.e.*, δ, $\frac{\mathrm{d}\delta}{\mathrm{d}x}$ and $\frac{\mathrm{d}^2\delta}{\mathrm{d}x^2}$. Different values of the first and second derivatives of δ used in the literature are shown in table 6.1. For a meniscus in a channel, the meniscus radius always approaches half of the height of the channel[150]. This constitutes the far-field condition in this problem.

There exist two methodologies to calculate the film thickness at the onset of thin the thin-film, at $x = 0$ (δ_0), derivations for which can be found in the appendix:

- **Wayner's Mass flux Model:** Since evaporation has not started yet, at $x = 0$, $\dot{m}''$ is taken as zero. Therefore, from equation (6.8), $T_{\mathrm{lv}} = T_w$.

Table 6.1: List showing different values of first and second derivatives of δ at $x = 0$ from literature

References	$\frac{\mathrm{d}\delta}{\mathrm{d}x}$	$\frac{\mathrm{d}^2\delta}{\mathrm{d}x^2}$	Designation
[142]	0	0	BC1
[150],[155], and [151]	1×10^{-11}	Far-field boundary condition	BC2
[134]	1×10^{-11}	1×10^{-19}	BC3
[143],[147], and [160]	Far-field boundary condition	0	BC4

Thus, from equation (1.1) and (6.6):

$$\delta_0 = \left\{ \frac{A\,T_v}{\rho_l\,\lambda\,(T_w - T_v)} \right\}^{1/3} \tag{6.11}$$

In the present study, this method will be called 'Wayner's method' and will be denoted by $(\delta_0)_{\text{way}}$.

- **Clausius-Clapeyron Equation:** Continuing from equation (6.9):

$$\delta_0 = \left\{ \frac{A\,T_v}{\rho_v\,\lambda\,(T_w - T_v)} \right\}^{1/3} \tag{6.12}$$

This will be called 'Clausius-Clapeyron method' and will be denoted by $(\delta_0)_{\text{cc}}$. Equation (6.10) gives the same expression of δ_0 as equation (6.11).

Figure 6.3 compares the values of thin-film thickness, liquid pressure and disjoining pressure at $x = 0$ calculated from the two methods. Working fluid considered are some of the common fluids used in these problems, *i.e.* octane, ammonia, acetone and pentane, at a saturation temperature of 30°C and superheat of 1K. From figure 6.3(a), it is clear that δ_0 calculated from equation (6.11) is very low. This gives negative liquid pressure (figure 6.3(b)) which is not acceptable as researchers have argued that in thin-film region, liquid pressure will always be positive[166], [204]. This can also be confirmed from the experimental data of Hanchak et al.[156].

The 'Clausius–Clapeyron' method, on the other hand, gives a high value of δ_0. This gives a relatively thick film at $x = 0$, which leads to a low value of disjoining pressure (figure 6.3(c)). This also goes against the physics of the problem. Thus, it is clear that both the methods have their limitations, and hence, a new methodology is required to calculate δ_0.

Hence, in this study, two new parameters are defined $(\delta_0)_{\text{min}}$ and $(\delta_0)_{\text{max}}$ which will represent the lower and upper limits of (δ_0) respectively, *i.e.*:

$$(\delta_0)_{\text{min}} < \delta_0 < (\delta_0)_{\text{max}} \tag{6.13}$$

Following are its details:

1. Definition of $(\delta_0)_{\text{min}}$: It is defined as the film thickness where the vapour pressure is precisely equal to disjoining pressure, and hence, rendering liquid pressure zero (figure 6.4). Since liquid pressure is positive in the thin-film region, it implies that $(\delta_0)_{\text{min}} < \delta_0$. Following is its derivation:

$$\begin{aligned} P_v - P_l &= P_d \quad \text{(From equation (1.1))} \\ \implies P_v - P_l &= \frac{A}{\delta_0^3} \end{aligned} \tag{6.14}$$

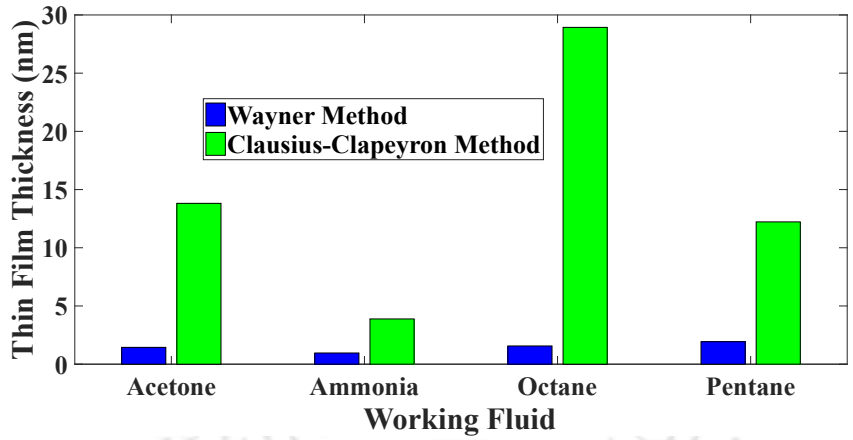

(a)

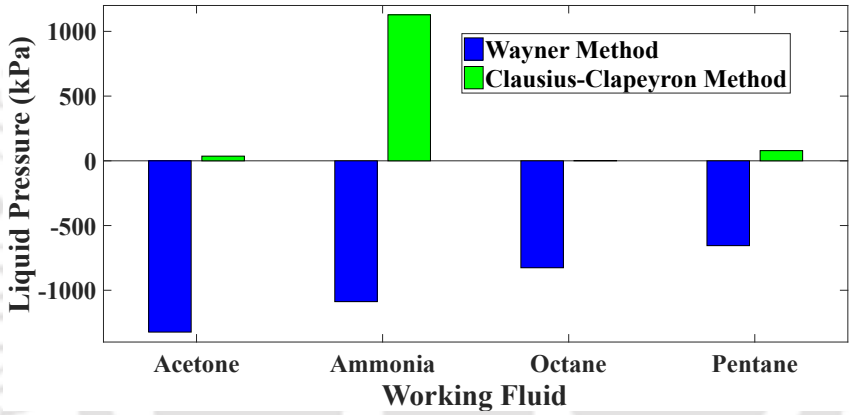

(b)

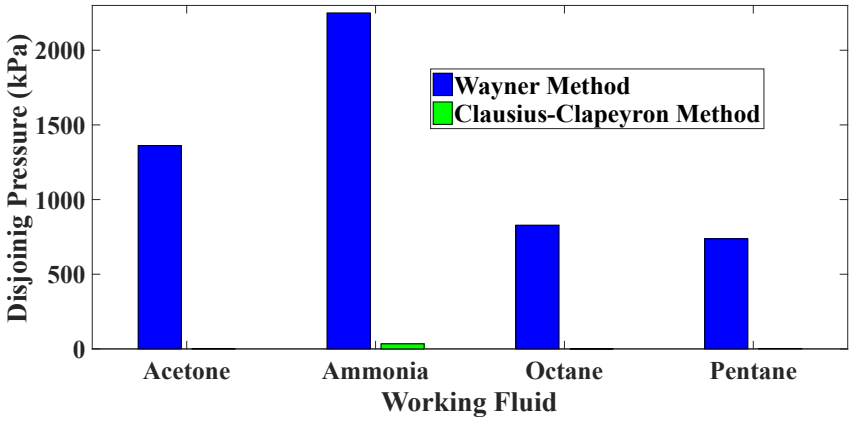

(c)

Figure 6.3: Comparision of : (a) thin-film thickness, (b), Liquid Pressure and (c) Disjoining Pressure, at $x = 0$ calculated from 'Wayner' and 'Clausius-Clapeyron' method for different working fluid at same saturation temperature and superheat

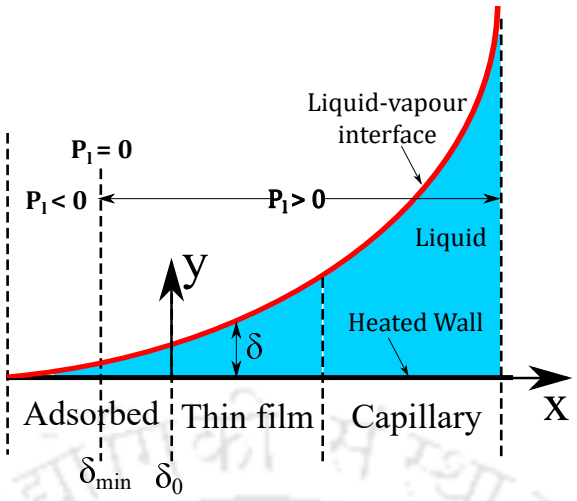

Figure 6.4: Extended maniscus showing variation of liquid pressure

To keep the analysis simple, non-retarded expression of P_d is used. Now, as $\delta_0 \rightarrow (\delta_0)_{min}$, $(P_v - P_l) \rightarrow P_v$. So, equation (6.14) becomes:

$$P_v = \frac{A}{(\delta_0)_{min}^3}$$

$$\implies (\delta_0)_{min} = \left(\frac{A}{P_v}\right)^{1/3} \tag{6.15}$$

Equation (6.15) shows that $(\delta_0)_{\min}$ is independent of superheat and depends only on the properties of the working fluid.

2. Definition of $(\delta_0)_{\max}$: It is assigned the same value as 'Clausius-Clapeyron' method (equation (6.12)):

$$(\delta_0)_{\max} = \left\{\frac{A\,T_v}{\rho_v\,\lambda\,(T_w - T_v)}\right\}^{1/3} \tag{6.16}$$

To prove the theory shown by equation (6.13), experimental δ_0 is taken from the literature and compared with their corresponding $(\delta_0)_{\min}$ and $(\delta_0)_{\max}$. In this study, experimental data of Hanchak et al.[156] is used for validation. They measured the thin-film thickness of n-octane on a heated silicon wafer using a microscope-based reflectometer. They estimated the film profile and using that data calculated δ_0 for five different cases, as shown in table 6.2.

Figure 6.5 compares the value of δ_0 measured in their experiment (denoted as $(\delta_0)_{\text{exp}}$) with $(\delta_0)_{\min}$, $(\delta_0)_{\text{cc}}$ and with $(\delta_0)_{\text{way}}$. As can be seen from the figure, $(\delta_0)_{\text{cc}}$ gives exceptionally high value as compared to $(\delta_0)_{\text{way}}$ for all the five cases. Hence, it is justified to denote it as $(\delta_0)_{\max}$. $(\delta_0)_{\text{exp}}$ is also always found in between $(\delta_0)_{\min}$ and $(\delta_0)_{\max}$. Thus, this proves the theory represented by equation (6.13).

Now, let us refer figure 6.5 again. As can be seen from this figure, $(\delta_0)_{\text{way}}$ provides a closer estimate of δ_0 compared to $(\delta_0)_{\text{cc}}$. The accuracy varies between 80–90% (table 6.3). However, as superheat increases, the value of $(\delta_0)_{\text{way}}$ decreases and even gives a value less than $(\delta_0)_{\min}$ for high superheats, which is unacceptable (figure 6.6(a)). On the other hand, $(\delta_0)_{\text{cc}}$ gives extremely high

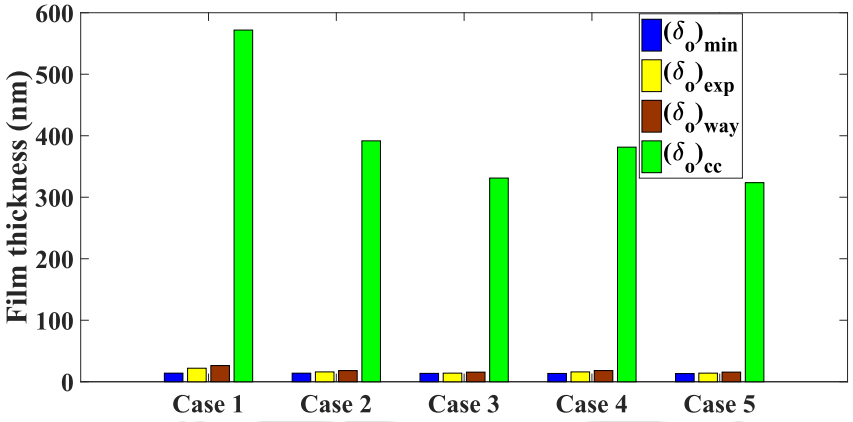

Figure 6.5: Comparison of $(\delta_0)_{way}$ and $(\delta_0)_{cc}$ with $(\delta_0)_{min}$ and δ_0 taken from experiment[156]

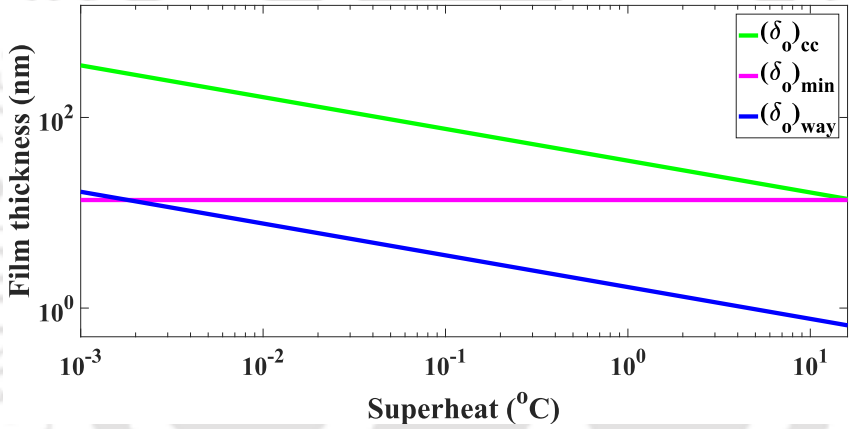

(a)

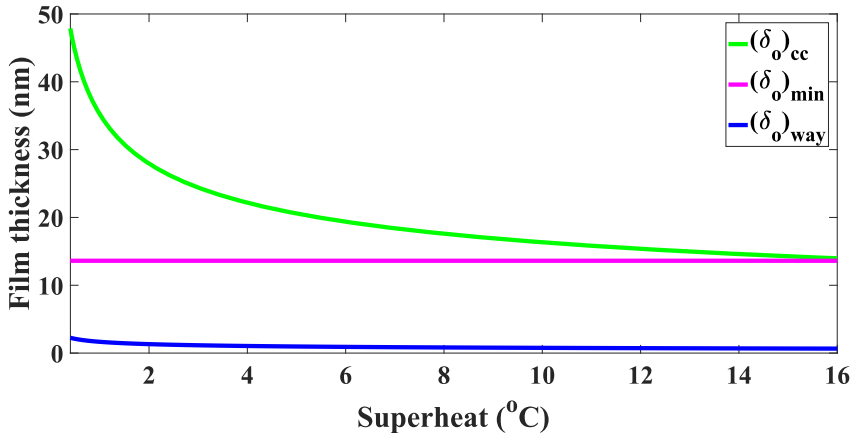

(b)

Figure 6.6: Comparison of $(\delta_0)_{min}$, $(\delta_0)_{way}$ and $(\delta_0)_{cc}$ taking octane at 22.3 °C saturation temperature (a) for a range of superheats and (b) for high superheats

Table 6.2: Experimental data taken from Hanchak et al.[156]

Case	Equilibrium film thickness (nm)	Vapour Temperature (K)	Superheat (K)
1	22	293.9	2.5×10^{-4}
2	16	294.1	7.7×10^{-4}
3	14	295.3	1.2×10^{-3}
4	16	295.7	7.7×10^{-4}
5	14	296.7	1.2×10^{-3}

Table 6.3: Comparision of $(\delta_0)_{\text{exp}}$ and $(\delta_0)_{\text{way}}$ from Hanchak et al.[156]

Case	$(\delta_0)_{\text{exp}}$(nm)	$(\delta_0)_{\text{way}}$(nm)	Accuracy(%)
1	22	26.29	80.5
2	16	18.07	87.06
3	14	15.63	88.36
4	16	18.13	86.69
5	14	15.67	88.07

values (unrealistic) at low superheats, but starts giving acceptable values as the superheat increases, as shown in figure figure 6.6(b).

Thus, from figure 6.6, it can be deduced that the Wayner method gives acceptable values of δ_0 only for extremely low superheat (order 10^{-3} K) and the Clausius-Clapeyron method only for extremely high superheat ($>$ 10 K). Based on these observations, a simple expression for estimating δ_0 for a wide range of superheats (from 10^{-3} K to 20 K) is proposed as follows:

$$\delta_0 = (\delta_0)_{\text{way}}\{f(\Delta T)\} + (\delta_0)_{\text{cc}}\{g(\Delta T)\} \tag{6.17}$$

where f and g are functions of superheat (ΔT) having the following asymptotes:

$$\text{As } \Delta T \to 0, \text{ f} \to 1 \text{ and g} \to 0;$$
$$\text{As } \Delta T \to \infty, \text{ f} \to 0 \text{ and g} \to 1.$$

Furthermore, the functions f and g should have significant values only for $\Delta T < 20$ K and $\Delta T > 10^{-3}$ K, respectively. The upper limit of 20 K is so chosen as Zhao et al. [143] have found no enhancement in heat transfer beyond 20 K superheat in their thin-film evaporation study. The functions f and g have to be defined in such a way that they satisfy the above conditions and the estimated value of δ_0 follows the physics of the problem. The following simple functions are found to meet these criteria:

$$f = \exp\left(-\varsigma \times \frac{\Delta T}{T_v}\right)$$
$$g = 1 - \exp\left(-\varsigma \times \frac{\Delta T}{T_v}\right)$$

Here, ς is a non-dimensional coefficient. The value of ς should be taken in such a way that the calculated δ_0 is always greater than $(\delta_0)_{\text{min}}$. An exponential function is chosen because it is smooth.

Figure 6.7 shows δ_0 calculated from equation 6.17 and compared with $(\delta_0)_{\text{way}}$ and $(\delta_0)_{\text{cc}}$ for octane at two saturation temperatures (22.3 °C and 70 °C), which have been used in the literature. Between these two values of saturation temperature, ς in the range of 500 to 1500 gives satisfactory

results. It can be seen that the proposed method gives a realistic estimate of δ_0 for a wide range of superheats and mimics $(\delta_0)_{\text{way}}$ and $(\delta_0)_{\text{cc}}$ at low and high superheats, respectively.

6.2.2 Liquid Pressure

The liquid pressure at $x = 0$ is calculated from equation (1.1).

$$\begin{aligned} P_v - P_l &= P_d \\ \implies P_l &= P_v - P_d \end{aligned} \tag{6.19}$$

Here P_v is the saturation pressure at the vapour temperature.

6.2.3 Liquid mass flow rate

As there is no evaporation at $x = 0$, the mass flow rate of the liquid is taken as zero.

6.2.4 Interface temperature

The following are the expressions for $(T_{\text{lv}})_{x=0}$ obtained from the three methods (equations 6.8, 6.9 and 6.10) discussed earlier, taking $m'' = 0$ and utilizing equation 1.1.

- Method 1 (based on equation 6.8):

$$(T_{\text{lv}})_{x=0} = T_w$$

- Method 2 (based on equation 6.9):

$$(T_{\text{lv}})_{x=0} = T_v \left(1 + \frac{A}{\rho_v \lambda \delta_0^3}\right)$$

- Method 3 (based on equation 6.10):

$$(T_{\text{lv}})_{x=0} = T_v \left(1 + \frac{A}{\rho_l \lambda \delta_0^3}\right)$$

Figure 6.8 shows the comparison of the interface temperatures at $x = 0$ obtained by these three methods. Methods 1 and 3 give values of $(T_{\text{lv}})_{x=0}$ equal to T_w and T_v (in this case, it is 22.3 °C), respectively. Method 2 gives a value greater than T_w for low superheat but becomes equal to T_w as the superheat increases.

Method 2 goes against the physics of the phenomena involved, as the maximum temperature that can be attained by the working fluid undergoing evaporation is the wall temperature. Method 3 also goes against the result of Stephan and Busse[205] as they have proved that the interface temperature cannot be equal to saturation temperature because it overpredicts the heat transfer coefficient.

Thus, from the above discussion, it can be said that only the energy balance method (Method 1) gives an acceptable value of $(T_{\text{lv}})_{x=0}$ for all superheat.

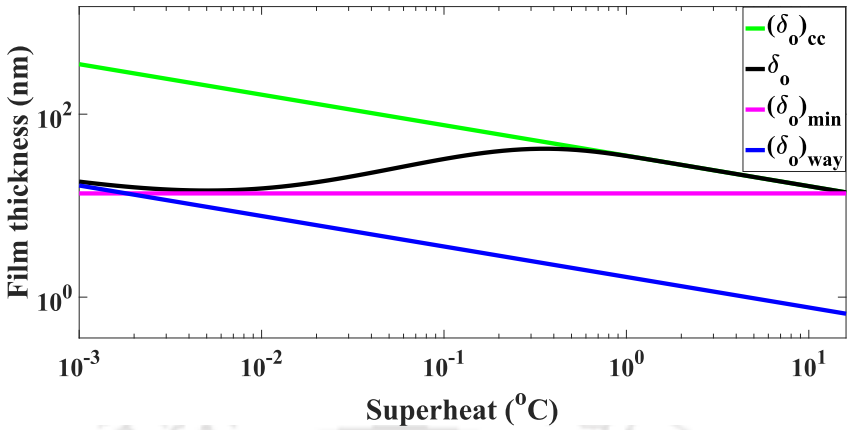

(a)

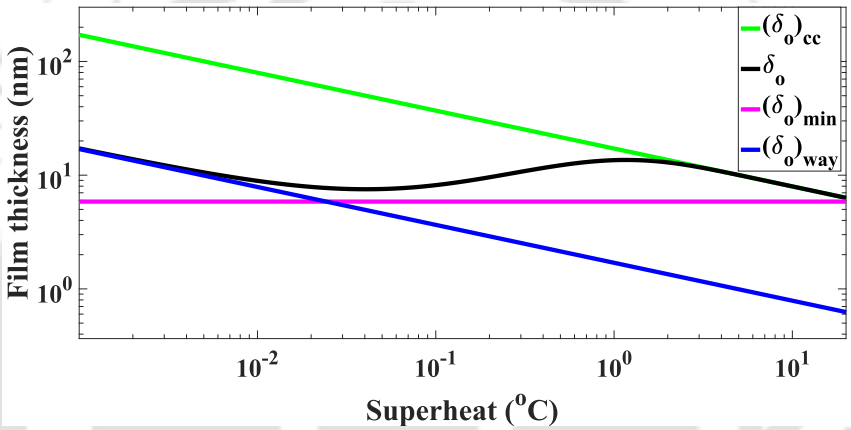

(b)

Figure 6.7: Comparison of δ_0 from equation (6.17) with $(\delta_0)_{\text{way}}$ and $(\delta_0)_{\text{cc}}$ for (a) octane at 22.3 °C saturation temperature and (b) octane at 70 °C saturation temperature

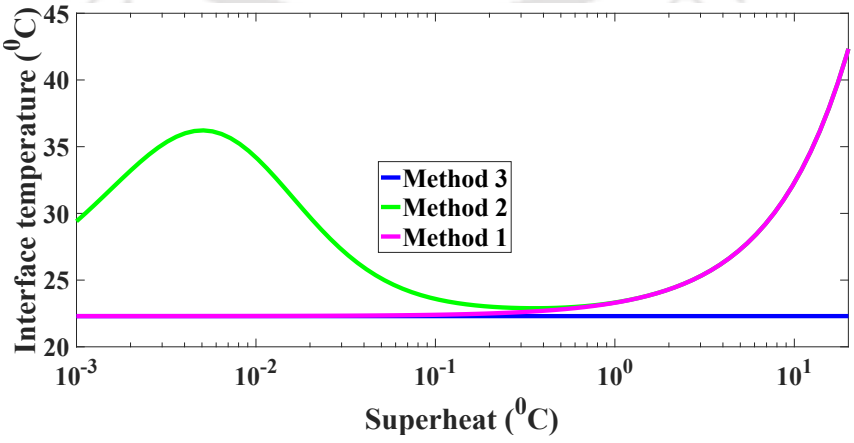

Figure 6.8: Interface temperature at $x = 0$ for a range of superheat using different methods available in the literature

CHAPTER 7

SIMULATION RESULTS

THE film thickness profile can be obtained by simultaneously solving equations for film thickness (equation 6.1), liquid pressure (equation 6.4), mass flow rate (equation 6.7) and interface temperature, with appropriate boundary conditions, for which the fourth-order Runge-Kutta method has been used in the present work. For the interface temperature, all three equations (6.8, 6.9, 6.10) are tested, since it was not clear which method would give correct results. Figure 7.1 shows the flowchart of the algorithm used.

7.1 Solution methodology

The thin-film evaporation is a two-point boundary condition problem. Hence, a shooting technique is used to solve it. An in-house Matlab code is used to implement this algorithm. Following are the steps involved:

1. The properties of the working fluid are inserted as an input and the governing equations(6.1-6.10) are set.
2. δ_0 is calculated using equation (6.17).
3. Boundary conditions of capillary pressure, disjoining pressure, liquid pressure, mass flow rate and interface temperature are set as explained in section 6.2.
4. For the values of $\frac{d\delta}{dx}$ and $\frac{d^2\delta}{dx^2}$, BC4 scheme is used (refer table 6.1) as it was observed that the thin film thickness is extremely sensitive to its first derivative, which was also reported by Jung and Boo[206]. Hence, a suitable assumption is made on the initial value of $\frac{d\delta}{dx}$ and $\frac{d^2\delta}{dx^2}$ is set as zero.
5. The equations are solved using Runge-Kutta method. In the Matlab code, ode45 function is used.
6. The curvature is calculated using equation (6.2).

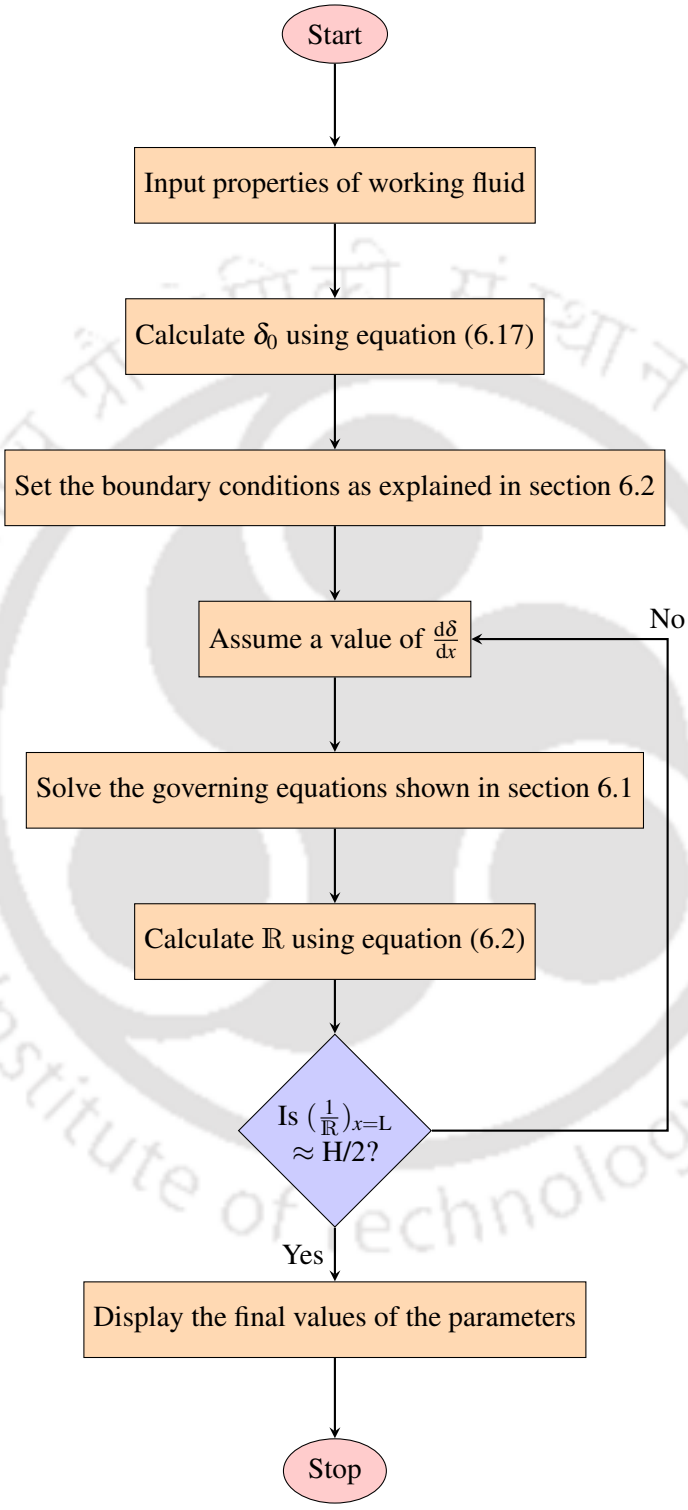

Figure 7.1: Flowchart showing the solution methodology

7. Steps 4, 5 and 6 are repeated until the far-field boundary condition is satisfied, *i.e.* the meniscus radius approaches the half of the channel height.

8. Length of the thin film is calculated by taking the reading of the film where the disjoining pressure is 1/5000th of its value at the start of thin film *i.e.* at $x = 0$[150].

9. The simulation is stopped and the results are displayed.

7.2 Model validation

The equations are validated with results from the literature, for a case of significantly high superheat [150] and a case of very low superheat [156]. Figure 7.2 shows the comparison. As can be seen from the figure, the film thickness profiles obtained with the set of equations: (6.1, 6.4, 6.7 and 6.8) agrees well with the results in the literature [150], [156], except for a slight deviation, possibly due to the inclusion of the slip factor (β) in the present model. Thus, it is inferred that method 1 equation (6.8) models the interface temperature correctly.

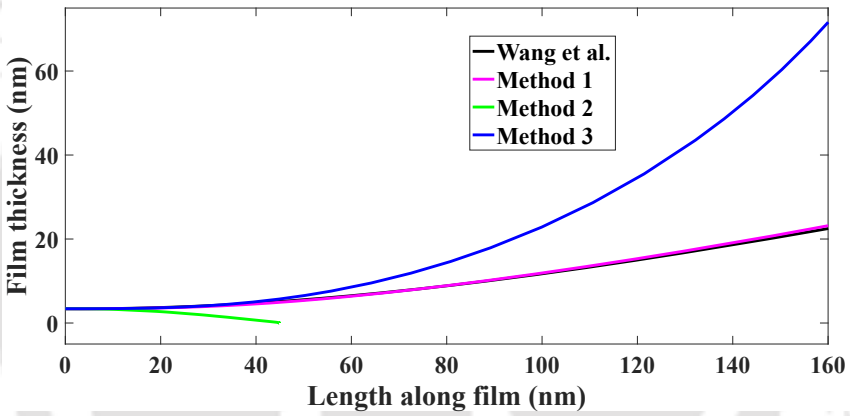

(a)

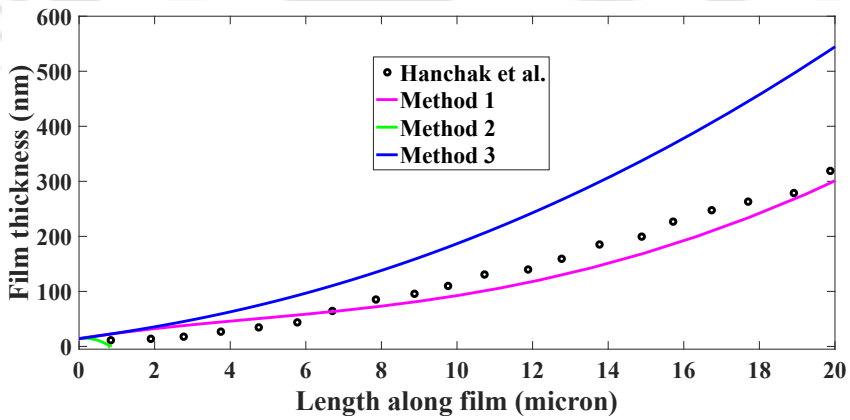

(b)

Figure 7.2: Comparison of film thickness profile generated from the present model with (a) Wang et al. [150] (1 K superheat) and (b) Hanchak et al. [156] (case 3)

It can also be observed that the line corresponding to method 2 abruptly ends. This is because for method 2, the values of its boundary conditions are greater than the wall temperature (figure 6.8). This goes against the physics of the phenomena involved, as the maximum temperature that

can be attained by a working fluid undergoing evaporation is the wall temperature. Hence, while solving the governing equations of method 2, the algorithm crashed and had to be truncated. No such problem occurred while solving the other two methods.

7.3 Heat transfer analysis

As explained by Plawsky et al.[207], there are three thermal resistances connected in series in a meniscus. They are:

1. Wall resistance, generally very low.
2. Conduction resistance of the liquid ($1/h_{\mathrm{l}}$).
3. Interfacial resistance between the vapour and the liquid film ($1/h_{\mathrm{lv}}$)

Thus, the total (or overall) heat transfer coefficient is given by:

$$\frac{1}{h_{\mathrm{overall}}} = \frac{1}{h_{\mathrm{lv}}} + \frac{1}{h_{\mathrm{l}}}$$

The expressions for $1/h_{\mathrm{lv}}$ and $1/h_{\mathrm{l}}$, taken respectively from Wang et al.[150] and Biswal et al.[155], are given below:

$$h_{\mathrm{lv}}(x) = \lambda \left\{ c_1 - c_2 \left(\frac{P_d + P_c}{T_{\mathrm{lv}} - T_v} \right) \right\} \tag{7.1a}$$

$$h_{\mathrm{l}}(x) = \frac{k_l}{\delta} \tag{7.1b}$$

Figure 7.3 shows the variation of heat flux along the length of the film. As is clear from the figure, the heat flux decreases in the thin-film region and continues to decrease in the capillary region. This confirms the theory of Maroo and Chung[11]. They suggested that the heat flux attains its highest value at the interline region between the adsorbed region and the thin-film region. After that, it decreases monotonically throughout the thin-film and intrinsic meniscus. This trend can also be confirmed from the experimental data of Nazari et al.[138].

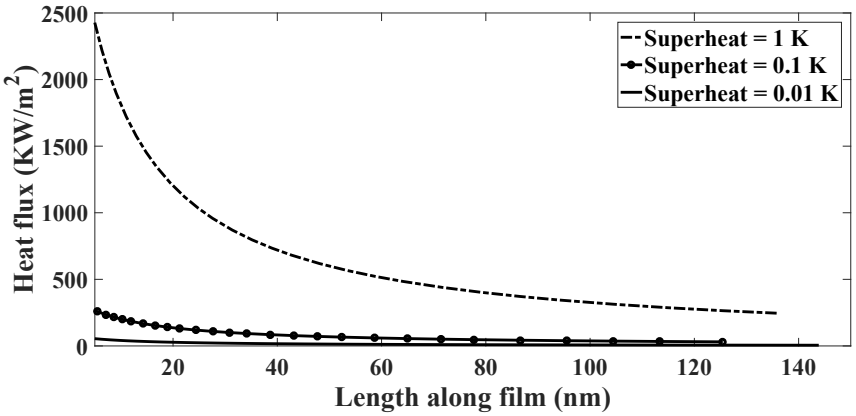

Figure 7.3: Effect of superheat on the heat flux

7.4 Parametric simulations

After validation, the model is used to study the effect of superheat on different parameters. For this, the conditions used in Jasvanth et al.[182] are simulated. They had done experimental as well as mathematical simulation of evaporation from a capillary slot under constant heat flux. Working fluid used is pentane at 35.678°C saturation temperature. Using equation (6.17), initial conditions are calculated. The value of ς is taken as 80. Figure 7.4 clearly shows that δ_0 will not give negative liquid pressure at the onset of thin-film and low disjoining pressure.

Figures 7.5–7.8 show the variation of different parameters after solving the governing equations with the relevant boundary conditions using solution methodology detailed in figure 7.1. Their trend are compared at superheat ranging from 2 to 12 K using δ_0 values shown in table 7.1. Following are the parameters studied:

- Thin-film thickness: Figure 7.5 shows the thin-film profiles for different superheats. From the figure, it is clear that film thickness increases as superheat increases towards the capillary region. With the increase in superheat, the evaporation also increases. This leads to more liquid pumping into the thin-film region leading to an increase in the apparent contact angle and as a consequence, the film thickness.

- Disjoining pressure: Figure 7.6 clearly shows that the disjoining pressure decreases as capillary region approaches (as expected). However, contrary to the results of Yan et al.[159], here, the disjoining pressure at 2K is higher than that of 12K. This is because equation (6.17) gives a lower value of δ_0 at 2K superheat as compared to 12K superheat (figure 7.4). This shows that the present model is not perfect and needs further improvement.

- Capillary pressure: As the capillary region is approached, the film thickness increases. This leads to a high surface tension force, as can be seen in figure 7.7.

- Average velocity: It is calculated from the following expression:

$$\bar{u} = \frac{\dot{m}}{\rho_l \delta}$$

  As can be seen from figure 7.8, the average velocity increases up to a certain limit and then decreases as the capillary region approaches. Also, the fluid has a higher velocity at higher superheat, which can be attributed to a high evaporation rate.

Table 7.1: Values of δ_0 computed at different superheats

Superheat (°C)	**Film thickness (nm)**
2	4.67
4	5.15
6	5.26
8	5.19
10	5.04
12	4.88

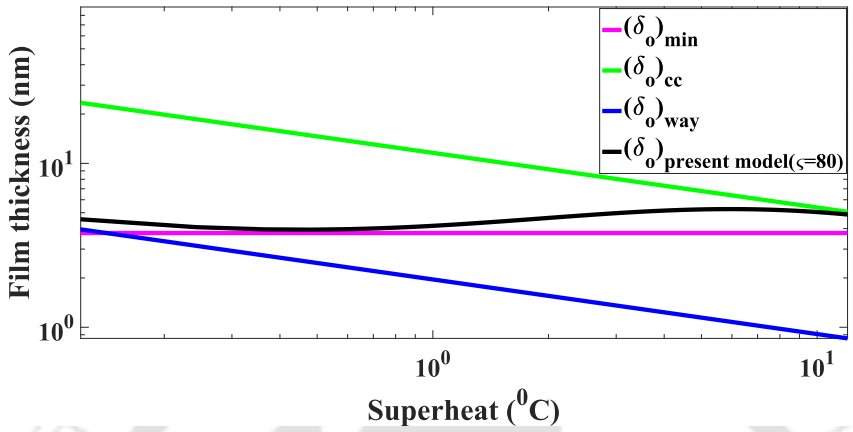

Figure 7.4: Calculation of δ_0 for a range of superheat for conditions depicted in Jasvanth et al.[182]

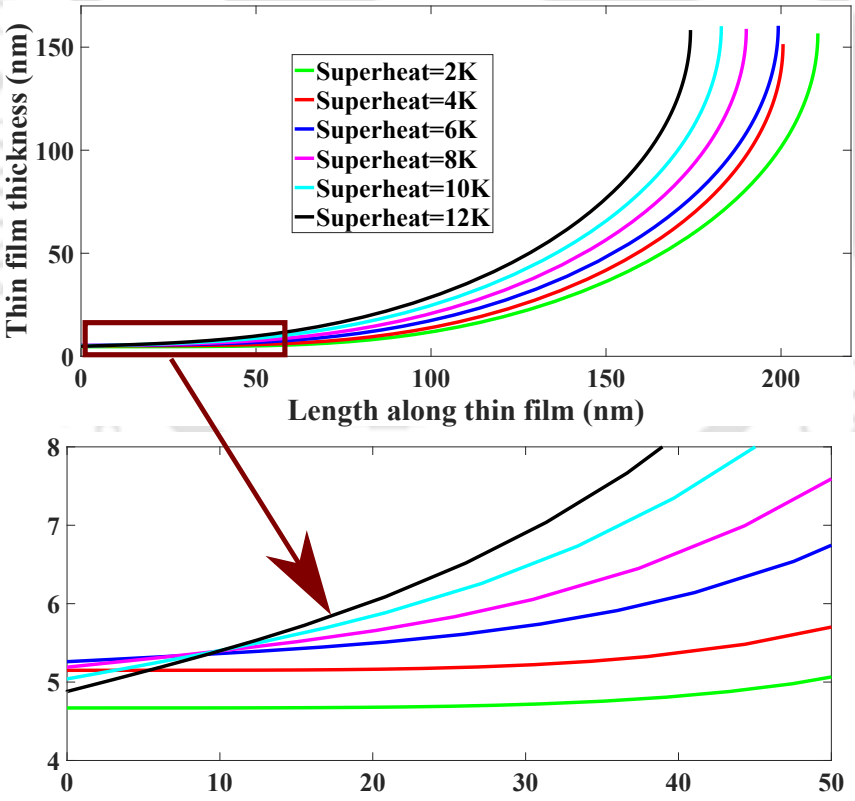

Figure 7.5: Variation of thin-film thickness with superheat

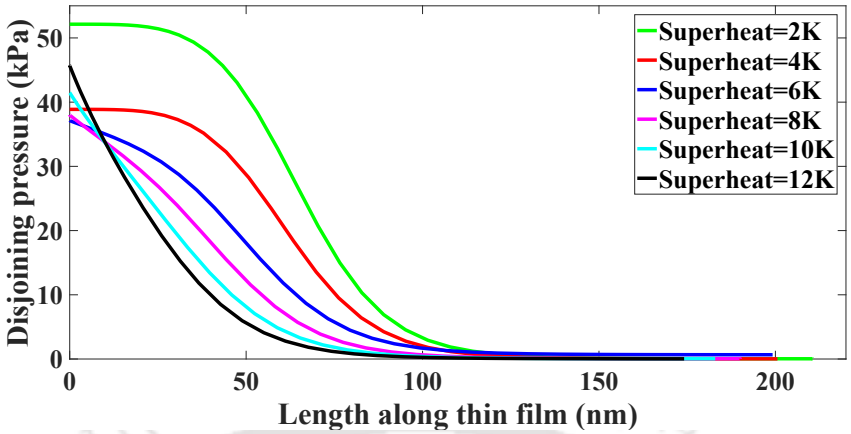

Figure 7.6: Variation of disjoining pressure with superheat

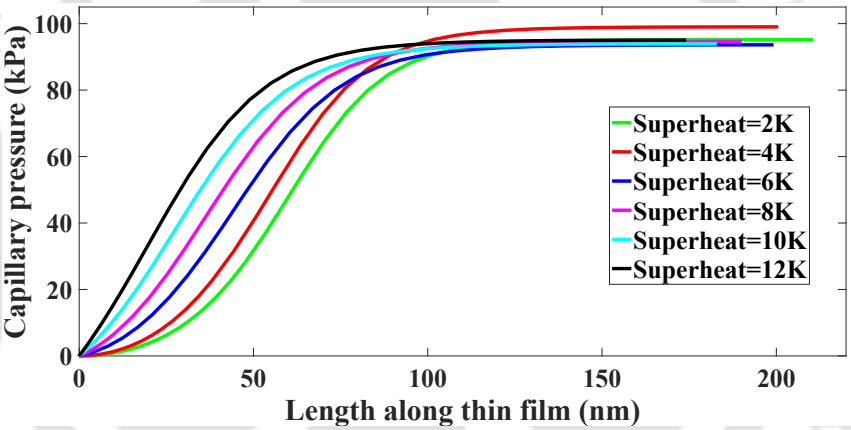

Figure 7.7: Variation of capillary pressure with superheat

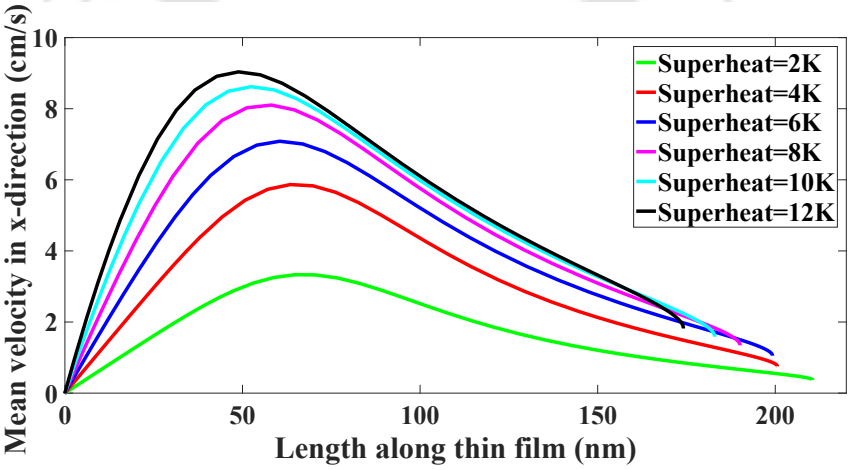

Figure 7.8: Variation of average flow velocity with superheat

CHAPTER 8

NEW FIGURE OF MERIT

In chapter 6, a new parameter $(\delta_0)_{min}$ (equation (6.15)) is introduced. It is defined as the film thickness where liquid pressure is exactly zero, *i.e.* the vapour pressure is exactly equal to the disjoining pressure (figure 6.4). In this chapter, a new figure of merit is developed using this parameter. This is applicable for any devices using thin-film evaporation. Before discussing this parameter, different figures of merit proposed for heat pipes are discussed in the following section.

8.1 Figures of merit for two-phase capillary devices

In section 2.1.2, three figures of merit were discussed (equation 2.1). Following are the different phenomenon they qualitatively represent:

1. **Liquid transport factor (FOM_{LTF}):** Symbolises the capillary limit of the heat pipe, shown by equation (2.1(a)). Also known as '0-g figure of merit' because its expression does not take into account the body force and vapour pressure drop factor.

2. **Body force factor ($FOM_{g\text{-}field}$):** To take into account the body force, equation (2.1(b)) is proposed. Also called the capillary pump factor, this parameter can be used to estimate the performance of the working fluid in an anti-gravitational regime and device orientation.

3. **Nucleation tolerance factor ((FOM_{NTF}):** Shown by equation (2.1(c)), it can be used to estimate the dry-out limit of the device.

These parameters were some of the earliest known figures of merit used for working fluid selection in heat pipes. However, a heat pipe is governed by several complex phenomena and these parameters were not able to accommodate all of them. Hence, researchers proposed various other expressions which can be used as a figure of merit. They are grouped based on the different phenomenon they model, as follows:

8.1.1 Based on heat transport modelling

The following parameters are used to gauge the heat pipe performance by estimating the overall heat transport capacity of the device:

1. For heat sinks, Wayner[27], [28], [208] demonstrated a methodology to approximately determine its performance on constant heat flux mode. He introduced a dimensionless parameter from which the figure of merit can be derived, known as the interline heat flow parameter (equation (8.1)):

$$\mathrm{FoM_{IL}} = \frac{\rho_l A \lambda}{\mu_l} \tag{8.1}$$

   Greater the value of this parameter, higher will be the theoretical heat transfer of the device.

2. Chernyseva and Maydanik[209] put forward the following criterion:

$$\mathrm{K_{Pe}} = \frac{C_P}{\lambda} \tag{8.2}$$

   They derived its expression from the Peclet number. They stated that $\mathrm{K_{Pe}}$ signifies the working fluid cooling effect and consequently, the evaporator temperature.

Figures 8.1 and 8.2 show their variation for ammonia, acetone, octane and pentane.
As can be seen from figure 8.2, $\mathrm{K_{Pe}}$ is very sensitive to the critical state of the working fluid. Because of this, it is advisable to compare the trend of heat pipe figure of merit at that range of temperature, where the critical state does not affect its value. For the set of working fluids considered in this study, this range is between -50 to 100°C. Now, comparing the trend of these two parameters, it can be seen that there is a discrepancy. For $\mathrm{FoM_{IL}}$, ammonia has the highest and pentane has the lowest value, and hence their performance will also vary accordingly. On the other hand, figure 8.2 clearly shows that pentane has the highest value of $\mathrm{K_{Pe}}$, and consequently should have the highest cooling effect and the lowest evaporator temperature. This was also observed experimentally by Anand et al.[106], (fluids compared were pentane, acetone, methanol and ethanol).

This discrepancy can be attributed to the fact that parameters $\mathrm{FoM_{IL}}$ represent wick heat transfer at microscale level (based on thin-film evaporation), while $\mathrm{K_{Pe}}$ represent macroscale heat transfer of the device.

8.1.2 Based on pressure drop in transport channels

In loop heat pipes, vapour pressure drop in the transport channels is the most dominant pressure drop term[185], [186]. However, the parameter $\mathrm{FoM_{LTF}}$ qualitatively represents the capillary limit of the device, but does not takes into account the pressure drop at the transport channels.

Hence, researchers proposed the following parameters which addresses the pressure drop issue and therefore, can be used at low heat loads where the capillary limit is of no consequence.

1. Maydanik et al.[210] put forward a criterion comprising of fluid thermophysical properties. Smaller the value of this criterion (equation (8.3a)), lower is the pressure loss in the vapour line. Later, in another study[49], they suggested the criterion shown in equation (8.3b). Higher the value of this criteria, higher is the performance of the LHP system.

$$(\mathrm{K_v})_{\mathrm{I}} = \frac{\mu_v}{\lambda \rho_v} \frac{dT}{dP} \tag{8.3a}$$

$$(\mathrm{K_v})_{\mathrm{II}} = \frac{\sigma}{\mu_v} \frac{dP}{dT} \tag{8.3b}$$

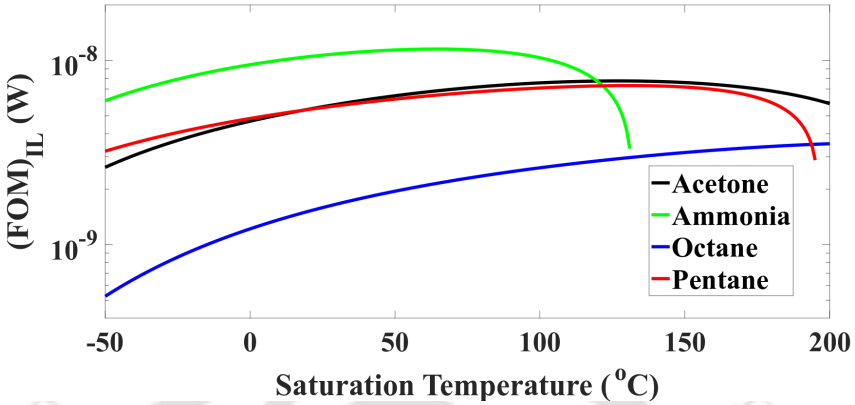

Figure 8.1: Variation of interline heat flow parameter

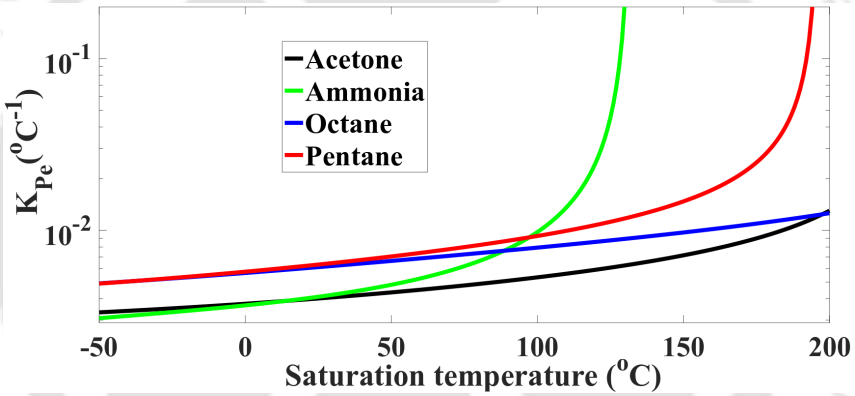

(a)

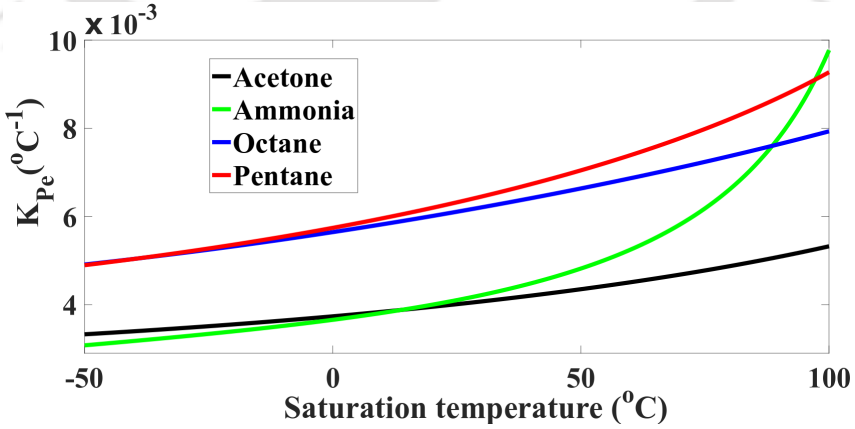

(b)

Figure 8.2: Variation of K_{Pe} with saturation temperature upto (a) 200°C and (b) 100°C

2. Joung et al.[211] proposed an alternate figure of merit for loop heat pipes. This correlation (equation (8.4)) can be used to predict its steady state-performance. It also accounted for the laminar/turbulent vapour flow in the transport channels.

$$\mathrm{FoM_{joung\text{-}lam}} = \frac{\lambda^2 \rho_v^2}{\mu_v} \tag{8.4a}$$

$$\mathrm{FoM_{joung\text{-}turb}} = \left(\frac{\lambda^{11} \rho_v^8}{\mu_v}\right)^{1/7} \tag{8.4b}$$

3. Yadavalli et al.[212] developed a figure of merit (equation (8.5)) for thin heat pipes operating at low heat loads (based on the vapour pressure drop and not affected by the capillary limit).

$$\mathrm{FoM_{yadavalli}} = \frac{P_v \rho_v \lambda^2}{\mu_v R\, T_v{}^2} \tag{8.5}$$

4. Patankar et al.[213] developed a new figure of merit for for flat heat pipes (or ultra-thin vapour chambers). Their figure of merit is based on not only fluid properties, but also its geometric properties. Their methodology works under the assumption that vapour core resistance is the primary resistance in vapour chambers. Here the objective is to maximize the thermal performance instead of heat transport capability. They defined a parameter 'Vapour core effective conductance' (equation (8.6)).

$$k_{vc} = \frac{Q}{\Delta T_{sat}} \tag{8.6}$$

Following are the correlation of the parameters:

$$k_{vc} = a_2\, \mathrm{FoM_{yadavalli}} \left\{ t - a_1 \sqrt{\frac{Q}{\mathrm{FoM_{LTF}}}} \right\}^3$$

$$a_1 = 2\sqrt{\frac{n\, M\, FoS}{4\pi\chi}} \left\{ \ln\left(\frac{r_{vc}}{r_{evap}}\right) + \frac{5}{8} \right\}$$

$$a_2 = \frac{\pi}{6 \ln\left(\frac{r_{vc}}{r_{evap}}\right)}$$

$$\chi = \frac{\phi^3}{\iota(1-\phi)^2}$$

Here ΔT_{sat} is the change in the saturation temperature in the vapour core due to pressure drop.

From figures 8.3, 8.4 and 8.5, it can be observed that ammonia has the lowest and octane has the highest vapour pressure drop in heat pipe systems. Low vapour pressure drop signifies that the heat pipe system will operate at low operating temperature. Experimental data from the literature[106], [211], [214], [215] also show matching trend with that set by these parameters.

Patankar et al.[213] applied $\mathrm{FoM_{yadavalli}}$ and $\mathrm{FoM_{LTF}}$ to develop k_{vc} (equation (8.6)). Figure 8.6 shows its trend for their device, at different power. At low power (Q = 0.25 W), pentane has the

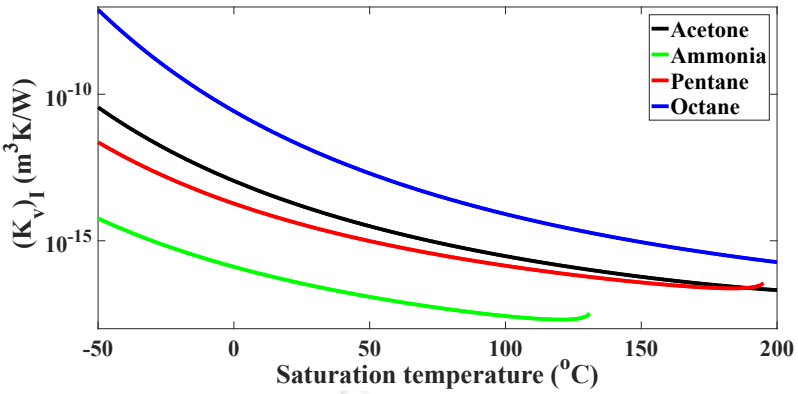

(a) Proposed by Maydanik et al.[210]

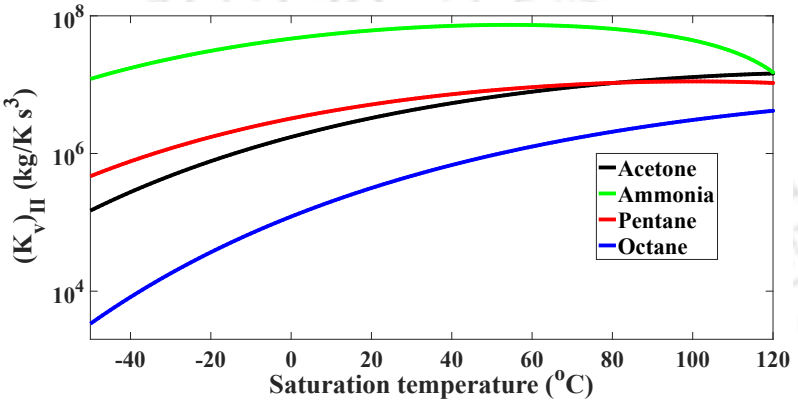

(b) Proposed by Maydanik et al.[49]

Figure 8.3: Variation of K_v criterion

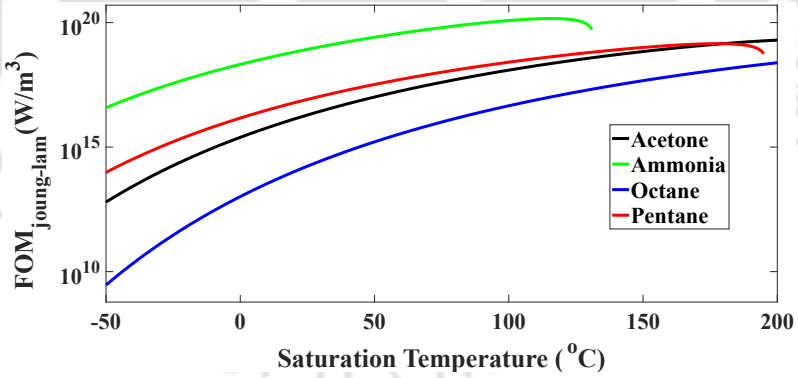

(a)

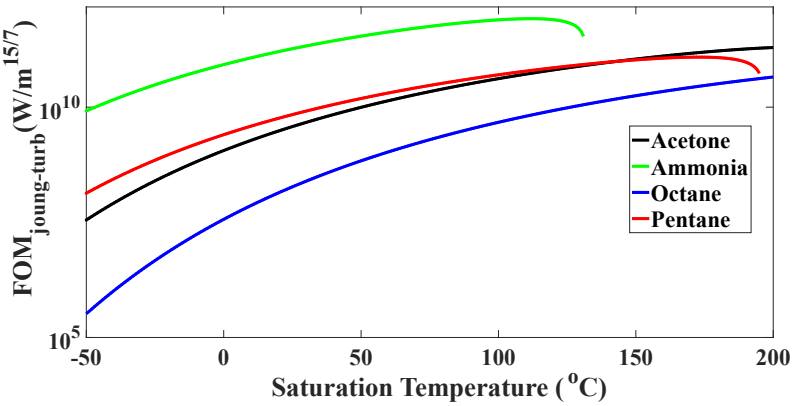

(b)

Figure 8.4: Variation of (a) $(FoM_{lam})_{joung}$ and (b) $(FoM_{turb})_{joung}$ proposed by Joung et al.[211]

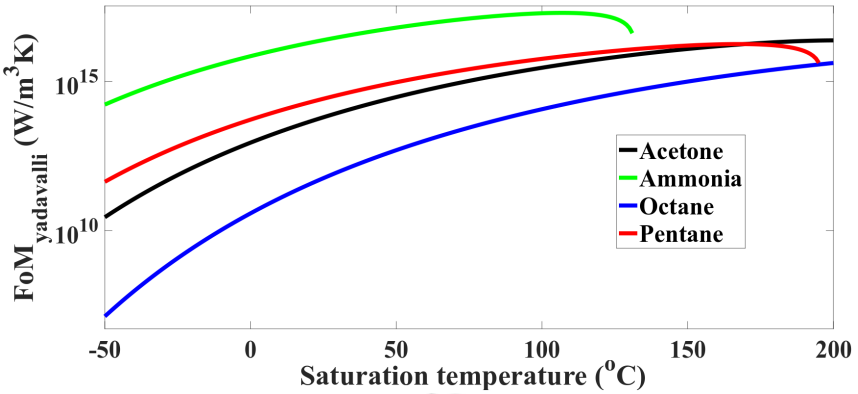

Figure 8.5: Variation of $FoM_{yadavalli}$ with saturation temperature (equation (8.5))

highest value, second only to ammonia and thus its performance can be rated the best (figure 8.6(a)). However, as can be seen from figure 8.6(b), only a slight increase in power leads to performance degradation of pentane (because of low k_{vc}). The authors reasoned that at low power, k_{vc} is affected by $FoM_{yadavalli}$ and at high power, it is affected by FoM_{LTF}. Since pentane has the lowest FoM_{LTF} among all the working fluids (figure 2.3(a)), it will have a low k_{vc} at intermediate to high power. At higher power, most of the working fluids disappear, only ammonia remains. This implies that at those power, only ammonia is feasible. Ammonia gives the best performance throughout the given range of power.

Generally, for low to medium heat load applications, water, ammonia, acetone or methanol is used. Neon/nitrogen is used for cryogenic applications and at extremely high temperature, liquid metals such as sodium, potassium and silver are used[13]. In their review, Jouhara et al.[216] put forward a list of working fluids, and their corresponding operating range and also material compatibility for heat pipe applications.

8.2 Derivation of the new figure of merit

Using $(\delta_0)_{min}$, the theoretical limit of the heat transfer coefficient of the device can be estimated (equation (8.7)). The values of Dispersion constant are shown in table 8.1.

$$(h_l)_{max} = \frac{k_l}{(\delta_0)_{min}} = k_l \left(\frac{P_v}{A}\right)^{1/3} \tag{8.7}$$

The parameters $(\delta_0)_{min}$ and $(h_l)_{max}$ are independent of superheat and only depends on the properties of the working fluid.

As can be seen from figure 8.7, $(\delta_0)_{min}$ shows a decreasing trend with an increase in saturation temperature and approaches a constant value close to zero, at high temperature (>100°C). This

Table 8.1: Values of dispersion constant used (source: Jasvanth et al.[217])

Working fluid	Dispersion constant (J)
Acetone	4.1×10^{-21}
Ammonia	2×10^{-21}
Octane	3.18×10^{-21}
Pentane	5.31×10^{-21}

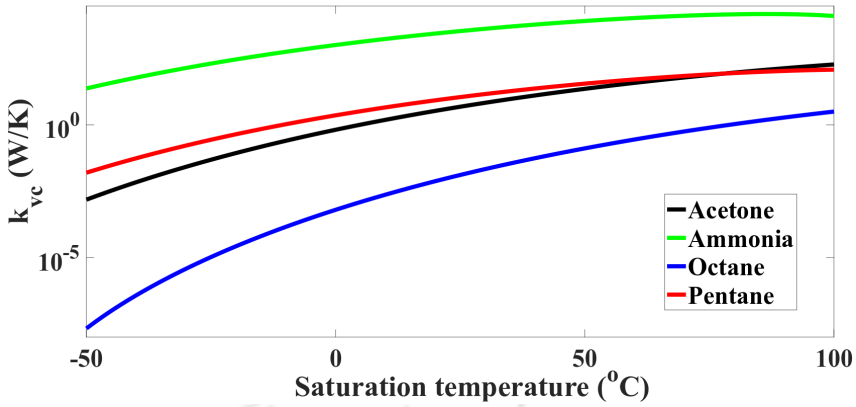

(a) Q = 0.25 W

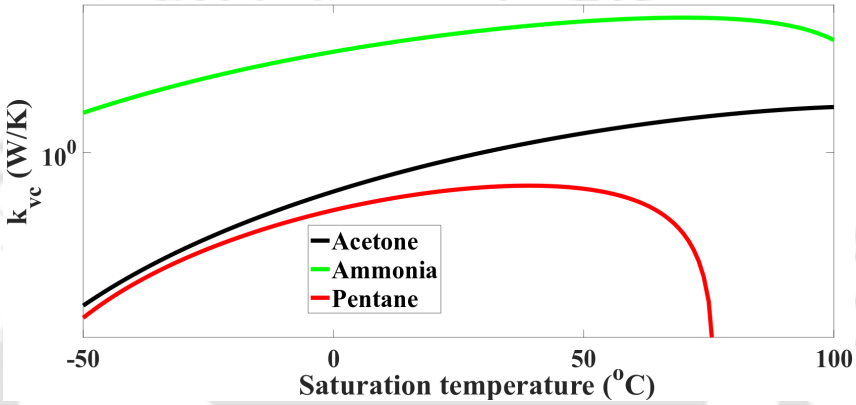

(b) Q = 1 W

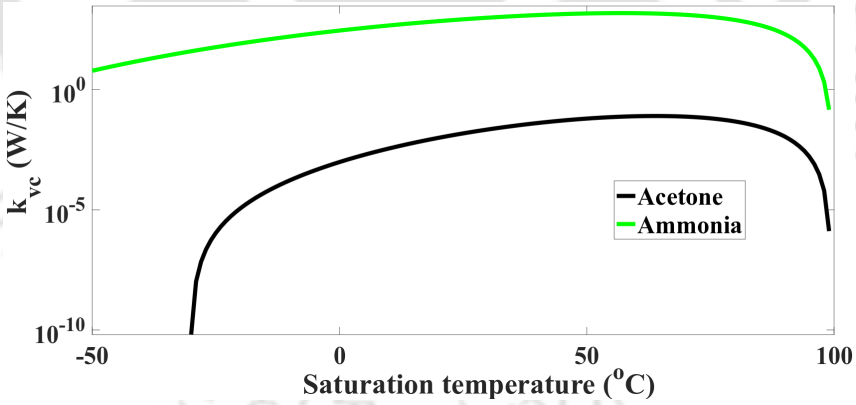

(c) Q = 2 W

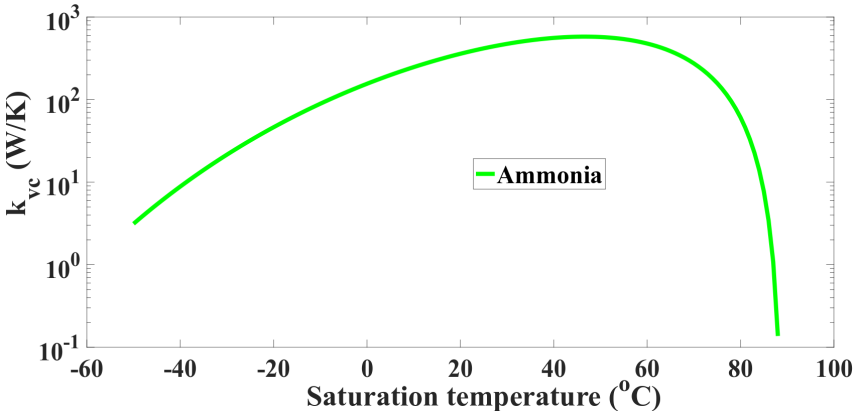

(d) Q = 3 W

Figure 8.6: Variation of k_{vc} (vapour core effective conductance) at various power (calculated using equation (8.6))

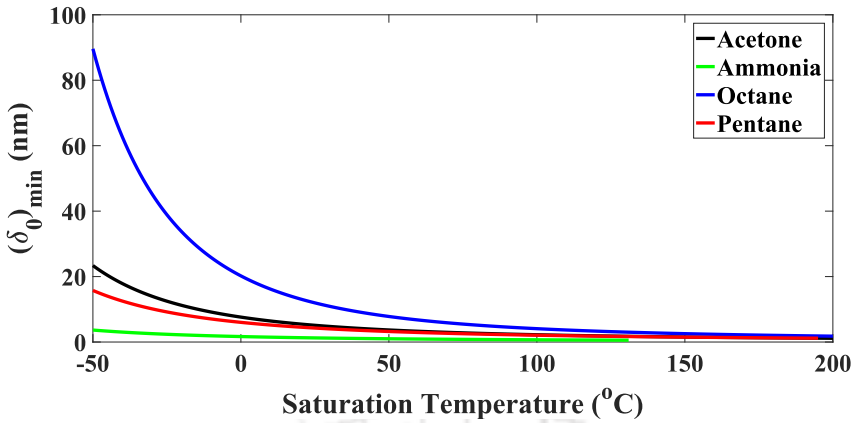

Figure 8.7: Variation of $(\delta_0)_{min}$ calculated from equation (6.15) with saturation temperature for different working fluids

is because of the increase in saturation pressure with temperature. Another observation is that ammonia has the lowest and octane has the highest value of $(\delta_0)_{min}$. This means that measuring the thin-film thickness profile will be comparatively straightforward in the case of octane than ammonia for the same saturation temperature and superheat.

Figures 8.8(a) and (b), shows the variation of the maximum heat transfer coefficient and the overall heat transfer coefficient with the saturation temperature (calculated using equation (8.8)) respectively. Both the graphs show similar trend *i.e.* ammonia and octane at the top and bottom respectively, and acetone and pentane in between but very close to each other. This is because a lower film thickness gives higher heat transfer[218]. This also shows that the parameter $(h_l)_{max}$ behaves similarly to the conventional $h_{overall}$ and can be used as a design tool to compare the performance of different working fluids for these devices.

$$\frac{1}{h_{overall}} = \frac{1}{(h_l)_{max}} + \frac{1}{h_{lv}} \tag{8.8}$$

Where:

$$h_{lv} = \frac{2\hat{\sigma}}{2-\hat{\sigma}} \frac{\rho_v \lambda^2}{\sqrt{2\pi R T_v} T_v} \quad \text{(Taken from Stephan and Busse[205])}$$

8.3 Validation

The trend of $(h_l)_{max}$ (shown in figure 8.8(a)) for four different working fluids over a wide range of saturation temperature is compared with the conventional figures of merit and data from the literature.

1. Interline heat flow parameter ($FOM_{interline}$): It is given by equation (8.1). As can be seen from figure 8.1, it shows a similar trend as $(h_l)_{max}$.

2. Theoretical limit of heat flux: It is derived from the kinetic theory of evaporation and represents the maximum attainable heat flux. Following is its correlation[219], derivation of which is given in the appendix:

$$(q_{max})_{kin} = \rho_v \lambda \sqrt{\frac{RT}{2\pi}} \tag{8.9}$$

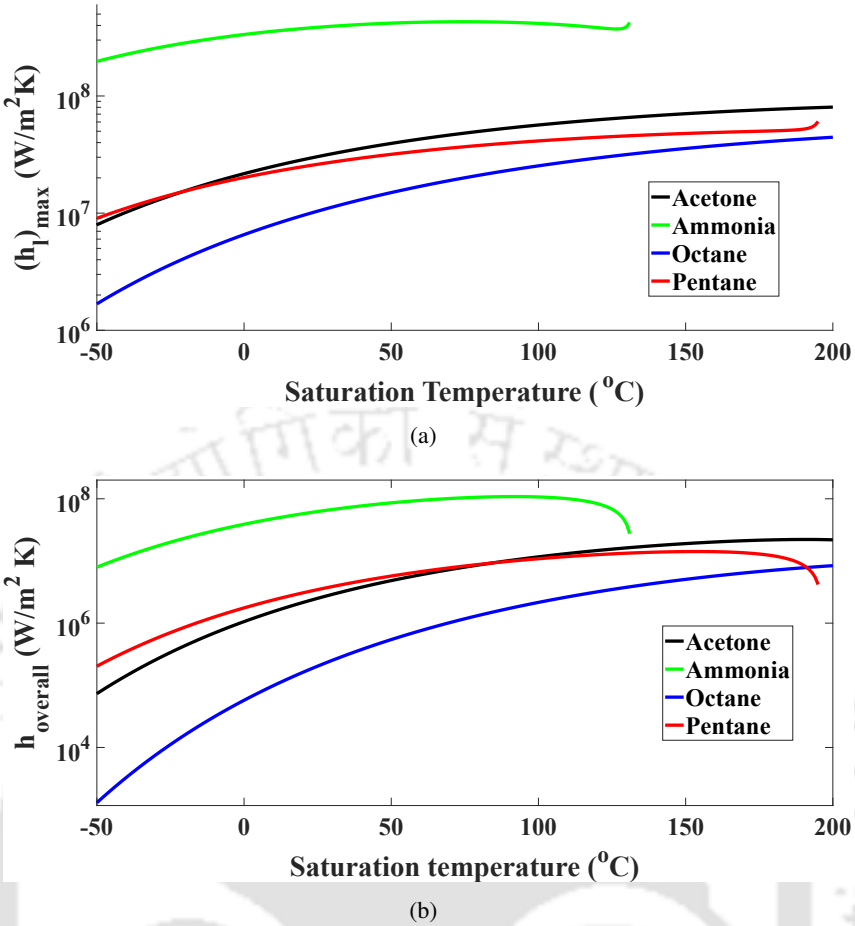

Figure 8.8: Variation of (a) $(h_l)_{max}$ calculated from equation (8.7) and (b) overall heat transfer coefficient calculated from equation (8.8) with saturation temperature for different working fluids

The trends in the two figures 8.8(a) and 8.9 matches with each other.

3. Liquid transport factor (FoM_{LTF}): It is given by equation 2.1(a). Figure 8.10 shows its trend for working fluid acetone, ammonia, octane and pentane. As can be clearly seen, its trend is similar to that $(h_l)_{max}$.

4. Numerical simulation results from Jasvanth et al.[217]: The trend of $(h_l)_{max}$ is compared with Q_{mic} (at 1 μm film length, 10 μm radius of curvature at the end of the thin film and 1K superheat), for the given set of working fluids, taken from Jasvanth et al.[217]. Here:

$$Q_{mic} = \int_0^x q''_{evap}\, dx \tag{8.10}$$

Where:

$$q''_{evap} = \frac{T_w - T_v\left(1 + \frac{P_v - P_l}{\rho_l \lambda}\right)}{\frac{\delta}{k_l} + \frac{2-\hat{\sigma}}{2\hat{\sigma}}\frac{\sqrt{2\pi R T_v}\,T_v}{\rho_v \lambda^2}} \tag{8.11}$$

Figure 8.11 shows the variation of Q_{mic}. As can be seen from the figure, the trend from figure 8.8(a) exactly matches with that from Jasvanth et al.[217]. However, as explained

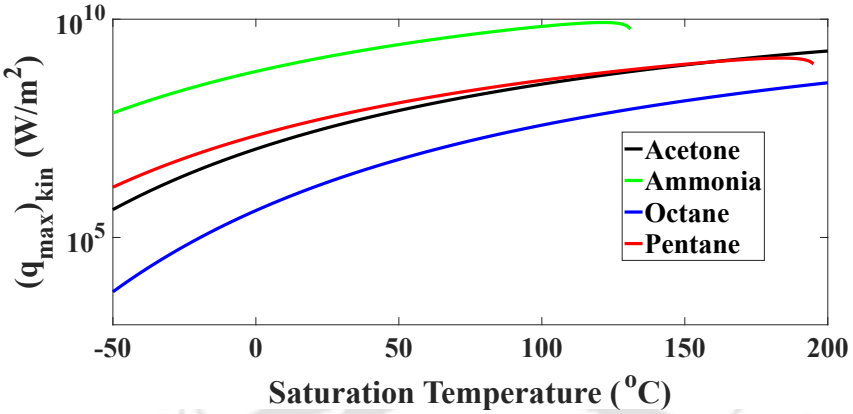

Figure 8.9: Variation of maximum heat flux limit

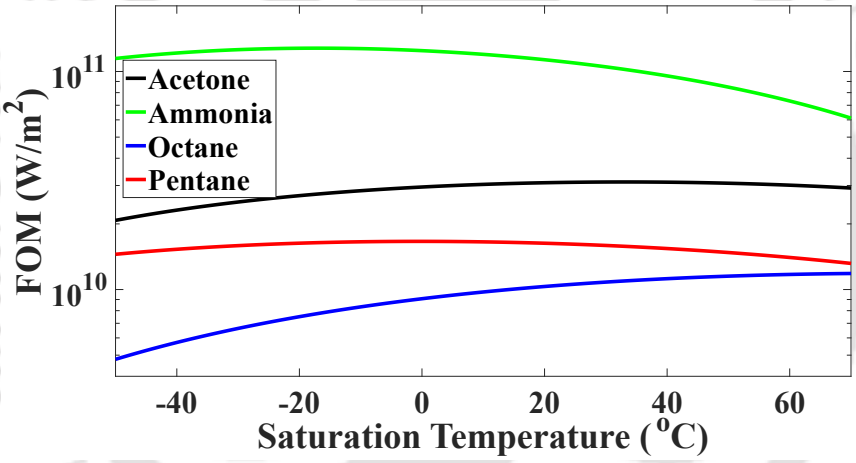

Figure 8.10: Variation of Liquid transport factor

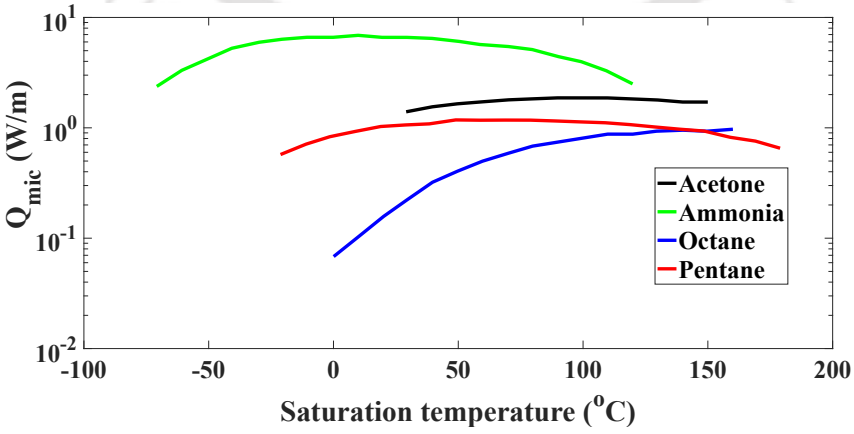

Figure 8.11: Variation of cumulative heat transfer (source: Jasvanth et al.[217])

before, to obtain their results, all the governing equations (6.1–6.8) need to be solved using a complicated algorithm (figure 7.1). Whereas the present method is comparatively less time consuming and requires minimal computational resource as one needs to do a simple explicit calculation using equation (8.7).

5. Figures of merit based on pressure drop in transport channels (equations 8.3–8.6): It was observed that their trends (shown by figures 8.3–8.6) were similar to that of $(h_l)_{max}$ except for pentane and acetone. As discussed in section 8.1.1, this is due to the different phenomenon that each criteria/figure of merit represents. While these figures of merit represent the pressure drop in the transport channels of the heat pipe, the parameter $(h_l)_{max}$ represents the heat transfer in the wick at the microscale level.

8.4 Discussion

In this study, the significance of $(\delta_0)_{min}$ is shown, defined as the film thickness where the liquid pressure is zero, (when the disjoining pressure equals the vapour pressure). Its correlation is shown by equation (6.15). Since the liquid pressure in the thin film region must always remain positive[166], [204], $(\delta_0)_{min}$ represents the lower limit of (δ_0), *i.e.* the film thickness at the onset of the thin-film region (figure 6.2). Hence, the corresponding heat transfer coefficient, designated as $(h_l)_{max}$ at $(\delta_0)_{min}$ is the highest attainable value of heat transfer coefficient for the thin-film region. Physically, it represents the heat transfer coefficient of the liquid column in a heated meniscus (inside a wick) when the liquid pressure is precisely zero. Hence, we propose the symbol $FoM_{(@P_l=0)}$ for its designation.

$(h_l)_{max}$ is calculated for four different working fluids for a wide range of saturation temperature (figure 8.8). Next, its trend is compared with that from literature, heat pipe figure of merit, maximum heat flux limit and interline heat flow parameter and observed that they all show similar trend.

Hence, we propose the parameter $(h_l)_{max}/FoM_{(@P_l=0)}$, as a figure of merit for devices utilizing thin-film evaporation. Its final expression is (from equation (8.7)):

$$(h_l)_{max} = FoM_{(@P_l=0)} = k_l \left(\frac{P_v}{A}\right)^{1/3}$$

Part IV

Closure

CHAPTER 9

CONCLUSIONS

COMPLETE development of a novel μlhp device is presented in this dissertation. It consists of design, optimization, fabrication, charging and finally, performance testing. The device is fabricated on a 2 inch silicon wafer using microfabrication technologies commonly used in the semiconductor field. Compared to other microfabrication technique employed in the literature, the methodology employed here is simple, economical and has less number of intermediate steps.

For numerical simulation of its evaporator, a new thin-film evaporation model is developed. It consists of the velocity slip boundary condition at the wall and a disjoining pressure consisting of both retarded and non-retarded terms.

This chapter is divided into two sections. The first section summarizes the results and explains all the conclusions obtained from them. In the second section, various aspects of the present study, which requires further investigation, are described, and is left for future studies.

9.1 Major contributions

9.1.1 Summary of study on μlhp device

1. Optimization study: The optimization equations of the micro loop heat pipe is developed from one-dimensional balance equations of mass and energy for different components of the device and momentum balance for the closed-loop. A code is developed in C to solve these equations. The heat transfer limit of the device is estimated from this model. As expected, the model shows that there is an optimum evaporator channel width for which the heat capacity reaches a maximum value. For a device length of 20 mm, the optimum evaporator channel width for which the heat transfer capacity reaches its upper limit is 6.4 μm. For higher device length of 70 mm and 120 mm, it becomes 3.4 μm and 2.5 μm respectively. This shows that the optimum evaporator channel width for a particular μlhp device lies in the same range independent of the device length.

2. New design: Based on this study, a micro loop heat pipe is designed, to be fabricated on a 2-inch silicon wafer. The overall length of this device is 3 cm, which is to the best of our

knowledge is second smallest. The credit of fabricating the smallest MEMS based μLHP goes to Wang et al.[123], having an overall length of 2 cm. But their fabrication technique was comparatively complicated (table 4.1).

3. Fabrication and charging: A simple fabrication methodology is developed, based on Singh et al.[197]. The silicon wafer is p-type and having orientation $\langle 1\,1\,0 \rangle$. This ensured that channels etched are of rectangular shape, as is evident from figures 4.3 and 4.4. Etchant used is TMAH (tetramethylammonium hydroxide). However, despite best effort, some deviations are obtained (figure 4.8). Moreover, since, it is a multi-step methodology, errors sustained in one step will always carry over to the next one. The details of each process in the fabrication methodology is shown in table 9.1.
   The charging process involves two steps. In the first step, the device is purged of any non-condensable gas with a vacuum pump. In the second step, working fluid is introduced into the device by taking advantage of the vacuum inside it. The disadvantage of this methodology is that the fluid flow into the device cannot be controlled and hence, the device is prone to flooding. Thus, the probability of a successful charge is very low using this process.

4. Performance test: Before charging, the device is connected with a valve, strip heater heat sink and thermocouples. The heat sink is connected with a constant temperature bath and placed below the condenser. The strip heater (placed below the evaporator) is connected with a DC power supply (figures 5.3 and 5.4). Using the DC power supply, the heat load is varied, and the resulting temperature is recorded.
   Results show that the start-up heat load of the device is in the range 1.5 to 4.0 W. A temperature reduction of 28.6 °C is attained at 3.78 W load. The heat leak parameter is also investigated and is found to have a linear relationship with heat load, as suggested in the literature.

9.1.2 Summary of study on thin-film evaporation theory

1. In the present work, various thin-film evaporation models available in the literature are analyzed for their capability to model the physics of the problem. Both their strengths and shortcomings are highlighted. It is observed that for most of these models, the governing equations are correct, problem lies in the implementation of boundary conditions. Following are the observation made on boundary conditions:

   (a) Film thickness at the onset of thin-film (δ_0): In literature, there are two distinct methodologies available to calculate δ_0 (figure 6.2). One using the Wayner's mass flux model ($(\delta_0)_{\text{way}}$ given by equation (6.11)) and the other using the Clausius-Clapeyron equation ($(\delta_0)_{\text{cc}}$ given by equation (6.12)). The problem with $(\delta_0)_{\text{way}}$ is that it results in negative liquid pressure in the thin-film region. Now, different researchers have asserted that the liquid pressure in this region cannot be negative[166], [204]. This can also be confirmed from the experimental data of Hanchak et al.[156]. $(\delta_0)_{\text{cc}}$ results in extremely low disjoining pressure at the onset of the thin-film region. This also goes against the physics of this phenomenon.

Table 9.1: Details of the processes used in the microfabrication

Process	**Remarks**
Cleaning	RCA cleaning
Oxidation	Equipment: 2-inch wet oxidation furnace Thickness of SiO_2 using Ellipsometer = 700 to 1000 nm
Pattern transfer	Photolithography using double sided aligner (DSA) Steps: 1. Pre-baking at 150°C for 15 minutes 2. PPR(S1813) coating at 3000 rpm for 30 seconds 3. The sample is exposed at 13.8 doses for 8 seconds. 4. Exposed PPR removed by treating the wafer with PPR developer (MF319) for 25 seconds. 5. The sample is checked under a microscope for any errors in pattern transfer.
Groove formation	Chemical etching using TMAH (substrate: Si, mask: SiO_2) Steps: 1. Exposed SiO_2 removed by BOE. 2. Remaining PPR removed by acetone. 3. The sample is then kept in a heated solution of TMAH vertically. 4. Etch rate at 70 to 80 °C recorded was 1.067 µm/min. 5. The sample is etched up to a depth of 150 to 160 µm/min. 6. The dimensions are checked using SEM or profilometer.
Sealing	PDMS bonding Steps: 1. PDMS and curing agent mixed in 10:1 ratio. 2. Mixture subjected to vacuum. 3. Mixture applied on the cover plate. 4. Cover plate rotated at 3000 rpm for 30 seconds and then 1500 rpm for 15 seconds.

In this study, it was observed that $(\delta_0)_{way}$ gives correct values only at extremely low superheat (<0.001 K), as shown in table 6.3 and $(\delta_0)_{cc}$ gives a reasonable value of δ_0 at high superheat (>10 K), as shown in figure 6.6. Hence, a new function to calculate (δ_0) is proposed for the intermediate range of superheat (0.001 to 10 K) represented by equation (6.17).

(b) Derivative of δ: As shown in table 6.1, various researchers have used different values of the first derivative and second derivative of δ at $x = 0$. For the present model, it is observed that the first derivative has a greater effect on the profile compared to the second derivative. This was also observed by Jung and Boo[206]. Hence, BC4 scheme is used to calculate $(\frac{d\delta}{dx})_{x=0}$ and $(\frac{d^2\delta}{dx^2})_{x=0}$.

(c) Interface temperature (T_{lv}): In literature, there are three different methods available to simulate the interface temperature of the heated meniscus given by equations (6.8), (6.9) and (6.10). They are all tested and its performance compared with the data from the literature (figure 7.2). It is observed that the result from equation (6.8) matches with that from literature (data taken from Wang et al.[150] and Hanchak et al.[156]).

2. A new thin-film evaporation model is developed, consisting of the velocity slip boundary condition at the wall and a disjoining pressure consisting of both retarded and non-retarded terms. This model is validated with both experimental and numerical data from the literature. After validation, parametric simulation is carried out. Variation of the following parameters: thin-film thickness, disjoining pressure, capillary pressure and mean velocity, along the meniscus length is investigated for different superheat. Its trend is found to match with that from the literature.

3. Using the new model, it is observed that the heat flux decreases monotonically throughout the thin-film and the intrinsic meniscus region. It reaches its maximum value in the interline region between adsorbed and thin-film region and from there its value drops significantly as it reaches the meniscus region. This trend is also observed in the molecular simulation of Maroo and Chung[11] and experimental data of Nazari et al.[138].

4. During the course of this research, a new parameter is discovered. It is the film thickness where the liquid pressure is exactly zero or when the disjoining pressure is equal to the vapour pressure. Since the liquid pressure is positive in the thin-film region, it can be argued that this parameter represents the lower limit of (δ_0) (refer figure 6.4) and hence is designated as $(\delta_0)_{min}$. Its expression is given by equation (6.15). As can be seen from the equation, it is independent of superheat and its value depends on two parameters: the dispersion constant and the saturated vapour pressure.
   This parameter provides an easy methodology to compare the film thickness of different working fluids in a heated as well as non-heated meniscus (figure 8.7).

5. Using $(\delta_0)_{min}$, $(h_l)_{max}$ is calculated. It is the corresponding heat transfer coefficient and is given by equation (8.7). It is the maximum attainable heat transfer coefficient of thin-film region.
   In this study, $(h_l)_{max}$ is proposed as a new figure of merit for devices utilizing thin-film

evaporation as a source of heat transfer (commonly found in heat pipes and other two-phase devices). To prove this, its trend is compared with four different figures of merit: the theoretical limit of heat flux (from the Kinetic theory of evaporation), heat pipe figure of merit, interline heat flow parameter and other parameters proposed in the literature. It is found that their trends are similar. Hence, $(h_l)_{max}$ can be used as a figure of merit. The advantage of this methodology is that it is simple and requires an explicit calculation involving three parameters only. $FoM_{(@P_l=0)}$ is proposed as its symbol.

Table 9.2 shows the application of the various figures of merit discussed in this thesis.

9.2 Future scope

The theoretical, as well as experimental study suggest that the micro loop heat pipe utilizing thin-film evaporation is an effective passive cooling device for electronics as well as any application subject to change in orientation and having space constraint. Although many important issues have been addressed in this study, there are still many opportunities for future work. They are summarized as follows:

1. A charging methodology specially designed for MEMS based micro heat pipes is required. This methodology should not only be able to control the flow of working fluid but also the final pressure of the device after charging.

2. Experimental validation of the proposed figure of merit is required. This can be achieved by experimentally investigating the performance of the present device with various working fluids.

3. More experimental study is required in the field of thin-film evaporation. The current model employs an exponential function to approximately determine δ_0. This can be improved and a more accurate function can be developed from experiments.

4. Owing to the complexity of the problem due to the multiscale nature of the film, many researchers[135], [136], [160], [182] have taken the mass flow rate at $x = 0$ (refer figure 6.2) to be zero, *i.e.* assumed that no heat transfer takes place in the adsorbed region (as also

Table 9.2: Operating range of the various figures of merit

Figures of merit	Application
FoM_{LTF}	High heat load
$FoM_{g\text{-}field}$	Anti-gravitational regime
FoM_{NTF}	Dry-out limit
FoM_{IL} and $FoM_{(@P_l=0)}$	Wick microscale heat transfer
K_{Pe}	Working fluid cooling capacity
K_1, K_2 and FoM_{joung}	Low to medium heat loads
$FoM_{yadavalli}$ and k_{vc}	Vapour chambers

followed in this study). However from figure 6.7, it can be inferred that some amount of heat transfer does takes place in the adsorbed region at higher superheat. Other studies[12], [167] have also questioned the validity of this assumption. Hence, a comprehensive study is required to properly investigate the heat transfer phenomenon in the transition region between the adsorbed and thin film region.

5. A complete mathematical model of the extended meniscus is desirable. This model shall combine the molecular simulation of the adsorbed region, thin-film and intrinsic meniscus.

REFERENCES

[1] Y. Cai, Y. Wang, D. Liu, and F.-Y. Zhao, "Thermoelectric cooling technology applied in the field of electronic devices: Updated review on the parametric investigations and model developments," *Applied Thermal Engineering*, vol. 148, pp. 238–255, 2019. DOI: 10.1016/j.applthermaleng.2018.11.014.

[2] A. R. M. Siddique, S. Mahmud, and B. Van Heyst, "A comprehensive review on a passive (phase change materials) and an active (thermoelectric cooler) battery thermal management system and their limitations," *Journal of Power Sources*, vol. 401, pp. 224–237, 2018. DOI: 10.1016/j.jpowsour.2018.08.094.

[3] T. Guclu and E. Cuce, "Thermoelectric coolers (tecs): From theory to practice," *Journal of Electronic Materials*, vol. 48, no. 1, pp. 211–230, 2019. DOI: 10.1007/s11664-018-6753-0.

[4] S. Pawar and D. K. Patel, "The impingement heat transfer data of inclined jet in cooling applications: A review," *Journal of Thermal Science*, vol. 29, no. 1, pp. 1–12, 2020. DOI: 10.1007/s11630-019-1200-y.

[5] P. Smakulski and S. Pietrowicz, "A review of the capabilities of high heat flux removal by porous materials, microchannels and spray cooling techniques," *Applied Thermal Engineering*, vol. 104, pp. 636–646, 2016. DOI: 10.1016/j.applthermaleng.2016.05.096.

[6] E. Alehosseini and S. M. Jafari, "Micro/nano-encapsulated phase change materials (pcms) as emerging materials for the food industry," *Trends in Food Science & Technology*, vol. 91, pp. 116–128, 2019. DOI: 10.1016/j.tifs.2019.07.003.

[7] M. Mofijur, T. M. I. Mahlia, A. S. Silitonga, H. C. Ong, M. Silakhori, M. H. Hasan, N. Putra, and S. Rahman, "Phase change materials (pcm) for solar energy usages and storage: An overview," *Energies*, vol. 12, no. 16, p. 3167, 2019. DOI: 10.3390/en12163167.

[8] M. Frigione, M. Lettieri, and A. Sarcinella, "Phase change materials for energy efficiency in buildings and their use in mortars," *Materials*, vol. 12, no. 8, p. 1260, 2019. DOI: 10.1016/j.applthermaleng.2017.08.161.

[9] T. Dixit and I. Ghosh, "Review of micro-and mini-channel heat sinks and heat exchangers for single phase fluids," *Renewable and Sustainable Energy Reviews*, vol. 41, pp. 1298–1311, 2015. DOI: 10.1016/j.ijthermalsci.2018.05.046.

[10] A.-C. Iradukunda, D. R. Huitink, and F. Luo, "A review of advanced thermal management solutions and the implications for integration in high-voltage packages," *IEEE Journal of Emerging and Selected Topics in Power Electronics*, vol. 8, no. 1, pp. 256–271, 2019. DOI: 10.1109/JESTPE.2019.2953102.

[11] S. C. Maroo and J. Chung, "Fundamental roles of nonevaporating film and ultrahigh heat flux associated with nanoscale meniscus evaporation in nucleate boiling," *Journal of Heat Transfer*, vol. 135, no. 6, p. 061 501, 2013. DOI: 10.1115/1.4023575.

[12] Y. Akkus, A. Koklu, and A. Beskok, "Atomic scale interfacial transport at an extended evaporating meniscus," *Langmuir*, vol. 35, no. 13, pp. 4491–4497, 2019. DOI: 10.1021/acs.langmuir.8b04219.

[13] S. Khandekar, "Crc handbook of thermal engineering," in. CRC Press, 2017, ch. Applications: Heat pipes, pp. 953–985. DOI: 10.4324/9781315119717.

[14] D. A. Reay, P. A. Kew, and R. J. McGlen, "Heat pipes," in. 2014, ch. Historical Development, pp. 1–13. DOI: 10.1016/C2011-0-08979-2.

[15] R. S. Gaugler, *Heat transfer device*, US Patent 2,350,348, 1944.

[16] G. M. Grover, *Evaporation-condensation heat transfer device*, US Patent 3,229,759, 1966.

[17] Y. F. Gerasimov, Y. F. Maidanik, G. T. Shchegolev, G. A. Filippov, L. G. Starikov, V. M. Kiseev, and Y. E. Dolgirev, "Low-temperature heat pipes with separate channels for vapor and liquid," *Journal of Engineering Physics*, vol. 28, no. 6, pp. 683–685, 1975. DOI: 10.1007/BF00867371.

[18] Y. F. Maidanik, "State-of-the-art of cpl and lhp technology," *Proc. of the 11th IHPC, Tokyo*, pp. 19–30, 1999.

[19] T. Cotter, "Principles and prospects of micro heat pipes," in *Proceedings of the 5th International Heat Pipe Conference*, Tsukuba, Japan, 1984, pp. 328–335.

[20] X. Chen, H. Ye, X. Fan, T. Ren, and G. Zhang, "A review of small heat pipes for electronics," *Applied Thermal Engineering*, vol. 96, pp. 1–17, 2016. DOI: 10.1016/j.applthermaleng.2015.11.048.

[21] H. Tang, Y. Tang, Z. Wan, J. Li, W. Yuan, L. Lu, Y. Li, and K. Tang, "Review of applications and developments of ultra-thin micro heat pipes for electronic cooling," *Applied energy*, vol. 223, pp. 383–400, 2018. DOI: 10.1016/j.apenergy.2018.04.072.

[22] P. Wayner Jr. and C. Coccio, "Heat and mass transfer in the vicinity of the triple interline of a meniscus," *AIChE journal*, vol. 17, pp. 569–574, 1971. DOI: 10.1002/aic.690170317.

[23] M. Potash Jr. and P. C. Wayner Jr., "Evaporation from a two-dimensional extended meniscus," *International Journal of Heat and Mass Transfer*, vol. 15, pp. 1851–1863, 1972. DOI: 10.1016/0017-9310(72)90058-0.

[24] P. Wayner, Y. Kao, and L. LaCroix, "The interline heat-transfer coefficient of an evaporating wetting film," *International Journal of Heat and Mass Transfer*, vol. 19, pp. 487–492, 1976. DOI: 10.1016/0017-9310(76)90161-7.

[25] R. W. Schrage, *A Theoretical Study of Interphase Mass Transfer*. Columbia University Press, 1953. [Online]. Available: https://books.google.co.in/books?id=2ztRAAAAMAAJ.

[26] F. Holm and S. Goplen, "Heat transfer in the meniscus thin-film transition region," *Journal of Heat Transfer*, vol. 101, pp. 543–547, 1979. DOI: 10.1115/1.3451025.

[27] P. Wayner Jr, "The effect of the london-van der waals dispersion force on interline heat transfer," *Journal of Heat Transfer*, vol. 100, no. 1, pp. 155–159, 1978. DOI: 10.1115/1.3450490.

[28] P. C. Wayner, "A Dimensionless Number for the Contact Line Evaporative Heat Sink," *Journal of Heat Transfer*, vol. 111, no. 3, pp. 813–815, 1989. DOI: 10.1115/1.3250758.

[29] N. S. Ramasamy, P. Kumar, B. Wangaskar, S. Khandekar, and Y. F. Maydanik, "Miniature ammonia loop heat pipe for terrestrial applications: Experiments and modeling," *International Journal of Thermal Sciences*, vol. 124, pp. 263–278, 2018. DOI: 10.1016/j.ijthermalsci.2017.10.018.

[30] E. W. Saaski, "Investigation of an inverted meniscus heat pipe wick concept," NASA, United States of America, Tech. Rep., 1975.

[31] S. Riffat and X. Ma, "Recent developments in heat pipe technology and applications: A review," *International Journal of Low-carbon Technologies*, vol. 2, no. 2, pp. 162–177, 2007. DOI: 10.1093/ijlct/2.2.162.

[32] W. Tian, S. He, Z. Liu, and W. Liu, "Experimental investigation of a miniature loop heat pipe with eccentric evaporator for cooling electronics," *Applied Thermal Engineering*, vol. 159, p. 113 982, 2019. DOI: 10.1016/j.applthermaleng.2019.113982.

[33] M. Chernysheva and Y. Maydanik, "Simulation of heat and mass transfer in a cylindrical evaporator of a loop heat pipe," *International Journal of Heat and Mass Transfer*, vol. 131, pp. 442–449, 2019. DOI: 10.1016/j.ijheatmasstransfer.2018.11.034.

[34] V. Pastukhov and Y. F. Maydanik, "Development and tests of a loop heat pipe with several separate heat sources," *Applied Thermal Engineering*, vol. 144, pp. 165–169, 2018. DOI: 10.1016/j.applthermaleng.2018.08.051.

[35] B. Xiao, W. Deng, Z. Ma, S. He, L. He, X. Li, F. Yuan, W. Liu, and Z. Liu, "Experimental investigation of loop heat pipe with a large squared evaporator for multi-heat sources cooling," *Renewable Energy*, vol. 147, pp. 239–248, 2020. DOI: 10.1016/j.renene.2019.08.142.

[36] Y. F. Maydanik, S. Vershinin, and M. Chernysheva, "Experimental study of an ammonia loop heat pipe with a flat disk-shaped evaporator using a bimetal wall," *Applied Thermal Engineering*, vol. 126, pp. 643–652, 2017. DOI: 10.1016/j.applthermaleng.2017.07.152.

[37] Y. F. Maydanik, M. A. Chernysheva, and V. Pastukhov, "Review: Loop heat pipes with flat evaporators," *Applied Thermal Engineering*, vol. 67, no. 1-2, pp. 294–307, 2014. DOI: 10.1016/j.applthermaleng.2014.03.041.

[38] Y. Chen, Y. Qu, and S. S. Zhang, "Design and Simulation of Visual Miniature Loop Heat Pipe," vol. 605-607, pp. 346–351, 2012. DOI: 10.4028/www.scientific.net/AMR.605-607.346.

[39] Z. Zhang, H. Zhang, Z. Liu, and W. Liu, "Experimental study of heat transfer capacity for loop heat pipe with flat disk evaporator," *Applied Thermal Engineering*, p. 115 183, 2020. DOI: 10.1016/j.applthermaleng.2020.115183.

[40] Y. F. Maydanik, "Loop heat pipes," *Applied thermal engineering*, vol. 25, no. 5-6, pp. 635–657, 2005. DOI: 10.1016/j.applthermaleng.2004.07.010.

[41] Y. Maydanik, S. Vershinin, and M. Chernysheva, "The results of comparative analysis and tests of ammonia loop heat pipes with cylindrical and flat evaporators," *Applied Thermal Engineering*, vol. 144, pp. 479–487, 2018. DOI: 10.1016/j.applthermaleng.2018.08.022.

[42] P. Wallin, "Heat pipe, selection of working fluid," *Heat and Mass Trasfer Project Report*, pp. 1–7, 2012.

[43] J. F. Morris, "Figure-of-merit calculation methods for organic heat-pipe fluids," Tech. Rep., 1973.

[44] L. M. Poplaski, S. P. Benn, and A. Faghri, "Thermal performance of heat pipes using nanofluids," *International Journal of Heat and Mass Transfer*, vol. 107, pp. 358–371, 2017. DOI: 10.1016/j.ijheatmasstransfer.2016.10.111.

[45] B. D. Marcus, *Theory and design of variable conductance heat pipes*. National Aeronautics and Space Administration, 1972.

[46] Y. Maydanik, S. Vershinin, and M. Chernysheva, "Investigation of thermal characteristics of a loop heat pipe in a wide range of external conditions," *International Journal of Heat and Mass Transfer*, vol. 147, p. 118 967, 2020. DOI: 10.1016/j.ijheatmasstransfer.2019.118967.

[47] S. Veeramachaneni, S. K. Pisipaty, D. R. Vedula, and A. B. Solomon, "Characterization of flat miniature loop heat pipe using water and methanol at different inclinations," *Experimental Heat Transfer*, pp. 1–23, 2020. DOI: 10.1080/08916152.2020.1800136.

[48] C.-C. Hsu, S.-W. Kang, and T.-F. Hou, "Performance testing of micro loop heat pipes," *Tamkang Journal of Science and Engineering*, vol. 8, no. 2, pp. 123–132, 2005.

[49] Y. Maydanik, V. Pastukhov, and M. Chernysheva, "Development and investigation of a loop heat pipe with a high heat-transfer capacity," *Applied Thermal Engineering*, vol. 130, pp. 1052–1061, 2018. DOI: 10.1016/j.applthermaleng.2017.11.084.

[50] M. Nishikawara, K. Otani, Y. Ueda, and H. Yanada, "Liquid–vapor phase behavior and operating characteristics of the capillary evaporator of a loop heat pipe at start-up," *International Journal of Thermal Sciences*, vol. 129, pp. 426–433, 2018. DOI: 10.1016/j.ijthermalsci.2018.03.023.

[51] X. Wang and J. Wei, "Visual investigation on startup characteristics of a novel loop heat pipe," *Applied Thermal Engineering*, vol. 105, pp. 198–208, 2016. DOI: 10.1016/j.applthermaleng.2016.05.156.

[52] W. Joung, K. Gam, K. Park, S. Ma, and J. Lee, "Transient responses of the flat evaporator loop heat pipe," *International Journal of Heat and Mass Transfer*, vol. 57, no. 1, pp. 131–141, 2013. DOI: 10.1016/j.ijheatmasstransfer.2012.10.025.

[53] S. Wang, W. Zhang, X. Zhang, and J. Chen, "Study on start-up characteristics of loop heat pipe under low-power," *International Journal of Heat and Mass Transfer*, vol. 54, no. 4, pp. 1002–1007, 2011. DOI: 10.1016/j.ijheatmasstransfer.2010.10.014.

[54] S. Launay, V. Platel, S. Dutour, and J.-L. Joly, "Transient modeling of loop heat pipes for the oscillating behavior study," *Journal of Thermophysics and Heat Transfer*, vol. 21, no. 3, pp. 487–495, 2007. DOI: 10.2514/1.26854.

[55] N. Watanabe, N. Phan, Y. Saito, S. Hayashi, N. Katayama, and H. Nagano, "Operating characteristics of an anti-gravity loop heat pipe with a flat evaporator that has the capability of a loop thermosyphon," *Energy Conversion and Management*, vol. 205, p. 112 431, 2020. DOI: 10.1016/j.enconman.2019.112431.

[56] Q. Zhang, G. Lin, X. Shen, L. Bai, and D. Wen, "Visualization study on the heat and mass transfer in the evaporator-compensation chamber of a loop heat pipe," *Applied Thermal Engineering*, vol. 164, p. 114 472, 2020. DOI: 10.1016/j.ijheatmasstransfer.2018.06.138.

[57] H. Wang, G. Lin, L. Bai, Y. Tao, and D. Wen, "Comparative study of two loop heat pipes using r134a as the working fluid," *Applied Thermal Engineering*, vol. 164, p. 114 459, 2020. DOI: 10.1016/j.applthermaleng.2019.114459.

[58] J. Choi and M. Jeong, "Preliminary design on high-end workstation cooling system using loop heat pipes," *Thermal Science and Engineering Progress*, p. 100 519, 2020. DOI: 10.1016/j.tsep.2020.100519.

[59] A. B. Solomon, A. K. Mahto, C. Joy, A. A. Rajan, D. A. Jayprakash, A. Dixit, and A. Sahay, "Application of bio-wick in compact loop heat pipe," *Applied Thermal Engineering*, p. 114 927, 2020. DOI: doi.org/10.1016/j.applthermaleng.2020.114927.

[60] H. Cho, L. Jin, and S. Jeong, "Experimental investigation on performances and characteristics of nitrogen-charged cryogenic loop heat pipe with wick-mounted condenser," *Cryogenics*, vol. 105, p. 102 970, 2020. DOI: 10.1016/j.cryogenics.2019.08.001.

[61] J. Ku, "Operating characteristics of loop heat pipes," SAE Technical Paper, Tech. Rep., 1999.

[62] J. He, J. Miao, L. Bai, G. Lin, H. Zhang, and D. Wen, "Effect of non-condensable gas on the startup of a loop heat pipe," *Applied Thermal Engineering*, vol. 111, pp. 1507–1516, 2017. DOI: 10.1016/j.applthermaleng.2016.07.154.

[63] Y. Zhao, S. Chang, B. Yang, W. Zhang, and M. Leng, "Experimental study on the thermal performance of loop heat pipe for the aircraft anti-icing system," *International Journal of Heat and Mass Transfer*, vol. 111, pp. 795–803, 2017. DOI: 10.1016/j.ijheatmasstransfer.2017.04.009.

[64] Z. Liu, D. Wang, C. Jiang, J. Yang, and W. Liu, "Experimental study on loop heat pipe with two-wick flat evaporator," *International Journal of Thermal Sciences*, vol. 94, pp. 9–17, 2015. DOI: 10.1016/j.ijthermalsci.2015.02.007.

[65] S. U. Khalid, H. Babar, H. M. Ali, M. M. Janjua, and M. A. Ali, "Heat pipes: Progress in thermal performance enhancement for microelectronics," *Journal of Thermal Analysis and Calorimetry*, 2020. DOI: 10.1007/s10973-020-09820-7.

[66] E. G. Jung and J. H. Boo, "Overshoot elimination of the evaporator wall temperature of a loop heat pipe through a bypass line," *Applied Thermal Engineering*, vol. 165, p. 114 594, 2020. DOI: 10.1016/j.applthermaleng.2019.114594.

[67] M. Khalili, A. M. Abolmaali, and M. Shafii, "Experimental and analytical study of thermohydraulic performance of a novel loop heat pipe with an innovative active temperature control method," *Applied Thermal Engineering*, vol. 143, pp. 964–976, 2018. DOI: 10.1016/j.applthermaleng.2018.08.008.

[68] Y. Yang, K. Zhu, Y. Wang, J. Wei, M. Zheng, and Z. Cui, "Experimental investigation and visual observation of a vapor–liquid separated flat loop heat pipe evaporator," *Applied Thermal Engineering*, vol. 101, pp. 71–78, 2016. DOI: 10.1016/j.applthermaleng.2016.01.100.

[69] K. Zhu, X. Chen, B. Dai, M. Zheng, Y. Wang, and H. Li, "Operation characteristics of a new-type loop heat pipe (lhp) with wick separated from heating surface in the evaporator," *Applied Thermal Engineering*, vol. 123, pp. 1034–1041, 2017. DOI: 10.1016/j.applthermaleng.2017.05.140.

[70] X. Li, K. Zhu, H. Li, X. Chen, and Y. Wang, "Performance comparison regarding loop heat pipes with different evaporator structures," *International Journal of Thermal Sciences*, vol. 136, pp. 86–95, 2019. DOI: 10.1016/j.ijthermalsci.2018.09.029.

[71] X. Lu and J.-J. Wei, "Experimental study on a novel loop heat pipe with both flat evaporator and boiling pool," *International Journal of Heat and Mass Transfer*, vol. 79, pp. 54–63, 2014. DOI: 10.1016/j.applthermaleng.2016.01.100.

[72] X. Wang, J. Wei, Y. Deng, Z. Wu, and B. Sundén, "Enhancement of loop heat pipe performance with the application of micro/nano hybrid structures," *International Journal of Heat and Mass Transfer*, vol. 127, pp. 1248–1263, 2018. DOI: 10.1016/j.ijheatmasstransfer.2018.06.138.

[73] V. Kiseev and O. Sazhin, "An experimental study of loop heat pipes with steam jet pump," *International Journal of Heat and Mass Transfer*, vol. 115, pp. 137–142, 2017. DOI: 10.1016/j.ijheatmasstransfer.2017.07.035.

[74] I. Setyawan, N. Putra, I. I. Hakim, and R. Irwansyah, "Development of hybrid loop heat pipe using pump assistance for cooling application on high heat flux device," *Journal of Mechanical Science and Technology*, vol. 33, no. 8, pp. 3685–3694, 2019. DOI: 10.1007/s12206-019-0710-6.

[75] H. Zhang, C. Jiang, Z. Zhang, Z. Liu, X. Luo, and W. Liu, "A study on thermal performance of a pump-assisted loop heat pipe with ammonia as working fluid," *Applied Thermal Engineering*, p. 115 342, 2020. DOI: 10.1016/j.applthermaleng.2020.115342.

[76] V. G. Pastukhov and Y. F. Maydanik, "Combined lhp and php based heat-transfer system," *International Journal of Thermal Sciences*, vol. 74, pp. 81–85, 2013.

[77] C. Petit, B. Siedel, D. Gloriod, V. Sartre, F. Lefèvre, and J. Bonjour, "Adsorption-based antifreeze system for loop heat pipes," *Applied Thermal Engineering*, vol. 78, pp. 704–711, 2015. DOI: 10.1016/j.applthermaleng.2014.11.028.

[78] L. Han, Y. Xie, J. Zhu, H. Wu, and H. Zhang, "Experimental and analytical study of dual compensation chamber loop heat pipe under acceleration force assisted condition," *International Journal of Heat and Mass Transfer*, vol. 153, p. 119 615, 2020. DOI: 10.1016/j.ijheatmasstransfer.2020.119615.

[79] L. Bai, Y. Tao, Y. Guo, and G. Lin, "Startup characteristics of a dual compensation chamber loop heat pipe with an extended bayonet tube," *International Journal of Heat and Mass Transfer*, vol. 148, p. 119 066, 2020. DOI: 10.1016/j.ijheatmasstransfer.2019.119066.

[80] Y. Xie, Y. Zhou, D. Wen, H. Wu, G. Haritos, and H. Zhang, "Experimental investigation on transient characteristics of a dual compensation chamber loop heat pipe subjected to acceleration forces," *Applied Thermal Engineering*, vol. 130, pp. 169–184, 2018.

[81] Y. Xie, J. Zhang, L. Xie, Y. Yu, H. Wu, H. Zhang, and H. Gao, "Experimental investigation on the operating characteristics of a dual compensation chamber loop heat pipe subjected to acceleration field," *Applied Thermal Engineering*, vol. 81, pp. 297–312, 2015.

[82] G. Lin, N. Li, L. Bai, and D. Wen, "Experimental investigation of a dual compensation chamber loop heat pipe," *International Journal of Heat and Mass Transfer*, vol. 53, no. 15-16, pp. 3231–3240, 2010.

[83] S. Du, Q. Zhang, P. Hou, C. Yue, and S. Zou, "Experimental study and steady-state model of a novel plate loop heat pipe without compensation chamber for cpu cooling," *Sustainable Cities and Society*, vol. 53, p. 101 894, 2020. DOI: 10.1016/j.scs.2019.101894.

[84] Y.-n. Zhao, T. Yan, J. Liang, and N. Wang, "A new way of supercritical startup of a cryogenic loop heat pipe," *International Journal of Heat and Mass Transfer*, vol. 145, p. 118 793, 2019. DOI: 10.1016/j.ijheatmasstransfer.2019.118793.

[85] Y. Guo, G. Lin, J. He, H. Zhang, J. Miao, and J. Li, "Supercritical startup strategy of cryogenic loop heat pipe with different working fluids," *Applied Thermal Engineering*, vol. 155, pp. 267–276, 2019. DOI: 10.1016/j.applthermaleng.2019.04.008.

[86] J. He, Y. Guo, H. Zhang, J. Miao, L. Wang, and G. Lin, "Design and experimental investigation of a neon cryogenic loop heat pipe," *Heat and Mass Transfer*, vol. 53, no. 11, pp. 3229–3239, 2017.

[87] H. Zhang, G. Li, L. Chen, G. Man, J. Miao, X. Ren, J. He, and Y. Huo, "Development of flat-plate loop heat pipes for spacecraft thermal control," *Microgravity Science and Technology*, vol. 31, no. 4, pp. 435–443, 2019. DOI: 10.1007/s12217-019-09716-8.

[88] V. Jasvanth, A. A. Adoni, V. Jaikumar, and A. Ambirajan, "Design and testing of an ammonia loop heat pipe," *Applied Thermal Engineering*, vol. 111, pp. 1655–1663, 2017.

[89] T. Ding, C. Liu, M. Li, J. Miao, Y. Guo, and X. Bu, "Design and experimental study of deployable radiator based on loop heat pipes," in *Mechanical and Aerospace Engineering (ICMAE), 2017 8th International Conference on*, IEEE, 2017, pp. 286–291.

[90] T. M. Diallo, M. Yu, J. Zhou, X. Zhao, J. Ji, and D. Hardy, "Analytical investigation of the heat-transfer limits of a novel solar loop-heat pipe employing a mini-channel evaporator," *Energies*, vol. 11, no. 1, p. 148, 2018. DOI: 10.3390/en11010148.

[91] X. Zhang, X. Zhao, J. Xu, and X. Yu, "Characterization of a solar photovoltaic/loop-heat-pipe heat pump water heating system," *Applied Energy*, vol. 102, pp. 1229–1245, 2013.

[92] J.-C. Jang, R.-G. Chi, S.-H. Rhi, K.-B. Lee, H.-C. Hwang, J.-S. Lee, and W.-H. Lee, "Heat pipe-assisted thermoelectric power generation technology for waste heat recovery," *Journal of Electronic Materials*, vol. 44, no. 6, pp. 2039–2047, 2015.

[93] V. G. PastUkhov, Y. F. Maidanik, C. Vershinin, and M. Korukov, "Miniature loop heat pipes for electronics cooling," *Applied Thermal Engineering*, vol. 23, no. 9, pp. 1125–1135, 2003. DOI: 10.1016/S1359-4311(03)00046-2.

[94] Y. F. Maydanik, S. V. Vershinin, M. A. Korukov, and J. M. Ochterbeck, "Miniature loop heat pipes-a promising means for cooling electronics," *IEEE Transactions on Components and Packaging Technologies*, vol. 28, no. 2, pp. 290–296, 2005. DOI: 10.1109/TCAPT.2005.848487.

[95] G. Zhou, J. Li, and L. Lv, "An ultra-thin miniature loop heat pipe cooler for mobile electronics," *Applied Thermal Engineering*, vol. 109, pp. 514–523, 2016. DOI: 10.1016/j.applthermaleng.2016.08.138.

[96] G. Zhou, J. Li, and Z. Jia, "Power-saving exploration for high-end ultra-slim laptop computers with miniature loop heat pipe cooling module," *Applied Energy*, vol. 239, pp. 859–875, 2019. DOI: 10.1016/j.apenergy.2019.01.258.

[97] P. Kumar, S. Khandekar, Y. F. Maydanik, and B. Bhattacharya, "Effect of vibrations on thermal performance of miniature loop heat pipe for avionics cooling: An experimental analysis," *Journal of Heat Transfer*, vol. 141, no. 9, 2019. DOI: 10.1115/1.4044466.

[98] H. Ye, R. Sokolovskij, H. W. van Zeijl, A. W. Gielen, and G. Zhang, "A polymer based miniature loop heat pipe with silicon substrate and temperature sensors for high brightness light-emitting diodes," *Microelectronics Reliability*, vol. 54, no. 6-7, pp. 1355–1362, 2014. DOI: 10.1016/j.microrel.2014.02.032.

[99] Y. Guo, G. Lin, J. He, L. Bai, Y. Sun, H. Zhang, and J. Miao, "Experimental analysis of operation failure for a neon cryogenic loop heat pipe," *International Journal of Heat and Mass Transfer*, vol. 138, pp. 96–108, 2019. DOI: 10.1016/j.ijheatmasstransfer.2019.04.045.

[100] Y. Guo, G. Lin, L. Bai, J. Miao, and G. Peterson, "Experimental study of the thermal performance of a neon cryogenic loop heat pipe," *International Journal of Heat and Mass Transfer*, vol. 120, pp. 1266–1274, 2018. DOI: 10.1016/j.ijheatmasstransfer.2017.12.138.

[101] L. Bai, G. Lin, H. Zhang, J. Miao, and D. Wen, "Effect of component layout on the operation of a miniature cryogenic loop heat pipe," *International Journal of Heat and Mass Transfer*, vol. 60, pp. 61–68, 2013. DOI: 10.1016/j.ijheatmasstransfer.2013.01.011.

[102] R. Singh, A. Akbarzadeh, and M. Mochizuki, "Effect of wick characteristics on the thermal performance of the miniature loop heat pipe," *Journal of Heat transfer*, vol. 131, no. 8, p. 082 601, 2009. DOI: 10.1115/1.3109994.

[103] R. Singh, A. Akbarzadeh, C. Dixon, and M. Mochizuki, "Theoretical modelling of miniature loop heat pipe," *Heat and mass transfer*, vol. 46, no. 2, p. 209, 2009. DOI: 10.1007/s00231-009-0504-y.

[104] Y. F. Maydanik and S. V. Vershinin, "Development and tests of ammonia miniature loop heat pipes with cylindrical evaporators," *Applied Thermal Engineering*, vol. 29, no. 11-12, pp. 2297–2301, 2009. DOI: 10.1016/j.applthermaleng.2008.11.016.

[105] M. Nishikawara and H. Nagano, "Parametric experiments on a miniature loop heat pipe with ptfe wicks," *International Journal of Thermal Sciences*, vol. 85, pp. 29–39, 2014. DOI: 10.1016/j.ijthermalsci.2014.05.016.

[106] A. R. Anand, A. Jaiswal, A. Ambirajan, and P. Dutta, "Experimental studies on a miniature loop heat pipe with flat evaporator with various working fluids," *Applied Thermal Engineering*, vol. 144, pp. 195–503, 2018. DOI: 10.1016/j.applthermaleng.2018.08.092.

[107] T. Tharayil, L. G. Asirvatham, V. Ravindran, and S. Wongwises, "Effect of filling ratio on the performance of a novel miniature loop heat pipe having different diameter transport lines," *Applied Thermal Engineering*, vol. 106, pp. 588–600, 2016. DOI: 10.1016/j.applthermaleng.2016.05.125.

[108] D. Gai, Z. Liu, W. Liu, and J. Yang, "Operational characteristics of miniature loop heat pipe with flat evaporator," *Heat and mass transfer*, vol. 46, no. 2, p. 267, 2009. DOI: 10.1007/s00231-009-0563-0.

[109] S. Vershinin and Y. F. Maydanik, "Investigation of pulsations of the operating temperature in a miniature loop heat pipe," *International Journal of Heat and Mass Transfer*, vol. 50, no. 25-26, pp. 5232–5240, 2007. DOI: 10.1016/j.ijheatmasstransfer.2007.06.024.

[110] Y. Chen, M. Groll, R. Mertz, Y. F. Maydanik, and S. Vershinin, "Steady-state and transient performance of a miniature loop heat pipe," *International Journal of Thermal Sciences*, vol. 45, no. 11, pp. 1084–1090, 2006. DOI: 10.1016/j.ijthermalsci.2006.02.003.

[111] R. Singh, A. Akbarzadeh, and M. Mochizuki, "Operational characteristics of a miniature loop heat pipe with flat evaporator," *International Journal of Thermal Sciences*, vol. 47, no. 11, pp. 1504–1515, 2008. DOI: 10.1007/s00231-009-0563-0.

[112] R. Singh, A. Akbarzadeh, and M. Mochizuki, "Operational characteristics of the miniature loop heat pipe with non-condensable gases," *International Journal of Heat and Mass Transfer*, vol. 53, no. 17-18, pp. 3471–3482, 2010. DOI: 10.1016/j.ijheatmasstransfer.2010.04.008.

[113] A. Anand, "Investigations on effect of noncondensable gas in a loop heat pipe with flat evaporator on de-prime," *International Journal of Heat and Mass Transfer*, vol. 143, p. 118 531, 2019. DOI: 10.1016/j.ijheatmasstransfer.2019.118531.

[114] T. Tharayil, L. G. Asirvatham, V. Ravindran, and S. Wongwises, "Thermal performance of miniature loop heat pipe with graphene–water nanofluid," *International Journal of heat and mass transfer*, vol. 93, pp. 957–968, 2016. DOI: 10.1016/j.ijheatmasstransfer.2015.11.011.

[115] T. Tharayil, L. G. Asirvatham, M. J. Dau, and S. Wongwises, "Entropy generation analysis of a miniature loop heat pipe with graphene–water nanofluid: Thermodynamics model and experimental study," *International Journal of Heat and Mass Transfer*, vol. 106, pp. 407–421, 2017. DOI: 10.1016/j.ijheatmasstransfer.2016.08.035.

[116] D. Venkata Krishnan, G. Udaya Kumar, S. Suresh, M. R. Thansekhar, and U. Iqbal, "Evaluating the scale effects of metal nanowire coatings on the thermal performance of miniature loop heat pipe," *Applied Thermal Engineering*, vol. 133, pp. 727–738, 2018. DOI: 10.1016/j.applthermaleng.2018.01.052.

[117] T. Tharayil, L. G. Asirvatham, S. Rajesh, and S. Wongwises, "Effect of nanoparticle coating on the performance of a miniature loop heat pipe for electronics cooling applications," *Journal of Heat Transfer*, vol. 140, no. 2, p. 022 401, 2018. DOI: 10.1115/1.4037541.

[118] T. Tharayil, L. G. Asirvatham, S. Rajesh, and S. Wongwises, "Thermal management of electronic devices using combined effects of nanoparticle coating and graphene–water nanofluid in a miniature loop heat pipe," *IEEE Transactions On Components, Packaging and Manufacturing Technology*, vol. 8, no. 7, pp. 1241–1253, 2018. DOI: 10.1109/TCPMT.2018.2846561.

[119] D. Cytrynowicz, M. Hamdan, P. Medis, A. Shuja, H. T. Henderson, F. M. Gerner, and E. Golliher, "Mems loop heat pipe based on coherent porous silicon technology," in *AIP Conference Proceedings*, AIP, vol. 608, 2002, pp. 220–232. DOI: 10.1063/1.1449729.

[120] D. Cytrynowicz, M. Hamdan, P. Medis, H. T. Henderson, and F. M. Gerner, "Test cell for a novel planar mems loop heat pipe based on coherent porous silicon," in *AIP Conference Proceedings*, AIP, vol. 654, 2003, pp. 227–238. DOI: 10.1063/1.1541298.

[121] D. Cytrynowicz, P. Medis, S. Parimi, A. Shuja, H. Thurman Henderson, and F. M. Gerner, "The mems loop heat pipe based on coherent porous silicon—the modified system test structure," in *AIP Conference Proceedings*, AIP, vol. 699, 2004, pp. 164–173. DOI: 10.1063/1.1649571.

[122] K. Fukushima and H. Nagano, "New evaporator structure for micro loop heat pipes," *International Journal of Heat and Mass Transfer*, vol. 106, pp. 1327–1334, 2017. DOI: 10.1016/j.ijheatmasstransfer.2016.10.116.

[123] C. Wang, Y. Kazoe, K. Morikawa, H. Shimizu, Y. Pihosh, K. Mawatari, and T. Kitamori, "Micro heat pipe device utilizing extended nanofluidics," *RSC Advances*, vol. 7, no. 80, pp. 50 591–50 597, 2017. DOI: 10.1039/C7RA10017E.

[124] N. S. Dhillon and A. P. Pisano, "Enabling two-phase microfluidic thermal transport systems using a novel thermal-flux degassing and fluid charging approach," *Journal of Micromechanics and Microengineering*, vol. 24, no. 3, p. 035 021, 2014. DOI: 10.1088/0960-1317/24/3/035021.

[125] T. Shioga, Y. Mizuno, and H. Nagano, "Operating characteristics of a new ultra-thin loop heat pipe," *International Journal of Heat and Mass Transfer*, vol. 151, p. 119 436, 2020. DOI: 10.1016/j.ijheatmasstransfer.2020.119436.

[126] T. Shioga and Y. Mizuno, "Micro loop heat pipe for mobile electronics applications," in *31st Thermal Measurement, Modeling & Management Symposium (SEMI-THERM)*, IEEE, 2015, pp. 50–55. DOI: 10.1109/SEMI-THERM.2015.7100139.

[127] M. Ghajar, J. Darabi, and N. Crews, "A hybrid CFD-mathematical model for simulation of a MEMS loop heat pipe for electronics cooling applications," *Journal of Micromechanics and Microengineering*, vol. 15, pp. 313–321, 2005. DOI: 10.1088/0960-1317/15/2/010.

[128] M. Ghajar and J. Darabi, "Numerical modeling of evaporator surface temperature of a micro loop heat pipe at steady-state condition," *Journal of Micromechanics and Microengineering*, vol. 15, pp. 1963–1971, 2005. DOI: 10.1088/0960-1317/15/10/024.

[129] M. Ghajar and J. Darabi, "Evaporative heat transfer analysis of a micro loop heat pipe with rectangular grooves," *International Journal of Thermal Sciences*, vol. 79, pp. 51–59, 2014. DOI: 10.1016/j.ijthermalsci.2013.12.014.

[130] E. G. Jung and J. H. Boo, "A novel transient thermohydraulic model of micro-channel heat sink," *International Journal of Heat and Mass Transfer*, vol. 145, p. 118 772, 2019. DOI: 10.1016/j.ijheatmasstransfer.2019.118772.

[131] Y. Yamada, M. Nishikawara, H. Yanada, and Y. Ueda, "Predicting the performance of a loop heat pipe considering evaporation from the meniscus at the three-phase contact line," *Thermal Science and Engineering Progress*, 2019. DOI: 10.1016/j.tsep.2019.03.022.

[132] E. G. Jung and J. H. Boo, "A novel transient thermohydraulic model of a micro heat pipe," *International Journal of Heat and Mass Transfer*, vol. 140, pp. 819–827, 2019. DOI: 10.1016/j.ijheatmasstransfer.2019.06.041.

[133] E. G. Jung and J. H. Boo, "A numerical modeling for the steady-state performance of a micro heat pipe using thin liquid film theory," *International Journal of Heat and Mass Transfer*, vol. 126, pp. 557–566, 2018. DOI: 10.1016/j.ijheatmasstransfer.2018.05.067.

[134] E. G. Jung and J. H. Boo, "A numerical study on the heat and mass transfer of a micro heat pipe with a phase-change interface analysis," *Heat and Mass Transfer*, vol. 53, pp. 3363–3372, 2017. DOI: 10.1007/s00231-017-2074-8.

[135] R. Mandel, A. Shooshtari, and M. Ohadi, "Thin-film evaporation on microgrooved heatsinks," *Numerical Heat Transfer; Part A: Applications*, vol. 71, pp. 111–127, 2017. DOI: 10.1080/10407782.2016.1257300.

[136] H. Hu, J. A. Weibel, and S. V. Garimella, "Role of nanoscale roughness in the heat transfer characteristics of thin film evaporation," *International Journal of Heat and Mass Transfer*, vol. 150, p. 119 306, 2020. DOI: 10.1016/j.ijheatmasstransfer.2020.119306.

[137] M. H. Matin, A. Fazeli, and S. Moghaddam, "Thermographic characterization of ultra-thin liquid films formation and evaporation in microchannels," *Lab on a Chip*, pp. 2610–2618, 2019. DOI: 10.1039/c9lc00301k.

[138] M. Nazari, A. Masoudi, P. Jafari, P. Irajizad, V. Kashyap, and H. Ghasemi, "Ultrahigh evaporative heat fluxes in nanoconfined geometries," *Langmuir*, vol. 35, no. 1, pp. 78–85, 2019. DOI: 10.1021/acs.langmuir.8b03463.

[139] L. Zhang, Y. Zhu, Z. Lu, L. Zhao, K. R. Bagnall, S. R. Rao, and E. N. Wang, "Characterization of thin film evaporation in micropillar wicks using micro-raman spectroscopy," *Applied Physics Letters*, vol. 113, no. 16, p. 163 701, 2018. DOI: 10.1063/1.5048837.

[140] K. L. Wilke, B. Barabadi, Z. Lu, T. Zhang, and E. N. Wang, "Parametric study of thin film evaporation from nanoporous membranes," *Applied Physics Letters*, vol. 111, no. 17, p. 171 603, 2017. DOI: 10.1063/1.4997945.

[141] J. B. Freund, "The atomic detail of an evaporating meniscus," *Physics of Fluids*, vol. 17, p. 022 104, 2005. DOI: 10.1063/1.1843871.

[142] K. Park, K.-J. Noh, and K.-S. Lee, "Transport phenomena in the thin-film region of a micro-channel," *International Journal of Heat and Mass Transfer*, vol. 46, pp. 2381–2388, 2003. DOI: 10.1016/S0017-9310(02)00541-0.

[143] J. J. Zhao, Y. Y. Duan, X. D. Wang, and B. X. Wang, "Effects of superheat and temperature-dependent thermophysical properties on evaporating thin liquid films in microchannels," *International Journal of Heat and Mass Transfer*, vol. 54, pp. 1259–1267, 2011. DOI: 10.1016/j.ijheatmasstransfer.2010.10.026.

[144] J.-J. Zhao, M. Huang, Q. Min, D. M. Christopher, and Y.-Y. Duan, "Near-wall liquid layering, velocity slip, and solid–liquid interfacial thermal resistance for thin-film evaporation in microchannels," *Nanoscale and Microscale Thermophysical Engineering*, vol. 15, no. 2, pp. 105–122, 2011. DOI: 10.1080/15567265.2011.560927.

[145] A. J. Shkarah, B. Sulaiman, M. Yusoff, M. bin Hj Ayob, *et al.*, "Analytical solutions of heat transfer and film thickness with slip condition effect in thin-film evaporation for two-phase flow in microchannel," *Mathematical Problems in Engineering*, vol. 2015, 2015. DOI: 10.1155/2015/369581.

[146] L. Biswal, S. Som, and S. Chakraborty, "Thin film evaporation in microchannels with interfacial slip," *Microfluidics and Nanofluidics*, vol. 10, no. 1, pp. 155–163, 2011. DOI: 10.1007/s10404-010-0655-7.

[147] J.-J. Zhao, X.-F. Peng, and Y.-Y. Duan, "Slip and micro flow characteristics near a wall of evaporating thin films in a micro channel," *Heat Transfer-Asian Research*, vol. 39, pp. 460–474, 2010. DOI: 10.1002/htj.20310.

[148] S.-K. Wee, K. D. Kihm, and K. P. Hallinan, "Effects of the liquid polarity and the wall slip on the heat and mass transport characteristics of the micro-scale evaporating transition film," *International journal of heat and mass transfer*, vol. 48, no. 2, pp. 265–278, 2005. DOI: 10.1016/j.ijheatmasstransfer.2004.08.021.

[149] S. Moosman and G. Homsy, "Evaporating menisci of wetting fluids," *Journal of Colloid and Interface Science*, vol. 73, pp. 212–223, 1980. DOI: 10.1016/0021-9797(80)90138-1.

[150] H. Wang, S. V. Garimella, and J. Y. Murthy, "Characteristics of an evaporating thin film in a microchannel," *International Journal of Heat and Mass Transfer*, vol. 50, pp. 3933–3942, 2007. DOI: 10.1016/j.ijheatmasstransfer.2007.01.052.

[151] Z. H. Kou, H. T. Lv, W. Zeng, M. L. Bai, and J. Z. Lv, "Comparison of different analytical models for heat and mass transfer characteristics of an evaporating meniscus in a micro-channel," *International Communications in Heat and Mass Transfer*, vol. 63, pp. 49–53, 2015. DOI: 10.1016/j.icheatmasstransfer.2015.02.005.

[152] A. Setchi, Y. Chen, J. Yu, and H. Wang, "Structural effects in partially-wetting thin evaporating liquid films near the contact line," *International Journal of Heat and Mass Transfer*, vol. 132, pp. 420–430, 2019. DOI: 10.1016/j.ijheatmasstransfer.2018.11.151.

[153] S. Y. Du and Y. H. Zhao, "New boundary conditions for the evaporating thin-film model in a rectangular micro channel," *International Journal of Heat and Mass Transfer*, vol. 54, pp. 3694–3701, 2011. DOI: 10.1016/j.ijheatmasstransfer.2011.02.059.

[154] H. Azarkish, A. Behzadmehr, U. De Sherbrooke, T. F. Sheikholeslami, S. Masoud, and H. Sarvari, "A modified disjoining pressure model for thin film evaporation of water," in *ASME International Mechanical Engineering Congress and Exposition*, 2013, V07BT08A007. DOI: 10.1115/IMECE2013-62986.

[155] L. Biswal, S. Som, and S. Chakraborty, "Thin film evaporation in microchannels with slope-and curvature-dependent disjoining pressure," *International Journal of Heat and Mass Transfer*, vol. 57, pp. 402–410, 2013. DOI: 10.1016/j.ijheatmasstransfer.2012.10.022.

[156] M. S. Hanchak, M. D. Vangsness, L. W. Byrd, and J. S. Ervin, "Thin film evaporation of n-octane on silicon: Experiments and theory," *International Journal of Heat and Mass Transfer*, vol. 75, pp. 196–206, 2014. DOI: 10.1016/j.ijheatmasstransfer.2014.03.063.

[157] S. Morris, M. Sellier, and A. R. A. Behadili, "Comparison of lubrication approximation and navier-stokes solutions for dam-break flows in thin films," *arXiv preprint arXiv:1708.00976*, 2017.

[158] H. Ma, P. Cheng, B. Borgmeyer, and Y. Wang, "Fluid flow and heat transfer in the evaporating thin film region," *Microfluidics and Nanofluidics*, vol. 4, no. 3, pp. 237–243, 2008. DOI: 10.1007/s10404-007-0172-5.

[159] C. Yan, X. Pan, and X. Lu, "Mechanisms of Thin-Film Evaporation Considering Momentum and Energy Conservation," in *ASME 2013 4th International Conference on Micro/Nanoscale Heat and Mass Transfer*, 2013, V001T11A007. DOI: 10.1115/MNHMT2013-22157.

[160] B. Fu, N. Zhao, B. Tian, W. Corey, and H. Ma, "Evaporation Heat Transfer in Thin-Film Region With Bulk Vapor Flow Effect," *Journal of Heat Transfer*, vol. 140, p. 011 502, 2018. DOI: 10.1115/1.4037448.

[161] A. Mirzamoghadam and I. Catton, "A physical model of the evaporating meniscus," *Journal of Heat Transfer*, vol. 110, no. 1, pp. 201–207, 1988. DOI: 10.1115/1.3250452.

[162] K. P. Hallinan, S. J. Kim, and W. S. Chang, "Evaporation from an extended meniscus for nonisothermal interfacial conditions," *Journal of Thermophysics and Heat Transfer*, vol. 8, pp. 709–716, 1994. DOI: 10.2514/3.602.

[163] E. Lim, Y. M. Hung, and B. T. Tan, "A hydrodynamic analysis of thermocapillary convection in evaporating thin liquid films," *International Journal of Heat and Mass Transfer*, vol. 108, pp. 1103–1114, 2017. DOI: 10.1016/j.ijheatmasstransfer.2016.12.111.

[164] E. Lim, T. C. Kueh, and Y. M. Hung, "Inverse-thermocapillary evaporation in a thin liquid film of self-rewetting fluid," *International Journal of Numerical Methods for Heat & Fluid Flow*, 2020. DOI: 10.1108/HFF-05-2020-0266.

[165] V. Jasvanth, A. Ambirajan, A. A. Adoni, and J. H. Arakeri, "Numerical investigation of an evaporating meniscus in a heated capillary slot," *Heat and Mass Transfer*, vol. 55, no. 12, pp. 3675–3688, 2019. DOI: 10.1007/s00231-019-02672-4.

[166] Y. Akkuş and Z. Dursunkaya, "A new approach to thin film evaporation modeling," *International Journal of Heat and Mass Transfer*, vol. 101, pp. 742–748, 2016. DOI: 10.1016/j.ijheatmasstransfer.2016.05.091.

[167] K. Bellur, E. F. Médici, C. K. Choi, J. C. Hermanson, and J. S. Allen, "Multiscale approach to model steady meniscus evaporation in a wetting fluid," *Physical Review Fluids*, vol. 5, p. 024 001, 2020. DOI: 10.1103/PhysRevFluids.5.024001.

[168] C. Zhang, F. Hong, and P. Cheng, "Simulation of liquid thin film evaporation and boiling on a heated hydrophilic microstructured surface by Lattice Boltzmann method," *International Journal of Heat and Mass Transfer*, vol. 86, pp. 629–638, 2015. DOI: 10.1016/j.ijheatmasstransfer.2015.03.029.

[169] W. Yang, H. Huang, and W. Yan, "Thermal lattice boltzmann simulation of evaporating thin liquid film for vapor generation," *Multidisciplinary Digital Publishing Institute*, vol. 8, no. 5, p. 798, 2018. DOI: 10.3390/app8050798.

[170] W. Yang, H. Li, M. H. Alhosani, and T. Zhang, "Prediction of thin liquid film evaporation characteristics with a thermal lattice boltzmann method," in *15th IEEE Intersociety Conference on Thermal and Thermomechanical Phenomena in Electronic Systems (ITherm)*, IEEE, 2016, pp. 1240–1247. DOI: 10.1109/ITHERM.2016.7517689.

[171] S. DasGupta, J. A. Schonberg, and P. C. Wayner, "Investigation of an Evaporating Extended Meniscus Based on the Augmented Young–Laplace Equation," *Journal of Heat Transfer*, vol. 115, pp. 201–208, 1993. DOI: 10.1115/1.2910649.

[172] R. Argade, S. Ghosh, S. De, and S. DasGupta, "Experimental investigation of evaporation and condensation in the contact line region of a thin liquid film experiencing small thermal perturbations," *Langmuir*, vol. 23, no. 3, pp. 1234–1241, 2007.

[173] M. S. Hanchak, L. W. Byrd, M. D. Vangsness, J. S. Ervin, and J. G. Jones, "Thin film evaporation model with retarded van der waals interaction," in *ASME International Mechanical Engineering Congress and Exposition*, San Diego, California, USA, 2013. DOI: 10.1115/IMECE2013-62397.

[174] A. A. Arends, T. M. Germain, J. F. Owens, and S. A. Putnam, "Simultaneous reflectometry and interferometry for measuring thin-film thickness and curvature," *Review of Scientific Instruments*, vol. 89, p. 055 117, 2018. DOI: 10.1063/1.5021704.

[175] M. S. Hanchak, M. D. Vangsness, J. S. Ervin, and L. W. Byrd, "Model and experiments of the transient evolution of a thin, evaporating liquid film," *International Journal of Heat and Mass Transfer*, vol. 92, pp. 757–765, 2016. DOI: 10.1016/j.ijheatmasstransfer.2015.09.051.

[176] D. H. Shin, J. S. Allen, C. K. Choi, and S. H. Lee, "Visualization of an evaporating thin layer during the evaporation of a nanofluid droplet," *Langmuir*, vol. 31, pp. 1237–1241, 2015. DOI: 10.1021/la504133h.

[177] L. Fung and M. Kawaji, "Measurement of liquid film thickness in slug flow of air and viscous liquid in a microchannel," in *ASME 13th International Conference on Nanochannels, Microchannels, and Minichannels collocated with the ASME 2015 International Technical Conference and Exhibition on Packaging and Integration of Electronic and Photonic Microsystems*, American Society of Mechanical Engineers, 2015. DOI: 10.1115/ICNMM2015-48663.

[178] L. Tachon and S. Guignard, "An accurate optical method for the measurement of contact angle and interface shape of evaporative thin liquids films," *Experimental Thermal and Fluid Science*, vol. 90, pp. 66–75, 2017. DOI: 10.1016/j.expthermflusci.2017.08.011.

[179] C. Höhmann and P. Stephan, "Microscale temperature measurement at an evaporating liquid meniscus," *Experimental Thermal and Fluid Science*, vol. 26, pp. 157–162, 2002. DOI: 10.1016/S0894-1777(02)00122-X.

[180] C. Sodtke, J. Kern, N. Schweizer, and P. Stephan, "High resolution measurements of wall temperature distribution underneath a single vapour bubble under low gravity conditions," *International Journal of Heat and Mass Transfer*, vol. 49, pp. 1100–1106, 2006. DOI: 10.1016/j.ijheatmasstransfer.2005.07.054.

[181] X. Xu and V. Carey, "Film evaporation from a micro-grooved surface- an approximate heat transfer model and its comparison with experimental data," *Journal of Thermophysics and Heat Transfer*, vol. 4, pp. 512–520, 1990. DOI: 10.2514/3.215.

[182] V. S. Jasvanth, A. Ambirajan, and J. H. Arakeri, "Experimental study on evaporation of pentane from a heated capillary slot," *International Journal of Heat and Mass Transfer*, vol. 95, pp. 466–476, 2016. DOI: 10.1016/j.ijheatmasstransfer.2015.11.052.

[183] N. Phan and H. Nagano, "Fabrication and testing of a miniature flat evaporator loop heat pipe with polydimethylsiloxane and molding," *Applied Thermal Engineering*, p. 115 377, 2020. DOI: 10.1016/j.applthermaleng.2020.115377.

[184] J. Qu, H. Wu, P. Cheng, Q. Wang, and Q. Sun, "Recent advances in MEMS-based micro heat pipes," *International Journal of Heat and Mass Transfer*, vol. 110, pp. 294–313, 2017. DOI: 10.1016/j.ijheatmasstransfer.2017.03.034.

[185] N. S. Dhillon, "Micro-columnated loop heat pipe: The future of electronic substrates," Ph.D. dissertation, University of California, Berkeley, 2012.

[186] N. S. Dhillon, A. P. Pisano, C. Hogue, and M. A. Hopcroft, "Mlhp: A high heat flux localized cooling technology for electronic substrates," in *ASME 2008 International Mechanical Engineering Congress and Exposition*, American Society of Mechanical Engineers, 2008, pp. 621–630. DOI: 10.1115/IMECE2008-66993.

[187] S. Kandlikar, S. Garimella, D. Li, S. Colin, and M. R. King, *Heat transfer and fluid flow in minichannels and microchannels*. elsevier, 2005.

[188] J. W. Coleman, "An experimentally validated model for two-phase sudden contraction pressure drop in microchannel tube headers," *Heat transfer engineering*, vol. 25, no. 3, pp. 69–77, 2004. DOI: 10.1080/01457630490280335.

[189] N. J. English and S. G. Kandlikar, "An experimental investigation into the effect of surfactants on air-water two-phase flow in minichannels," *Heat transfer engineering*, vol. 27, no. 4, pp. 99–109, 2006. DOI: 10.1080/01457630500523980.

[190] Praveen S. Medis, "Development of Microfluidic Packaging Strategies, with Emphasis on the Development of a MEMS Based Micro Loop Heat Pipe," Ph.D. dissertation, UNIVERSITY OF CINCINNATI, 2005.

[191] G. P. Peterson, A. B. Duncan, and M. H. Weichold, "Experimental investigation of micro heat pipes fabricated in silicon wafers," *Journal of Heat Transfer*, vol. 115, no. 3, pp. 751–756, 1993. DOI: 10.1115/1.2910747.

[192] Y. Cao, M. Gao, and E. Pinilla, "Fabrication and test of a filling station for micro/miniature devices," in *Proceedings of the Thirty-Second Intersociety Energy Conversion Engineering Conference*, IEEE, vol. 2, 1997, pp. 1509–1513. DOI: 10.1109/IECEC.1997.661993.

[193] C. Li, Y. Luo, C. Zhou, Q. Shan, and X. Wang, "Charging method of micro heat pipe for high-power light-emitting diode," *Micro & Nano Letters*, vol. 10, no. 10, pp. 518–522, 2015. DOI: 10.1049/mnl.2015.0097.

[194] C. Li, X. Wang, C. Zhou, Y. Luo, Z. Li, and S. Li, "New encapsulation method using low-melting-point alloy for sealing micro heat pipes," *Journal of Mechanical Science and Technology*, vol. 31, no. 6, pp. 2621–2626, 2017. DOI: 10.1007/s12206-017-0504-7.

[195] X.-d. Wang, G. Liu, L.-l. Zou, and Y. Luo, "Vacuum fluid charging and packaging technique for micro heat pipes," in *2013 14th International Conference on Electronic Packaging Technology*, IEEE, 2013, pp. 46–49. DOI: 10.1109/ICEPT.2013.6756418.

[196] M. T. Ababneh, S. Chauhan, F. M. Gerner, D. Hurd, P. de Bock, and T. Deng, "Charging station of a planar miniature heat pipe thermal ground plane," *Journal of heat transfer*, vol. 135, no. 2, 2013. DOI: 10.1115/1.4007430.

[197] S. G. Singh, R. R. Bhide, S. P. Duttagupta, B. P. Puranik, and A. Agrawal, "Two-phase flow pressure drop characteristics in trapezoidal silicon microchannels," *IEEE Transactions on Components and Packaging Technologies*, vol. 32, no. 4, pp. 887–900, 2009. DOI: 10.1109/TCAPT.2009.2019634.

[198] M. Le Berre, G. Pandraud, P. Morfouli, and M. Lallemand, "The performance of micro heat pipes measured by integrated sensors," *Journal of Micromechanics and Microengineering*, vol. 16, no. 5, p. 1047, 2006. DOI: 10.1088/0960-1317/16/5/023.

[199] X.-D. Wang, L.-L. Zou, J.-G. Liu, Y. Luo, G. Liu, and B.-K. Yu, "Experimental investigation of copper-grooved micro heat pipes (mhps)," *Journal of Solid State Lighting*, vol. 1, no. 1, pp. 1–8, 2014. DOI: 10.1186/s40539-014-0014-5.

[200] Y.-H. Lin, S.-W. Kang, and T.-Y. Wu, "Fabrication of polydimethylsiloxane (pdms) pulsating heat pipe," *Applied Thermal Engineering*, vol. 29, no. 2-3, pp. 573–580, 2009. DOI: 10.1016/j.applthermaleng.2008.03.028.

[201] C. Guo, X. Hu, W. Cao, D. Yu, and D. Tang, "Effect of mechanical vibration on flow and heat transfer characteristics in rectangular microgrooves," *Applied Thermal Engineering*, vol. 52, pp. 385–393, 2013. DOI: 10.1016/j.applthermaleng.2012.12.010.

[202] C. Yan and H. B. Ma, "Analytical Solutions of Heat Transfer and Film Thickness in Thin-Film Evaporation," *J. Heat Transfer*, vol. 135, p. 031 501, 2013. DOI: 10.1115/1.4007856.

[203] H. B. Ma and G. P. Peterson, "Temperature Variation and Heat Transfer in Triangular Grooves with an Evaporating Film," *Journal Of Thermophysics And Heat Transfer*, vol. 11, pp. 90–97, 1997. DOI: 10.2514/2.6205.

[204] H. Wang, Z. Pan, and Z. Chen, "Thin-liquid-film evaporation at contact line," *Frontiers of Energy and Power Engineering in China*, vol. 3, pp. 141–151, 2009. DOI: 10.1007/s11708-009-0020-2.

[205] P. C. Stephan and C. A. Busse, "Analysis of the heat transfer coefficient of grooved heat pipe evaporator walls," *International Journal of Heat and Mass Transfer*, vol. 35, pp. 383–391, 1992. DOI: 10.1016/0017-9310(92)90276-X.

[206] E. G. Jung and J. H. Boo, "A numerical modeling for the steady-state performance of a micro heatpipe using thin liquid film theory," *International Journal of Heat and Mass Transfer*, vol. 126, pp. 557–566, 2018. DOI: 10.1016/j.ijheatmasstransfer.2018.05.067.

[207] J. L. Plawsky, A. G. Fedorov, S. V. Garimella, H. B. Ma, S. C. Maroo, L. Chen, and Y. Nam, "Nano-and microstructures for thin-film evaporation-A review," *Nanoscale and Microscale Thermophysical Engineering*, vol. 18, pp. 251–269, 2014. DOI: 10.1080/15567265.2013.878419.

[208] P. Wayner Jr, "A constant heat flux model of the evaporating interline region," *International Journal of Heat and Mass Transfer*, vol. 21, pp. 362–364, 1978. DOI: 10.1016/0017-9310(78)90131-X.

[209] M. Chernysheva and Y. F. Maydanik, "Effect of liquid filtration in a wick on thermal processes in a flat disk-shaped evaporator of a loop heat pipe," *International Journal of Heat and Mass Transfer*, vol. 106, pp. 222–231, 2017. DOI: 10.1016/j.ijheatmasstransfer.2016.10.037.

[210] Y. F. Maydanik, V. G. Pastukhov, M. A. Chernysheva, *et al.*, "Development and investigation of a miniature copper-acetone loop heat pipe with a flat evaporator," *Journal of Electronics Cooling and Thermal Control*, vol. 5, no. 04, p. 77, 2015. DOI: 10.4236/jectc.2015.54006.

[211] W. Joung, J. Lee, S. Lee, and J. Lee, "Derivation and validation of a figure of merit for loop heat pipes with medium temperature working fluids," *Journal of Heat Transfer*, vol. 138, no. 5, 2016. DOI: 10.1115/1.4032534.

[212] Y. Yadavalli, J. A. Weibel, and S. V. Garimella, "Performance-governing transport mechanisms for heat pipes at ultrathin form factors," *IEEE Transactions on Components, Packaging and Manufacturing Technology*, vol. 5, no. 11, pp. 1618–1627, 2015. DOI: 10.1115/1.4032534.

[213] G. Patankar, J. A. Weibel, and S. V. Garimella, "Working-fluid selection for minimized thermal resistance in ultra-thin vapor chambers," *International Journal of Heat and Mass Transfer*, vol. 106, pp. 648–654, 2017. DOI: 10.1016/j.ijheatmasstransfer.2016.09.038.

[214] C. Liu, R. Xie, N. Li, D. Lu, F. Hong, and Y. Wu, "Experimental study of loop heat pipes with different working fluids in 190 260 k," *Applied Thermal Engineering*, p. 115 530, 2020. DOI: 10.1016/j.applthermaleng.2020.115530.

[215] D. S. Naruka, R. Dwivedi, and P. K. Singh, "Experimental inquisition of heat pipe: Performance evaluation for different fluids," *Experimental Heat Transfer*, pp. 1–15, 2020. DOI: 10.1080/08916152.2020.1713254.

[216] H. Jouhara, A. Chauhan, T. Nannou, S. Almahmoud, B. Delpech, and L. C. Wrobel, "Heat pipe based systems - Advances and applications," *Energy*, vol. 128, pp. 729–754, 2017. DOI: 10.1016/j.energy.2017.04.028.

[217] V. Jasvanth, A. Ambirajan, D. Kumar, and J. H. Arakeri, "Effect of heat pipe figure of merit on an evaporating thin film," *Journal of Thermophysics and Heat Transfer*, vol. 27, no. 4, pp. 633–640, 2013. DOI: 10.2514/1.T3980.

[218] C. Akhter, R. Choudhury, F. T. Huda, and M. N. Hasan, "Nano-scale transport characteristics during thin film evaporation: Effect of liquid film thickness," in *AIP Conference Proceedings*, AIP Publishing, vol. 1980, 2018, p. 050 028. DOI: 10.1063/1.5044364.

[219] W. R. Gambill and J. H. Lienhard, "An Upper Bound for the Critical Boiling Heat Flux," *Journal of Heat Transfer*, vol. 111, no. 3, pp. 815–818, 1989. DOI: 10.1115/1.3250759.

[220] J. Bevan Ott and J. Boerio-Goates, *Chemical thermodynamics: principles and applications*. Academic Press, London, 2000.

Appendix

APPENDIX A

DERIVATION OF IMPORTANT PARAMETERS

A.1 Governing Equations for thin film evaporation model

A.1.1 Film thickness

From equation (1.2):

$$P_v = P_l + P_d + P_c$$

$$\implies P_v = P_l + P_d + \sigma \frac{\frac{d^2\delta}{dx^2}}{\{1+(\frac{d\delta}{dx})^2\}^{3/2}} \quad \text{(From equation (6.2))}$$

Differentiating with respect to x:

$$0 = \frac{dP_l}{dx} + \frac{dP_d}{dx} + \frac{\sigma}{\{1+(\frac{d\delta}{dx})^2\}^{3/2}} \left[\frac{d^3\delta}{dx^3} - \frac{3(\frac{d\delta}{dx})(\frac{d^2\delta}{dx^2})^2}{\{1+(\frac{d\delta}{dx})^2\}} \right]$$

This gives:

$$\frac{d^3\delta}{dx^3} = \frac{3(\frac{d\delta}{dx})(\frac{d^2\delta}{dx^2})^2}{\{1+(\frac{d\delta}{dx})^2\}} - \frac{1}{\sigma}\left(\frac{dP_l}{dx} + \frac{dP_d}{dx}\right)\left\{1+\left(\frac{d\delta}{dx}\right)^2\right\}^{3/2}$$

A.1.2 Liquid pressure

From Lubrication approximation:

$$\frac{dP_l}{dx} = \mu_l \left(\frac{d^2u_l}{dy^2}\right)$$

Integrating:

$$\frac{du_l}{dy} = \frac{1}{\mu_l}\frac{dP_l}{dx}y + C \tag{A.1}$$

Again Integrating:

$$u_l = \left(\frac{1}{\mu_l}\frac{dP_l}{dx}\right)\frac{y^2}{2} + Cy + D \tag{A.2}$$

Boundary conditions are:

1. At $y = \delta$, $\frac{du_l}{dy} = 0$
2. At $y = 0$, $u_l = \beta\frac{du_l}{dy}$

Applying the first boundary condition on equation (A.1):

$$C = -\frac{1}{\mu_l}\frac{dP_l}{dx}\delta$$

Applying the second boundary condition on equation (A.2):

$$\begin{aligned}
&\beta\frac{du_l}{dy} = D \\
\implies &\beta \times C = D \quad \text{(Using equation (A.1))} \\
\implies &D = -\frac{\beta}{\mu_l}\frac{dP_l}{dx}\delta
\end{aligned}$$

Thus, substituting the values of C and D in equation (A.2):

$$\begin{aligned}
u_l &= \left(\frac{1}{\mu_l}\frac{dP_l}{dx}\right)\frac{y^2}{2} - \left(\frac{1}{\mu_l}\frac{dP_l}{dx}\delta\right)y - -\frac{\beta}{\mu_l}\frac{dP_l}{dx}\delta \\
\implies u_l &= \frac{1}{2\mu_l}\frac{dP_l}{dx}
\end{aligned} \tag{A.3}$$

Putting the value of u_l in equation (**??**):

$$\dot{m}_l = \int_0^{\delta} \rho_l \left\{\frac{1}{2\mu_l}\frac{dP_l}{dx}\right\} dy$$

This gives:

$$\frac{dP_l}{dx} = -\frac{3\nu_l \dot{m}_l}{\delta^2(\delta + 3\beta)}$$

A.1.3 Vapour pressure

If vapour pressure gradient is considered, then the shear stress at the liquid-vapour interface cannot be neglected. Thus, the modified boundary conditions of the liquid velocity are[142]:

1. At $y = \delta$, $\frac{du_l}{dy} = \frac{\tau}{\mu_l}$
2. At $y = 0$, $u_l = \beta\frac{du_l}{dy}$

This gives:

$$u_l = \frac{1}{2\mu_l}\frac{dP_l}{dx} - \frac{\tau}{\mu_l}(y + \beta) \tag{A.4}$$

The momentum equation for u_v (vapour velocity) is given by:

$$\frac{dP_v}{dx} = -\mu_v\left(\frac{d^2u_v}{dy^2}\right) \tag{A.5}$$

Integrations lead to:

$$\frac{du_v}{dy} = -\frac{1}{\mu_v}\frac{dP_v}{dx}y + M \tag{A.6}$$

And

$$u_v = -\left(\frac{1}{\mu_v}\frac{dP_v}{dx}\right)\frac{y^2}{2} + My + N \tag{A.7}$$

Boundary conditions are:

- At $y = H/2$, $\frac{du_v}{dy} = 0$
- At $y = \delta$, $u_v = u_\delta$

The value of u_δ can be found from equation (A.4). Thus,

$$u_\delta = -\frac{1}{2\mu_l}\frac{dP_l}{dx} - \frac{\tau}{\mu_l}(\delta + \beta) \tag{A.8}$$

Applying boundary conditions to equations (A.6) and (A.7), we get:

$$u_v = u_\delta - \frac{1}{2\mu_v}\frac{dP_v}{dx}(y + \delta - H) \tag{A.9}$$

Mass flow rate of vapour is given by

$$\dot{m}_v = -\int_\delta^{H/2} \rho_v u_v dy \tag{A.10}$$

Putting the value of u_v in equation (A.10) we have:

$$\begin{aligned}
\dot{m}_v &= -\int_\delta^{H/2} \rho_v\left\{u_\delta - \frac{1}{2\mu_v}\frac{dP_v}{dx}(y + \delta - H)\right\}dy \\
&= -\left[\rho_v u_\delta\left(\frac{H}{2} - \delta\right) - \frac{\rho_v}{2\mu_v}\frac{dP_v}{dx}\int_\delta^{H/2}(y^2 - Hy - \delta^2 + H\delta)dy\right] \\
&= -\left[\rho_v u_\delta\left(\frac{H}{2} - \delta\right) - \frac{1}{2\nu_v}\frac{dP_v}{dx}\left(\left|\frac{y^3}{3}\right|_\delta^{H/2} - H\left|\frac{y^2}{2}\right|_\delta^{H/2} - \delta^2\left|y\right|_\delta^{H/2} + H\delta\left|y\right|_\delta^{H/2}\right)\right] \\
&= -\left[\rho_v u_\delta\left(\frac{H}{2} - \delta\right) - \frac{1}{2\nu_v}\frac{dP_v}{dx}\left\{\left(\frac{H^3}{24} - \frac{\delta^3}{3}\right) - \frac{H}{2}\left(\frac{H^2}{4} - \delta^2\right) - \delta^2\left(\frac{H}{2} - \delta\right) + H\delta\left(\frac{H}{2} - \delta\right)\right\}\right]
\end{aligned}$$

Now, $\frac{H}{2} >> \delta$. So, higher order of δ can be safely neglected. Hence the above equation becomes:

$$\begin{aligned}
\dot{m}_v &= -\left[\rho_v u_\delta\left(\frac{H}{2}\right) - \frac{1}{2\nu_v}\frac{dP_v}{dx}\left\{\left(\frac{H^3}{24}\right) - \frac{H}{2}\left(\frac{H^2}{4}\right) - \delta^2\left(\frac{H}{2}\right) + H\delta\left(\frac{H}{2}\right)\right\}\right] \\
\implies \frac{1}{2\nu_v}\frac{dP_v}{dx}&\left\{-\frac{H^3}{12} - \frac{H\delta}{2}(\delta - H)\right\} = \dot{m}_v + \rho_v u_\delta\left(\frac{H}{2}\right) \\
\implies \frac{dP_v}{dx} &= -\frac{24\nu_v}{H^3 + 6H\delta(\delta - H)}\left(\dot{m}_v + \rho_v u_\delta\frac{H}{2}\right)
\end{aligned} \tag{A.11}$$

Now at the liquid-vapour interface, the shear stress for vapour is equal to the shear stress for liquid.

$$\therefore \tau = \mu_l \frac{\partial u_l}{\partial y}\Big|_{y=\delta} = -\mu_v \frac{\partial u_v}{\partial y}\Big|_{y=\delta}$$

From equation (A.9), we have:

$$\begin{aligned}\tau &= -\mu_v \frac{\partial}{\partial y}\left\{u_\delta - \frac{1}{2\mu_v}\frac{dP_v}{dx}(y+\delta-H)\right\}\Big|_{y=\delta} \\ &= \frac{1}{2}\frac{dP_v}{dx}|_{y=\delta} \\ &= \left(\delta - \frac{H}{2}\right)\frac{dP_v}{dx}\end{aligned}$$

Putting the value of τ in equation (6.4), we have:

$$\begin{aligned}\frac{dP_l}{dx} &= -\frac{3\nu_l}{\delta^2(\delta+3\beta)}\left\{\dot{m}_l + \frac{\tau\delta}{\nu_l}\left(\frac{\delta}{2}+\beta\right)\right\} \\ &= -\frac{3\nu_l}{\delta^2(\delta+3\beta)}\left\{\dot{m}_l + \frac{\delta}{\nu_l}\left(\frac{\delta}{2}+\beta\right)\left(\delta-\frac{H}{2}\right)\frac{dP_v}{dx}\right\}\end{aligned}$$

Similarly, equation (A.8) becomes:

$$\begin{aligned}u_\delta &= -\frac{1}{2\mu_l}\frac{dP_l}{dx} - \frac{\tau}{\mu_l}(\delta+\beta) \\ &= -\frac{1}{2\mu_l}\frac{dP_l}{dx} - \frac{1}{\mu_l}(\delta+\beta)\left(\delta-\frac{H}{2}\right)\frac{dP_v}{dx} \\ &= -\frac{1}{2\mu_l}\delta(\delta+2\beta)\frac{dP_l}{dx} - \frac{1}{2\mu_l}(\delta+\beta)(2\delta-H)\frac{dP_v}{dx}\end{aligned}$$

Putting the value of u_δ in equation (A.11), we have:

$$\frac{dP_v}{dx} = -\frac{24\nu_v}{H^3+6H\delta(\delta-H)}\left[\dot{m}_v + \frac{\rho_v H}{2}\left\{-\frac{1}{2\mu_l}\delta(\delta+2\beta)\frac{dP_l}{dx} - \frac{1}{2\mu_l}(\delta+\beta)(2\delta-H)\frac{dP_v}{dx}\right\}\right] \tag{A.12}$$

A.1.4 Mass flow rate

Wayner's model (equation (6.6)) is used to calculate the liquid mass flow rate, which is a simplification of Schrage model[25]. Following is its derivation[24]:

The Schrage mass flux model is given by:

$$\begin{aligned}\dot{m}'' &= \frac{2\hat{\sigma}}{2-\hat{\sigma}}\left(\frac{\overline{M}}{2\pi\overline{R}}\right)^{1/2}\left(\frac{P_{\mathrm{lv}}}{T_{\mathrm{lv}}^{1/2}} - \frac{P_{\mathrm{v}}}{T_{\mathrm{v}}^{1/2}}\right) \\ \implies \dot{m}'' &= \frac{2\hat{\sigma}}{2-\hat{\sigma}}\left(\frac{\overline{M}}{2\pi\overline{R}T_{\mathrm{lv}}}\right)^{1/2}(P_{\mathrm{lv}} - P_{\mathrm{v}})\end{aligned} \tag{A.13}$$

$\because$ For a liquid with low superheat, $T_{lv} \approx T_v$

Now, consider an isothermal process in which a liquid at reference state 1 is converted to gas at reference state 2.

$$\therefore \mathrm{d}G_m = \overline{R}T\,\mathrm{d}\ln(\mathrm{fug}) \tag{A.14}$$

$\because$ in a pure substance, the chemical potential is equal to its Gibbs free energy for a mole. Now, integrating:

$$\int_{\mathrm{G_{m1}}}^{\mathrm{G_{m2}}} \mathrm{dG_m} = \overline{R}T \int_{\ln(f_1)}^{\ln(f_2)} \mathrm{d}\ln(\mathrm{fug})$$
$$\implies \mathrm{G_{m2}} - \mathrm{G_{m1}} = \overline{R}T\,\ln\left(\frac{\mathrm{fug_2}}{\mathrm{fug_1}}\right)$$
$$\implies \frac{\mathrm{G_{m2}}}{T} - \frac{\mathrm{G_{m1}}}{T} = \overline{R}\ln(\mathrm{fug_2}) - \overline{R}\ln(\mathrm{fug_1})$$

Differentiating with respect to T at constant P:

$$\left\{\frac{\partial(G_{\mathrm{m2}}/T)}{\partial T}\right\}_P - \left\{\frac{\partial(G_{\mathrm{m1}}/T)}{\partial T}\right\}_P = \overline{R}\left[\frac{\partial\{\ln(\mathrm{fug_2})\}}{\partial T}\right]_P - \overline{R}\left[\frac{\partial\{\ln(\mathrm{fug_1})\}}{\partial T}\right]_P$$
$$\implies -\frac{H_{m2}}{T^2} + \frac{H_{m1}}{T^2} = \overline{R}\left[\frac{\partial\{\ln(\mathrm{fug_2})\}}{\partial T}\right]_P - \overline{R}\left[\frac{\partial\{\ln(\mathrm{fug_1})\}}{\partial T}\right]_P \quad \text{(From Gibbs-Helmoltz equation)}$$
$$\implies \left[\frac{\partial\{\ln(\mathrm{fug_2})\}}{\partial T}\right]_P - \left[\frac{\partial\{\ln(\mathrm{fug_1})\}}{\partial T}\right]_P = -\frac{H_{m2}}{\overline{R}T^2} + \frac{H_{m1}}{\overline{R}T^2}$$

Thus,

$$\left[\frac{\partial\{\ln(\mathrm{fug})\}}{\partial T}\right]_P = -\frac{\lambda_m}{\overline{R}T^2} \tag{A.15}$$

Again considering equation (A.14):

$$\mathrm{d}G_m = \overline{R}T\,\mathrm{d}\ln(\mathrm{fug})$$
$$\implies \mathrm{d}\ln(\mathrm{fug}) = \frac{\mathrm{d}G_m}{\overline{R}T}$$
$$\implies \frac{\mathrm{d}\ln(\mathrm{fug})}{\mathrm{d}P} = \frac{\mathrm{d}G_m}{\mathrm{d}P}\frac{1}{\overline{R}T}$$
$$\implies \left(\frac{\mathrm{d}\ln(\mathrm{fug})}{\mathrm{d}P}\right)_T = \frac{\mathrm{V_m}}{\overline{R}T} \quad \text{(From [220])} \tag{A.16}$$

Now, we know that:

$$d\ln(\mathrm{fug}) = \left(\frac{\mathrm{d}\ln(\mathrm{fug})}{\mathrm{d}T}\right)_P + \left(\frac{\mathrm{d}\ln(\mathrm{fug})}{\mathrm{d}P}\right)_T$$
$$= -\frac{\lambda_m}{\overline{R}T^2} + \frac{\mathrm{V_m}}{\overline{R}T} \quad \text{(Combining (A.15) and (A.16))}$$

Integrating over a range where the fugacity is approximately equal to the vapour pressure of the liquid:

$$\int d\ln(\mathrm{fug}) = \frac{\overline{M}\lambda}{\overline{R}T_vT_{lv}}(T_{lv} - T_v) + \frac{V_m}{\overline{R}T_{lv}}(P_l - P_v)$$

$$\implies \ln\left(\frac{P_{lv}}{P_v}\right) = \frac{\overline{M}\lambda}{\overline{R}T_vT_{lv}}(T_{lv}-T_v) + \frac{V_m}{\overline{R}T_{lv}}(P_l-P_v)$$

$$\implies \frac{P_{lv}-P_v}{P_v} = \frac{\overline{M}\lambda}{\overline{R}T_vT_{lv}}(T_{lv}-T_v) + \frac{V_m}{\overline{R}T_{lv}}(P_l-P_v) \quad \text{(Taylor's expansion)}$$

$$\implies P_{lv}-P_v = \frac{\overline{M}\lambda P_v}{\overline{R}T_vT_{lv}}(T_{lv}-T_v) - \frac{P_vV_m}{\overline{R}T_{lv}}(P_v-P_l)$$

Putting the value of $P_{lv}-P_v$ in equation (A.13):

$$\dot{m}'' = \frac{2\hat{\sigma}}{2-\hat{\sigma}}\left(\frac{\overline{M}}{2\pi\overline{R}T_{\mathrm{lv}}}\right)^{1/2}\left\{\frac{\overline{M}\lambda P_v}{\overline{R}T_vT_{lv}}(T_{lv}-T_v) - \frac{P_vV_m}{\overline{R}T_{lv}}(P_v-P_l)\right\}$$

A.1.5 Interface temperature

1. Derivation of equation (6.8):

   Heat flux due to evaporation at the interface = Heat flux due to conduction through the thin film

   $$\implies m''\lambda = \frac{k_l(T_w-T_{\mathrm{lv}})}{\delta}$$

   This gives:

   $$T_{\mathrm{lv}} = T_w - \frac{m''\lambda\delta}{k_l}$$

2. Derivation of equation (6.9):

   $$\left(\frac{\mathrm{d}P}{\mathrm{d}T}\right)_{\mathrm{sat}} = \frac{\lambda}{T_v\left(\frac{1}{\rho_v}-\frac{1}{\rho_l}\right)} \quad \text{(Clausius-Clapeyron equation)}$$

   $$\implies \left(\frac{\mathrm{d}P}{\mathrm{d}T}\right)_{\mathrm{sat}} = \frac{\rho_v\lambda}{T_v} \quad (\because \rho_v << \rho_l)$$

   $$\implies \frac{\Delta P}{T_{\mathrm{lv}}-T_{\mathrm{v}}} = \frac{\rho_v\lambda}{T_v}$$

   $$\implies T_{\mathrm{lv}} = T_{\mathrm{v}} + T_{\mathrm{v}}\frac{\Delta P}{\rho_v\lambda}$$

   This gives:

   $$T_{\mathrm{lv}} = T_{\mathrm{v}}\left(1+\frac{P_v-P_l}{\rho_v\lambda}\right)$$

3. Derivation of equation (6.10):

   $$\left(\frac{\mathrm{d}P}{\mathrm{d}T}\right)_{\mathrm{sat}} = \frac{\lambda}{T_v\left(\frac{1}{\rho_v}-\frac{1}{\rho_l}\right)}$$

$$\implies \frac{T_v \, \mathrm{d}P_v}{\rho_v} = \frac{T_v \, \mathrm{d}P_l}{\rho_l} + \lambda \, \mathrm{d}T \tag{A.17}$$

$\because \mathrm{d}P_v = 0$, this gives:

$$T_{\mathrm{lv}} = T_v\left(1 + \frac{P_v - P_l}{\rho_l \, \lambda}\right)$$

The authors have not given the intermediate steps leading to this expression.

A.2 Boundary conditions for thin film evaporation model

A.2.1 Film thickness

1. Derivation of $(\delta_0)_{\mathrm{way}}$: At the start of the thin film, no evaporation takes place. Hence:

$$\begin{aligned}
&\dot{m}'' = 0 \\
\implies &\frac{2\hat{\sigma}}{2-\hat{\sigma}}\{c_1(T_w - T_v) - c_2(P_d)\} = 0 \quad \text{(From equation (6.6))} \\
\implies &\left(\frac{P_v \overline{M} \lambda}{\overline{R} T_v T_{\mathrm{lv}}^{3/2}}\right)(T_w - T_v) = \left(\frac{V_l P_v}{\overline{R} T_{\mathrm{lv}}^{3/2}}\right)(P_d) \\
\implies &\frac{\overline{M}\lambda}{T_v}(T_w - T_v) = V_l \frac{\overline{A}}{\delta_0^3} \\
\implies &\delta_0 = \left\{\frac{\overline{A} V_l T_v}{\lambda \overline{M}(T_w - T_v)}\right\}^{1/3}
\end{aligned}$$

This gives:

$$\delta_0 = \left\{\frac{\overline{A} T_v}{\rho_l \lambda (T_w - T_v)}\right\}^{1/3}$$

2. Derivation of $(\delta_0)_{\mathrm{cc}}$: Continuing from equation (6.9):

$$\begin{aligned}
T_{\mathrm{w}} &= T_{\mathrm{v}}\left(1 + \frac{P_v - P_l}{\rho_v \lambda}\right) \\
\implies T_{\mathrm{w}} &= T_{\mathrm{v}}\left(1 + \frac{P_d}{\rho_v \lambda}\right) \\
\implies T_{\mathrm{w}} - T_{\mathrm{v}} &= T_{\mathrm{v}} \frac{\overline{A}}{\rho_v \lambda \delta_0^3}
\end{aligned}$$

This gives:

$$\delta_0 = \left\{ \frac{\overline{A} T_v}{\rho_v \lambda (T_w - T_v)} \right\}^{1/3}$$

A.3 Heat pipe figure of merit

From equation (3.3), neglecting the pressure drop at vapour channels and wick:

$$\Delta P_c = \Delta P_l$$

Now, $\Delta P_c = \sigma \mathbb{R}$, $\Delta P_l = \dfrac{\dot{m}\,\mu_l\,L_{eff}}{\rho_l\,Perm_{wick}\,Area_{wick}}$, $\dot{m} = \dfrac{Q}{\lambda}$

Putting the value of these parameters in the above equation:

$$\sigma \mathbb{R} = \frac{Q}{\lambda} \times \frac{\mu_l L_{eff}}{\rho_l Perm_{wick} Area_{wick}}$$
$$\implies Q = \frac{\mathbb{R}\,Area_{wick}\,Perm_{wick}^{\,2}}{L_{eff}} \times \left[\frac{\rho_l \sigma \lambda}{\mu_l} \right]$$

Thus:

$$FOM = \frac{\rho_l\,\sigma\,\lambda}{\mu_l}$$

A.4 Interline heat flow parameter

Derivation is reproduced from Wayner[28]:

$$P_v = P_l + P_d \quad \text{(From equation (1.1))}$$
$$\implies P_l = P_v - \frac{A}{\delta^3}$$
$$\therefore, \frac{dP_l}{dx} = \frac{3A}{\delta^4}\frac{d\delta}{dx}$$

Now,

$$\dot{m}_l = -\frac{\rho_l \delta^3}{3\mu_l}\frac{dP_l}{dx}$$
$$= -\frac{\rho_l \cancel{\delta^3}}{\cancel{3}\mu_l} \times \frac{\cancel{3}A}{\cancel{\delta^4}}\frac{d\delta}{dx}$$
$$= -\frac{\rho_l A}{\mu_l}\frac{d\delta}{dx}$$

And

$$Q = -\lambda\,\dot{m}_l$$

$$= \frac{\mathrm{d}\delta}{\mathrm{d}x}\left[\frac{\rho_\mathrm{l} \mathrm{A}\lambda}{\mu_\mathrm{l}}\right]$$

Thus:

$$\mathrm{FOM}_{\mathrm{interline}} = \frac{\rho_\mathrm{l} \mathrm{A}\lambda}{\mu_\mathrm{l}}$$

A.5 Theoretical limit of heat flux

Derivation is reproduced from Gambill and Lienhard[219]:

$$\begin{aligned}
(\mathrm{q}_{\max})_{\mathrm{kin}} &= (\mathrm{mass})_{\text{1-molecule}} \times \mathrm{J} \times \lambda \\
&= (\mathrm{mass})_{\text{1-molecule}} \times \frac{\mathrm{s} \times \bar{u}}{4} \times \lambda \quad \left(\because \mathrm{J} = \frac{\mathrm{s} \times \bar{u}}{4}\right) \\
&= (\mathrm{mass})_{\text{1-molecule}} \times \frac{\mathrm{s}}{4} \times \lambda \times \sqrt{\frac{8RT}{\pi}} \quad \left(\because \bar{u} = \sqrt{\frac{8RT}{\pi}}\right) \\
&= \cancel{(\mathrm{mass})_{\text{1-molecule}}} \times \frac{\rho_\mathrm{g}}{\cancel{(\mathrm{mass})_{\text{1-molecule}}}} \times \lambda \times \sqrt{\frac{8RT}{\pi}} \quad \left(\because \mathrm{s} = \frac{\rho_\mathrm{g}}{(\mathrm{mass})_{\text{1-molecule}}}\right)
\end{aligned}$$

This implies:

$$(\mathrm{q}_{\max})_{\mathrm{kin}} = \rho_\mathrm{g} \lambda \sqrt{\frac{RT}{2\pi}}$$

APPENDIX B

THIN-FILM EVAPORATION : EFFECT OF MASS FLUX MODEL AND VAPOUR PRESSURE GRADIENT

B.1 Governing equations

Here, the vapour pressure gradient is not neglected. Hence, it is incorporated in the governing equations and solved. Following are the modified equations:

I Thin film thickness:

$$\frac{d^3\delta}{dx^3} = \frac{3(\frac{d\delta}{dx})(\frac{d^2\delta}{dx^2})^2}{\{1+(\frac{d\delta}{dx})^2\}} + \frac{1}{\sigma}\left(\frac{dP_v}{dx} - \frac{dP_l}{dx} - \frac{dP_d}{dx}\right)\left\{1+\left(\frac{d\delta}{dx}\right)^2\right\}^{3/2}$$

II Vapour Pressure:

$$\frac{dP_v}{dx} = -\frac{24\nu_v}{H^3+6H\delta(\delta-H)}\left[\dot{m}_v + \frac{\rho_v H}{2}\left\{-\frac{1}{2\mu_l}\delta(\delta+2\beta)\frac{dP_l}{dx} - \frac{1}{2\mu_l}(\delta+\beta)(2\delta-H)\frac{dP_v}{dx}\right\}\right]$$

III Liquid Pressure:

$$\frac{dP_l}{dx} = -\frac{3\nu_l}{\delta^2(\delta+3\beta)}\left\{\dot{m}_l + \frac{\delta}{\nu_l}\left(\frac{\delta}{2}+\beta\right)\left(\delta-\frac{H}{2}\right)\frac{dP_v}{dx}\right\}$$

IV Interface temperature

$$T_{lv} = T_w - \frac{m''\Delta h\delta}{k_l}$$

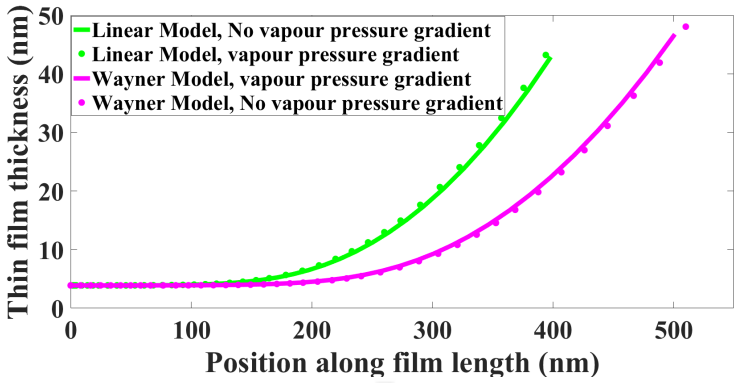

Figure B.1: Effect of vapour pressure gradient on thin film thickness

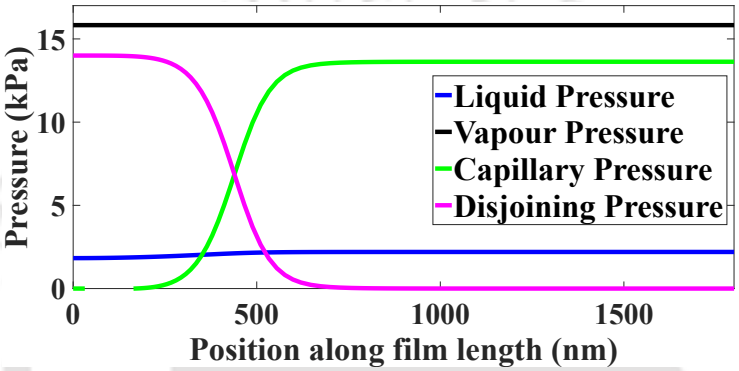

Figure B.2: Variation of different pressure components along the meniscus length

V Mass flow rate:

$$\dot{m}'' = -\frac{\mathrm{d}\dot{m}_l}{\mathrm{d}x}$$

- Linear model

$$\dot{m}'' = \frac{\dot{q}}{\mathrm{h_{fg}}}$$

- Wayner Model

$$\dot{m}'' = \frac{2\hat{\sigma}}{2-\hat{\sigma}}\left(\frac{\overline{M}}{2\pi\overline{R}}\right)^{1/2}\left[\left(\frac{P_v\overline{M}\Delta h}{\overline{R}T_vT_{\mathrm{lv}}^{3/2}}\right)(T_{\mathrm{lv}}-T_v)-\left(\frac{V_lP_v}{\overline{R}T_{\mathrm{lv}}^{3/2}}\right)(P_v-P_l)\right]$$

The boundary conditions used are the same as shown in chapter 6.

B.2 Results

The system of equations is solved using the appropriate boundary conditions. Working fluid used is octane at 70 °C saturation temperature.

Figure B.1 shows how the vapour pressure gradient affects the profile of thin film for different evaporating mass flux model. As can be clearly seen from the figure, vapour pressure gradient plays a negligible role in the thin film region for capillary cooling devices. This can also be confirmed from Figure B.2 where effect on different components of pressure (capillary, disjoining, liquid and vapour) along the film length is shown. The figure clearly shows that the disjoining pressure

decreases and the capillary pressure increases as the film progresses from the thin film region to the capillary region as expected. However, the vapour pressure remains constant throughout the extended meniscus. As such the vapour pressure gradient can be neglected. This justifies the assumption of constant vapour pressure by most of the researchers.

LIST OF PUBLICATIONS

PEER-REVIEWED JOURNALS:

I. **Shahnawaz Ahmed** and Manmohan Pandey, "New Insights on Modeling of Evaporation Phenomena in Thin Films", *Physics of Fluids,* vol. 31, no. 19, pp. 092001, 2019.

II. **Shahnawaz Ahmed** and Manmohan Pandey, "A Simple Figure of Merit for Devices Utilizing Thin Film Evaporation", *International Communications in Heat and Mass Transfer,* vol. 117, pp. 104803, 2020.

III. **Shahnawaz Ahmed** and Manmohan Pandey, "Development of a micro loop heat pipe with a simple MEMS-based fabrication technique", *Nanoscale and Microscale Thermophysical Engineering,* (Under review), 2020.

INTERNATIONAL CONFERENCES:

I. **Shahnawaz Ahmed** and Manmohan Pandey, "Design and Numerical Simulation of a Micro Loop Heat Pipe with Finned Evaporator", *6th International and 43rd National Conference on Fluid Mechanics and Fluid Power (FMFP), Allahabad, India,* 2016.

II. **Shahnawaz Ahmed** and Manmohan Pandey, "Study of Transport Phenomena in the Evaporator of Two–phase Capillary Devices using Thin Film Evaporation Model", *19th International Heat Pipe Conference and 13th International Heat Pipe Symposium, Pisa, Italy,* 2018.

COLOPHON

This document was typeset using the `chthes` typesetting system developed by Chandra Has. The body text is set 11pt with `palatino` font (math and roman) provided by `mathpazo` package. Most of the chapter styles are typeset using the `garamond`, `tikz`, `titlesec`, `tocloft`, `xcolor`, and `microtype` packages.

The title page was generated from a template downloaded from `http://www.fluortools.com/misc/LaTeXtemplate`.

TH-2623_136103007